2013

Large Eddy Simulation Of Surface Pressure Fluctuations Generated By Elevated Gusts

Jericho Erin Cain
University of Mississippi

Recommended Citation

Cain, Jericho Erin, "Large Eddy Simulation Of Surface Pressure Fluctuations Generated By Elevated Gusts" (2013). *Electronic Theses and Dissertations*. 771.
https://egrove.olemiss.edu/etd/771

LARGE EDDY SIMULATION OF SURFACE PRESSURE FLUCTUATIONS GENERATED BY ELEVATED GUSTS.

A Dissertation
presented in partial fulfillment of requirements
for the degree of Doctor of Philosophy
in the Department of Physics and Astronomy
The University of Mississippi

by

JERICHO E. CAIN

May 2013

ABSTRACT

Wind gusts cause substantial damage to wind turbines. If these damaging winds could be detected prior to their interaction with the turbine, the turbine rotor can be decoupled from the generator and gearing system to prevent damage during the gust event. This would significantly reduce wind turbine repair costs. Wind gusts can also create unsafe conditions for aircraft landing. A ground based detection system that monitored elevated wind gusts can provide new information for pilots to use when determining whether or not it is safe to land. In addition, the ability to monitor elevated gust events would provide a new probe to study features in the atmospheric boundary layer. Previous research indicates that elevated velocity events, such as gusts, may trigger pressure fluctuations on the ground. If that is true, it should be possible to monitor elevated wind gusts by measuring these pressure fluctuations. The goal of this project is to develop a ground based detector that monitors the behavior of pressure fluctuations on the ground for indicators that a gust event may be taking place at higher altitudes. In order to recognize these indicators from the pressure measurements on the ground, cross-correlation analysis between the time evolution of the frequency structures corresponding to elevated wind gusts and the pressure on the ground below were investigated. The data for these analysis was generated using a large eddy simulation. This numerical approach was chosen because the nature of the cross-correlation analysis demanded full field wind velocities and pressures at several altitudes. Collecting this data outdoors would be impractical. Correlation coefficients between 0.75 - 0.90 were found. These high correlations indicate that the two signals are causally related. Several common features of the pressures caused by elevated gusts were identified. These features were used to develop a tracking program that monitors fast moving high amplitude pressure fluctuations and to design a ground based pressure sensing array. The array design and tracking software was used to identify several new gust events within the simulated atmosphere. In total, eight gust events have been identified. These events show that the group velocities of the pressure fluctuations measured on the ground increase with the altitude location of the corresponding wind gust source. The methods, tracking software, and array design are ready to be used for experimental research outdoors.

DEDICTION

This dissertation is dedicated to my wife, Jiyeon, who supported me every step of the way through my graduate studies.

ACKNOWLEDGMENTS

Though only my name appears on the cover of this dissertation, many people have helped me along the way. I owe my gratitude to all those people who have made this dissertation possible. My deepest gratitude is to my advisor, Dr. Richard Raspet, for the support and guidance he showed me throughout my dissertation project. I am sure it would have not been possible without his help. I would also like to express my appreciation to my committee members, Drs. Josh Gladden, Maribeth Stolzenburg, and Nathan Murray. I would also like to thank Dr. Martin Otte, from the Environmental Protection Agency, for his help and advice with his simulation. Lastly, I would like to thank Jeremy Webster and Greg Lyons for the insightful discussions we have had about this project.

TABLE OF CONTENTS

LIST OF TABLES

Table Number Page

LIST OF FIGURES

Figure Number Page

CHAPTER 1: INTRODUCTION

1.1 Overview

The main goal for this project is to develop a method to study the relationships between elevated wind gusts and surface pressure fluctuations. This method is then used to identify common features that the surface pressure fluctuations and elevated gusts have in common. Finally, these features are used to design an optimized pressure sensing array and a processing script that tracks pressures on the ground that correspond to elevated wind gusts.

Ground based detection of elevated gusts could be useful for many applications. For example, wind gusts can cause substantial structural damage to wind turbines. If damaging winds can be detected prior to their interaction with the turbine, the turbine rotor can be decoupled from the generator and gearing system to prevent damage. A ground based detection method for elevated wind gusts could also be used at airports to monitor gust activity in the surface layer to warn pilots of unsafe landing conditions. Additionally, ground based elevated gust detection could be used as a new probe to study features of the atmospheric boundary layer (ABL). If elevated turbulent gusts produce identifiable pressure signatures at the ground, inexpensive low frequency pressure sensors can be used to monitor them.

In order to develop a detection criterion, methods to associate high amplitude fast moving ground pressures with elevated gusts are needed. For the correlation studies, full field velocity and pressure data are needed which can only be realistically generated with numerical models. Correlation studies outdoors would be difficult because few events of interest would be available to analyze due to the difficulty of monitoring the wind speeds at several elevations in tandem with pressures monitored with a ground based array. The behavior of signals containing coherent pressure fluctuations that are associated with elevated wind gusts must be understood in a simulated atmosphere first so that outdoor experiments have a search criterion along with a basis for signal processing. For this project the interest is in low frequency pressure fluctuations that are associated with large eddies, therefore a large eddy simulation (LES) is the atmospheric model of choice. Once pressure fluctuations on the ground that are associated with elevated gust events are identified and understood using a LES, a detection method and array design can be developed that monitors pressures at the ground that can be used for verification outdoors.

1.2 Historical Review

Turbulent flow is characterized as being stochastic and chaotic. As such, it is considered one of the most intriguing and frustrating problems in all of classical physics. The phenomenon was recognized at least 500 years ago by da Vinci along with an illustration in one of his sketch books and the description:

> *. . .the smallest eddies are almost numberless, and large things are rotated only by large eddies and not by small ones, and small things are turned by small eddies and large.*

After da Vinci's identification of the phenomenon there seems to be no significant progress made in understanding turbulence further until the 19th century. This review focuses on three main historical lines. The first being the development of turbulence theory as a statistical description up until the dawn of the computer age. The second will be a brief account of the history of numerical modeling of the ABL with significant focus on LES. Finally, the third will describe the research that motivated the idea that elevated wind events produce pressure signatures on the ground.

The equations of motion for fluid flow, including turbulent flow, were first introduced in the early 19th century by Navier and Stokes. This set of equations became known as the

Navier-Stokes equations and in general form can be written as,

$$\rho\left(\frac{\partial\mathbf{v}}{\partial t}+\mathbf{v}\cdot\nabla\mathbf{v}\right)=-\nabla p+\nabla\cdot\mathbf{T}+\mathbf{f} \tag{1.1}$$

where **f** represents body forces per unit volume acting on the fluid. Due to the nonlinear nature of these equations they are difficult to solve analytically. This is why early descriptions of turbulence were primarily observation based even after the development of Eq. 1.1.

The first investigation of the transition from laminar flows to turbulent flows were performed by George Gabriel Stokes. [3] Although Stokes developed the concept of a dimensionless parameter that gives a measure of the ratio of inertial forces to viscous forces it was Osborne Reynolds who popularized it through his systematic investigations of a fluid injected with ink dye flowing through a pipe with smooth transparent walls. [4] Today this parameter is called the Reynolds number,

$$Re=\frac{\rho UL}{\mu}, \tag{1.2}$$

where U and L are velocity and length scales respectively, μ is the dynamic viscosity, and ρ is the fluid density. When the Reynolds number for a flow exceeds a critical value the flow is considered turbulent. Reynolds continued his work in turbulence and published his seminal paper in 1894, in which he identified the Reynolds number as the only physical parameter involved in the transition of a flow from laminar to turbulent.[5] In his paper he concluded that turbulence was too complicated to understand rigorously and so he introduced the decomposition of flow variables into mean and fluctuating contributions. This method, called Reynolds decomposition, led to the prevailing view that since turbulence exhibits random behavior, studying its detailed behavior will not be as effective as studying its statistics.

In 1877 Boussinesq postulated that the momentum transfer caused by turbulent eddies could be modeled with an eddy viscosity. [6] He developed this idea by making an analogy with molecular velocity. He made the argument that eddy viscosity transfers momentum during turbulent motion similar to how molecular viscosity transfers momentum during molecular motion. The hypothesis that turbulent stresses are linearly proportional to mean strain rates is still the basis of most turbulence models used today. Shortly after Reynolds' suggestion that statistical analysis is the tool most appropriate for studying turbulence, Prandtl obtained a statistical result that essentially predicted eddy viscosity as introduced by Boussinesq.[7] Prandtl introduced his mixing length model which is a method to describe momentum transfer by turbulence Reynolds stresses within a Newtonian fluid boundary layer by means of eddy viscosity. This approach has never been successful in making predictions of turbulent flow due to the fact that in this model as the turbulent stress approach zero the heat or mass diffusivity also approaches zero which is not true for real flows. It has, however, been useful in understanding some behavior seen in some simple flows.

During the 1930s, Taylor introduced formal statistical methods involving correlations, Fourier transforms and power spectra into turbulence theory.[8] In addition, he applied these methods to experimental data from wind tunnel flow through a mesh to show that such flows could be viewed as isotropic and homogeneous. He also introduced the idea of viewing turbulence as "frozen" in a field moving with mean streamwise speed U. This allowed him to relate the streamwise wavenumber with the angular frequency as $k = \frac{\omega}{U}$ which became known as Taylor's hypothesis. This hypothesis provides a way to convert time series data into spatial series data.

The velocity fluctuations of a high Reynolds number flow in a three-dimensional velocity field are typically dispersed over all possible wavelengths of the system, from the effective size of the system to the smallest scales where viscous forces dominate the advection and dissipate the kinetic energy of fluid motion. In 1922 Lewis Fry Richardson described this process in verse:

> *"big whirls have lesser whirls that feed on their velocity, and little whirls have lesser whirls and so on to viscosity".*

The statistics of the velocity fluctuation distribution for turbulent flows were quantified more rigorously by Andrei Kolmogorov in 1941.[9] Kolmogorov derived an equation to describe the energy spectrum of the intermediate scales, called the inertial subrange, of high Reynolds number flows. He postulated that velocity fluctuations in the inertial subrange are independent of the initial and boundary conditions, therefore, the turbulent motions in this subrange show universal statistics and the flow is self-similar. Using dimensional analysis he derived his well known "-5/3 power law" describing the energy spectrum in the inertial subrange as,

$$E(\kappa) = \alpha\epsilon^{2/3}\kappa^{-5/3}, \tag{1.3}$$

where κ is the wave number given by $\kappa^2 = \kappa_x^2 + \kappa_y^2 + \kappa_z^2$, ϵ is the rate of average dispersion of energy per unit mass, and α is a dimensionless constant that is ascertained empirically. The physical picture of Eq. 1.3 is that kinetic energy of large-scale eddies is successively subdivided and redistributed among increasing wave number components (smaller eddies) until viscosity becomes significant. Kolmogorov's work represented a distinct departure from Reynolds' approach even though it is still statistical in nature. It is now referred to as the "K41" theory and was the last major piece missing in the tools needed to study turbulence numerically. However, it would be another twenty years before technology would catch up.

In a review paper on turbulence written in 1961, Corrsin estimated the number of grid points required in a direct numerical solution to the Navier-Stokes of a Re = 1000 flow to be 4×10^{14} grid points.[10] Considering that this was a flow with a relatively low Reynolds number, it was clear that a direct numerical simulation (DNS) would not be practical to study extremely turbulent flows such as those that exist in the atmosphere which may have a Reynolds number as high as 10^8. In fact, a DNS is not tenable for most realistic turbulent flows at present. The number of floating point operations (FLOPS) for a DNS increases as the cube of the Reynolds number. For the ABL, DNS requires 10^{24} FLOPS. The fastest super computers available today compute on the order of 10^{15} FLOPS. This means that a realistic DNS of the ABL requires unreasonable computational times. The small scales within turbulent flow absorb most of the computational power during a DNS. At these scales, the dynamics become very difficult to solve for directly. Another method developed to numerically solve for turbulence are solutions to the Reynolds-averaged Navier-Stokes equations (RANS). However, RANS modeling only yields time averaged velocities which do not contain important characteristics of the actual turbulent flow. For research that focuses on dynamic structures within a turbulent flow other numerical approaches are needed.

Large eddy simulation (LES) is an approach that will resolve dynamic structures in the ABL. It is a model that explicitly calculates the behavior of the large eddies in turbulent flow but parameterizes the small eddies using a statistical approach based on Eq. 1.3. The LES method was initially proposed in 1963 by Joseph Smagorinksy to simulate atmospheric air currents.[11] The first application of the LES approach to meteorological flows was made by Deardorff.[12] Deardorff's model was the only model that applied LES to the ABL for many years. This model provided many useful insights into atmospheric turbulence within the boundary layer, such as the scaling parameters for the convective ABL.[13] Over the next decade the rapid development of computers coupled with the desire to improve boundary-layer parameterizations led Chin-Hoh Moeng to develop a new LES model code in 1984.[14] Moeng's LES code took advantage of more modern techniques such as Fast Fourier Transforms (FFT) which allowed her to use a pseudospectral representation in the horizontal direction where the ABL turbulence was nearly homogeneous. It used finite-differencing in the vertical direction, whereas older LES models used a finite-differencing method across the entire grid. Moeng's methods reduced the computational time required by LES and allowed for more detailed resolution of simulated boundary layers.

Up until Moeng's 1984 LES work, the small eddies were modeled using a subgrid model developed by Douglas Lilly in 1967 as will be discussed in more detail in chapter two [15]. Essentially, Lilly derived a closure to Smagorinsky's model from the hypothesized balance between shear production and dissipation with the Kolmogorov spectrum. In his first LES, Deardorff noted that the calculated mean velocity profiles did not follow experimental observation in reproducing the logarithmic layer.[12] Deardorff introduced a modification to this, which was adopted by Moeng, in which a prognostic equation for the subgrid scale turbulence energy is solved in tandem with the LES equations.[16] This reduced the problem but LES continued to over-predict the mean velocity magnitudes and consequently the mean wind shear. Branko Kosevic recognized the problem was due to the fact that Smagorinksy type models only allowed for energy cascade to occur from large scales to small scales as opposed to the reverse. To remedy this, he developed a nonlinear extension to the classical Smagorinksy model that allowed for a local backscatter of energy.[17] Kosevic implemented the nonlinear SGS model in an LES of a shear-driven ABL and showed that it calculated the experimentally observed and theoretically predicted mean velocity profile.

LES continues to be a very active topic of research in meteorology today and progress is continually being made in the development and refinement of SGS models. More recent studies have been done that use LES to generate wind gusts in order to study their effects on various structures and aircraft.[18], [19],[20] A wind gust is characterized by a brief increase in the speed and/or change in the direction of wind. These gusts are responsible for causing substantial damage to wind turbines, buildings, forests, vehicles, as well as compromising the safety of landing aircraft. A method to detect these gusts as they are happening is needed.

Research that first suggested that elevated wind events contributed to pressure on the ground in a way that is measurable came from the dissertation work of Joseph Priestly in 1965. Priestly conducted correlation studies of pressure fluctuations on the ground beneath a turbulent boundary layer. In his thesis he notes that it is probably safe to assume that the dominant influence of an eddy extends a distance approximately proportional to the size of that particular eddy. Therefore one would expect that the high frequency region of the fluctuating pressure, the part arising from the small eddy contribution, is caused by turbulence near the ground. At low frequencies, the source height should be greater because larger eddies would extend to greater heights. If this is true, eddy size as a function of convection velocity should be related to the height versus the wind speed. In other words, if convection velocity corresponds to wind speed, then the wavelength should correspond to source height. In order to test this hypothesis, Priestly used anemometer data collected at an altitude of 4.27 m to measure a wind speed of 2.1 m/s. He then used the relation $k = \frac{\omega}{U_c}$ to plot wavelength versus convection velocity and found that a wind speed of 2.1 m/s corresponds to a wavelength of 22 m. From this Priestly concludes that the effective source height of the 22 meter wavelength disturbance is 4.27 m and it's velocity is 2.1 m/s, or, equivalently, the wavelength of the disturbance is 5.1 times the effective source height.[21] From this Priestly concluded that a wavelength disturbance in the pressure field measured at the ground is proportional to the height of the turbulent source that caused the disturbance. Wavelengths corresponding to low frequencies are associated with higher altitude sources than wavelengths corresponding to high frequencies.

F. Douglas Shields used an array of infrasound sensors in the direction of the flow beneath a turbulent layer to measure the pressure pattern.[22] He determined the convection velocity by dividing the distance between the sensors by the time shift that gives a maximum correlation between the sensor signals. He found that wind noise measurements near the ground level indicated a frequency dependent convection velocity. Shields used a modified version of Taylor's hypothesis, that assumes that different size eddies propagate with different velocities, to associate wind velocity as a function of frequency with wind velocity as a function of eddy size. In other words, the frequency response of the pressure disturbance corresponds to the size of the eddy that caused it. Using corresponding anemometer data, Shields was able to confirm Priestly's results that the effective source height is directly related to the wavelength of the pressure fluctuations.

Priestly's and Shield's research suggest that low frequency disturbances in the pressure measured at the ground correspond to the altitude and size of turbulent eddies. In other words, lower frequency fluctuations in the pressure at the ground correspond to larger eddies at some distance above the ground, whereas high frequency fluctuations correspond to smaller eddies that are closer to the ground.

Jiao Yu made theoretical predictions of the turbulence-shear interaction pressure contributions to wind noise for various microphone systems beneath a turbulent layer and compared these to data collected in the field. The theory predicted the frequency spectra of the pressure structure on the ground from the wind profile above the ground and the measured spectrum of the turbulence. Part of Yu's work used theory to investigate the source altitudes where the dominant influence on the pressure spectral level on the ground for a given wavenumber was located. Yu found that if the model was truncated so that it evaluated the power spectral density (PSD) of the pressure from the ground up to 2.0 m, the PSD for wavenumber contributions greater than 0.1 m trended away from the PSD calculated from altitudes from the ground to infinity. Conversely, when evaluated from z = 1 m to infinity, the PSD trended away from the PSD calculated from the ground to infinity for wavenumber contributions greater than 0.1 m. Yu's predictions revealed that lower frequency contributions to the PSD for the pressure on the ground were predominately influenced by higher altitude sources, whereas higher frequency contributions to the PSD were predominantly influenced by lower altitude sources.[23]

Measurements and models of vertical velocity spectra within the surface layer also show that peak frequencies shift toward lower values with increasing altitudes as shown in Fig. 1.1. [1] This indicates that low frequency pressure information received on the ground comes from higher altitudes within the surface layer.

These studies indicate that the movement and development of the pressure fluctuations on the ground are related to velocity events aloft rather than velocity events near the surface and that measurement of the low frequency pressure response at the ground yields information about turbulent events in the atmosphere.

1.3 The Atmospheric Boundary Layer

The atmospheric boundary layer (ABL) is a well defined structure that evolves with the diurnal cycle over land surfaces. The three major parts of this structure are the daytime convective boundary layer (CBL), the residual layer (RL), and the nighttime stable boundary layer (SBL). If clouds are present, the convective boundary layer is subdivided into a cloud and subcloud layer. At the very bottom of the ABL is a region known as the surface layer where turbulent fluxes and stress vary by less than 10 percent of their magnitude.[2] Fig. 1.2 shows a height versus local time plot which represents the evolution of the ABL throughout a 24 hour period. The CBL will be modeled for this project.

The CBL, also known as the mixed layer (ML), develops during the day. Solar heating of the ground heats the layer of air just above it. This creates thermals as the warm air rises into cooler air. These thermals transport heat and moisture to higher altitudes. As the plumes rise, they expand adiabatically until a thermodynamic equilibrium is reached at the top of the atmospheric boundary layer where the moisture that was transferred by the thermal plumes forms convective clouds in a region called the entrainment zone. The entrainment zone is where air from above becomes mixed into the PBL. Air becomes entrained either by an increase of the PBL depth as thermals become increasingly warm and rise higher, or by air moving downwards into the PBL. The entrainment zone acts as a lid to the rising thermals and the domain of turbulence. At times this lid, or capping stable layer, is strong enough to be classified as a temperature inversion, or in other words, a layer where the normal temperature profile is reversed. This elevated temperature inversion layer is called a capping inversion.

The SBL typically develops during the night time in mid-latitudes and during the day in cold climates. Under these conditions the surface is colder than the surrounding air causing the flow to stratify and turbulence to be generated by shear and destroyed by dissipation and negative buoyancy. [24] SBLs are shallow and are characterized by strong vertical shear and a high wind near the boundary layer top. At that height, the wind can produce a low-level jet. As a result, compared with daytime boundary layers, SBLs provide greater potential for power generation but with the the increased possibility of structural damage from strong vertical and lateral shear.

SBL LES's require very high resolution and long time integrations to get satisfactory statistics. The computational requirements to complete an SBL run at the resolution needed for this project is beyond the scope of the University of Mississippi's supercomputing cluster. However, it is thought that the methods that are developed from CBL LES will translate to SBL conditions. SBL conditions have less background noise than CBL atmospheres so the data analysis should be less of a challenge. With that in mind, the methods for tracking coherent pressure transfers on the ground and their associations with velocity events aloft will be developed for CBL conditions and presented in this dissertation project.

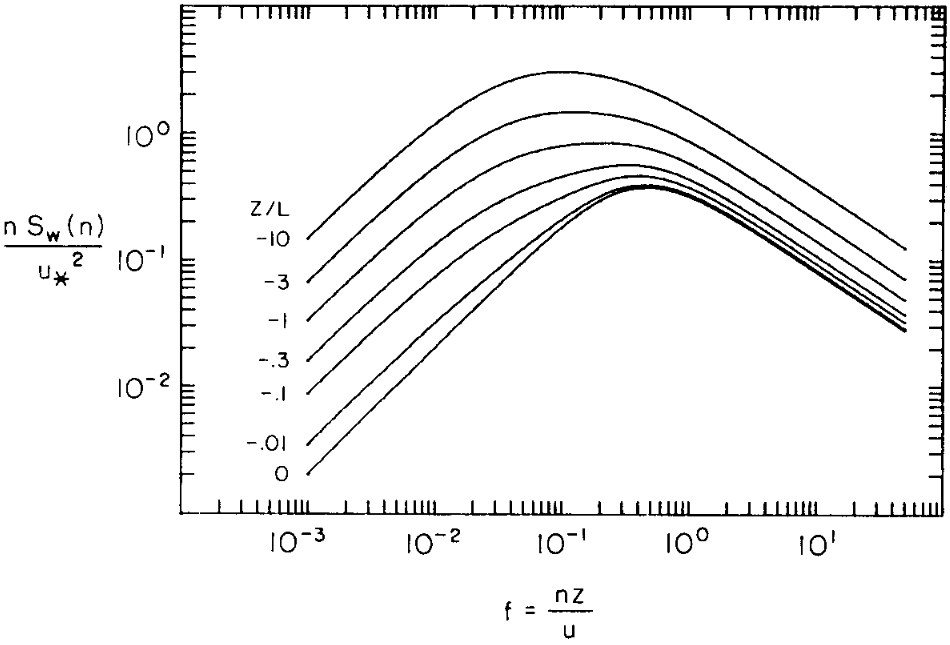

Figure 1.1. The vertical velocity spectra is characterized by a peak frequency shifted toward lower frequencies with increasing altitude within the surface layer. Here z is altitude, L is the negative valued Monin-Obukhov Length, S_w is the vertical spectra, u_* is the surface friction velocity, n is the normalized frequency $\frac{fz}{V}$, and V is the mean wind speed. Figure from *Atmospheric Turbulence* by Panofsky and Dutton [1].

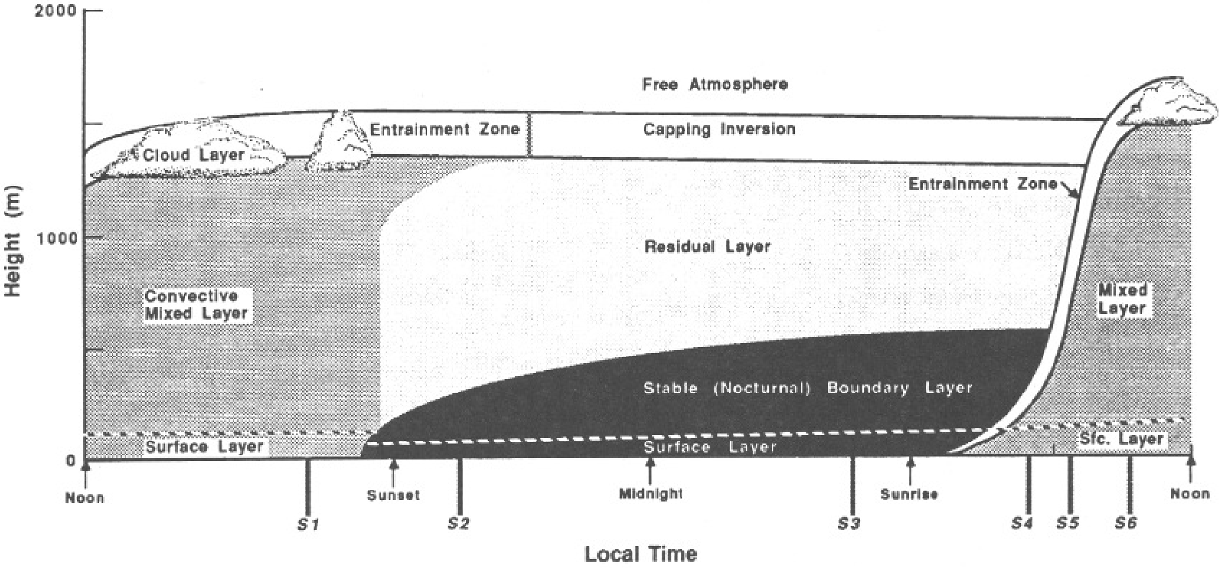

Figure 1.2. **The boundary layer in high pressure regions over land consisting of three major parts: a very turbulent mixed layer, a less-turbulent residual layer containing former mixed-layer air, and a nocturnal stable boundary layer of sporadic turbulence. The mixed layer can be subdivided into a cloud layer and a subcloud layer. Figure from *An Introduction to Boundary Layer Meteorology* by Roland B. Stull [2].**

1.4 Wind Gusts

Wind gusts are the primary atmospheric feature of interest in this project. As defined by the American Meteorological Society AMS Glossary, gusts are reported when the peak wind speed at a point reaches at least 8.2 m/s and the variation in the wind speed between the peaks and lulls is at least 4 m/s.[25] The duration of a gust at a single point is usually less than 20 s. This project uses this definition of a gust for identification purposes.

A common parameter that describes the intensity of a gust is called a gust factor and it is given by $G = \frac{u_{gust}}{\bar{U}}$ where u_{gust} is the maximum speed of the gust and $\bar{U}$ is the the mean wind speed over some chosen time interval.[26] It is common for a moderately windy daytime with mean wind speeds between 0 and 10 m/s measured at altitudes of around 40 m may have gusts with G between 1 and 3.

Research done in the 1970's at the White Sands Missile Range in New Mexico show that gust factors vary with altitude. The meteorological tower used in this research was instrumented at eight levels ranging from 7.6 m to 121.9 m. Gust factors measured during the day were between 1 and 3 with varying frequency. The work concludes that there is a decrease in gust factors associated with increasing height and mean wind speed.[27]

Differences between peaks and lulls, the duration of the gust candidate, the maximum velocity of the gust candidate, the gust factor, and the gust factor trend with increasing altitude will be used to identify gusts and will be used as a check for the LES as to whether or not it is producing realistic gusts.

1.5 Project Description

LES has been used to generate turbulence in the atmospheric boundary layer. Previous studies show that short lived high amplitude features called gusts are present in these simulations. Studies have also shown that gusts can cause significant damage to wind turbines as well as create unsafe landing conditions for aircraft. There is some evidence that elevated velocity events do trigger a pressure response on the ground. The primary goals for this project are to investigate the relationship between elevated velocity events such as wind gusts and their association with pressure patterns on the ground as well as to develop a system that can detect these elevated events from the ground by monitoring the pressure at the ground.

The first step in completing the goals was to study elevated velocity events and their effect on the pressure structure at the ground. To do this, methods for data analysis were developed to study correlations between the time-frequency evolution of the velocity events and the pressure events on the ground. High altitude velocity events were identified and the pressure below the event was checked for features in the pressure pattern. If a cluster of pressures that moved at a similar group velocity to the elevated velocity event was identified, cross-correlation studies between continuous wavelet transforms of their signals were performed. The correlation coefficients for many of these events showed significant correlation.

With the cross-correlation studies complete, the next phase of the project was to investigate optimized array designs that detect the fast moving pressure patterns identified during the cross-correlation analysis. A signal processing code was written that is compatible with any array geometry that identifies moving pressures over a certain threshold, compares the rate and direction in which they propagate across the array, and compares that rate with the velocity on the ground during that time. When such a pressure signal is identified, the script reports the event along with its direction in real time.

Finally, a simulated array was placed at the ground level in the LES data in the path of one of the known events found during the cross-correlation analysis and the processing script was tested. It succeeded in identifying the event. As a final test the simulated array was placed at various locations at the ground level in a separate LES run. Several new events were identified and the velocity fields above these events were checked for elevated events such as gusts. Five such events are presented.

CHAPTER 2: LARGE EDDY SIMULATION

2.1 Concept

An LES calculation filters out the high-frequency component of the flow field and use the low-pass-filtered form of the Navier-Stokes equations to solve for the large scale dynamics only. The effects of the filtered-out small-scale fields on the resolved fields are described by the subgrid-scale (SGS) model. The SGS model represents the interactions between the resolved and unresolved components of the flow field and is developed phenomenologically with Eq. 1.3 as a foundation. This project follows Chin-Hoh Moeng's LES method.[14] The most notable change from Moeng's paper is the use of the Kosevic SGS formulation.[17]

2.2 Filtering

A consequence of Kolmogorov's theory of self-similarity is that large eddies in a turbulent flow are dependent on the flow geometry while small eddy behavior is universal, or, inherent to small scales.[9] As a result, one can independently consider large eddies in an explicit calculation and consider the small eddies implicitly through a subgrid-scale model. Mathematically, separating a resolvable scale from an unresolvable scale is equivalent to a convolution between a function and a filtering kernal $G(\mathbf{x})$ which "picks out" the resolvable part from the function:

$$u_i^r(\mathbf{x}) = \int G(\mathbf{x} - \eta) u_i(\eta) d\eta, \tag{2.1}$$

where u_i is the full velocity field and u_i^r is the resolvable velocity field. u_i can be decomposed as,

$$u_i = u_i^r + u_i', \tag{2.2}$$

where u_i' is the subgrid-scale velocity field.

2.3 Equations of Motion

The equations that govern incompressible flow are continuity,

$$\frac{\partial u_i}{\partial x_i} = 0, \tag{2.3}$$

and the Navier-Stokes equation,

$$\frac{\partial u_i}{\partial t} + \frac{\partial (u_i u_j)}{\partial x_j} + \frac{1}{\rho}\frac{\partial p}{\partial x_i} = \frac{g_i}{\theta_o}\theta - 2\epsilon_{ijk}\Omega_j u_k + \nu \frac{\partial^2 u_i}{\partial x_i \partial x_j}, \tag{2.4}$$

where Ω_j is the Earth's rotation vector, θ is the potential temperature, ν is viscosity, and g_i is the acceleration due to gravity. The first term on the right hand side of Eq. 2.4 is the Boussinesq buoyancy approximation, the second is the Coriolis contribution, and the third represents momentum diffusion due to viscosity.

Using the decomposition from Eq. 2.2 and applying the filter defined in Eq. 2.1 to the equations of motion Eqs. 2.3 and 2.4 yields,

$$\frac{\partial u_i^r}{\partial x_i} = 0, \tag{2.5}$$

$$\frac{\partial u_i^r}{\partial t} + \frac{\partial (u_i^r u_j^r)}{\partial x_j} + \frac{1}{\rho}\frac{\partial p^r}{\partial x_i} = \frac{g_i}{\theta_o}\theta^r - 2\epsilon_{ijk}\Omega_j u_k^r - \frac{\partial \tau_{ij}}{\partial x_j}, \tag{2.6}$$

where the term τ_{ij} is the subgrid scale stress (SGS) and has to be modeled. The Reynolds number for ABL flow is very large so the filtered viscous term is negligible. Taking the divergence of Eq. 2.6 and using Eq. 2.5 yields a Poisson equation for the resolvable pressure field

$$\frac{1}{\rho}\Delta p^r = -\frac{\partial^2 u_i^r u_j^r}{\partial x_i \partial x_j} - \frac{\partial^2 \tau_{ij}}{\partial x_i \partial x_j} - 2\epsilon_{ijk}\Omega_j \frac{\partial u_k^r}{\partial x_i} + \frac{g_i}{\theta_o}\frac{\partial \theta^r}{\partial x_3}. \tag{2.7}$$

2.4 Subgrid Model

Because the Navier-Stokes equations are nonlinear, the filtered equations contain a remnant term, τ_{ij}, that contains information about the small dissipative eddies. This filtered non-linear term, called the subfilter-scale stress, contributes to the transfer of energy between the large and small scales. Energy transfer between the scales is due to the working of the subfilter-scale stresses against the resolvable scale strain rate and the working of the resolvable-scale stresses against the subfilter-scale strain rate. This subgrid-scale stress is the term that is analytically modeled using what is called a subgrid-scale (SGS) model.

The subgrid scale stresses (SGS) are defined as

$$\tau_{ij} = (u_i u_j)^r - u_i^r u_j^r. \tag{2.8}$$

The fundamental goal in LES is trying to express the SGS components defined in Eq. 2.8 in terms of the resolved velocities. The classical SGS model was developed by Douglas Lilly.[15] Lilly developed two models for the SGS effects in LES. He first assumed that energy production is balanced by dissipation,

$$\tau_{ij}^d = -2\nu_e S_{ij}, \tag{2.9}$$

where $\tau_{ij}^d = \tau_{ij} - \frac{2}{3}e\delta_{ij}$ is the anisotropic component of the SGS stress, and the turbulent strain rate tensor $S_{ij} = \frac{u_{i,j}^r + u_{j,i}^r}{2}$.

Lilly used the Smagorinsky model where the local eddy viscosity and the local rate of strain magnitude are related by,

$$\nu_e = (C_s l)^2 (2S_{kl}S_{lk})^{1/2}, \tag{2.10}$$

where l is the characteristic length scale and C_s is the Smagorinksy constant.[11] Lilly required that the spectrum of the resolved motion near the cutoff follow the Kolmogorov inertial subrange form and showed that C_s is related to the inertial subrange velocity spectral constant C_k by $C_s \simeq 0.23 C_k^{-3/4}$ from Eq. 1.3.[28]

Lilly developed a second model for the turbulence in which an equilibrium range is not developed instantaneously. For the subgrid scale eddy-viscosity coefficient , Lilly adopted the modified eddy viscosity relation developed by Prandtl where the eddy-viscosity coefficient is related to the product of a characteristic length scale and a characteristic velocity scale,

$$\nu_e = C_e l (e^r_{sgs})^{1/2}. \tag{2.11}$$

Here e^r_{sgs} is the SGS turbulent kinetic energy defined by

$$e^r_{sgs} = \frac{1}{2}((u_l u_l)^r - u^r_l u^r_l). \tag{2.12}$$

For this case an additional partial differential equation for the SGS kinetic energy is solved along with Eq. 2.30,

$$\frac{\partial e^r_{sgs}}{\partial t} + \left(u^r_j \frac{\partial e^r_{sgs}}{\partial x_j} \right)^r = -\tau_{ij} \frac{\partial u^r_i}{\partial x_j} - \frac{\partial \left(u'(e_{sgs} + p'/\rho) \right)^r}{\partial x_i} - \epsilon, \tag{2.13}$$

where ϵ denotes the dissipation rate. On the left hand side of Eq. 2.13 are local time change and advection terms. On the the right are shear production, a transport term, and viscous dissipation. The transport term and viscous dissipation term on the right hand side have to modeled.

Improved modeling methods have been developed. This project uses an SGS model developed by Branko Kosevic. Smagorinksy-Lilly type models are absolutely dissipative when $\nu_e > 0$. This means that they cannot account for the effects of the backscattering of energy from the small unresolved scales toward the resolved scales. Without this SGS models do not accurately reproduce experimentally observed mean velocity profiles when used in LES's. Kosevic adopted a phenomenological approach to develop a non-linear extension to the Smagorinksy model that allows for backscattering,

$$\tau_{ij}^{d} = -C_e\Delta\left\{2(e_{sgs}^{r})^{1/2}S_{ij} + \left(\frac{27}{8\pi}\right)^{1/3} C_s^{2/3}\Delta\left[C_1\left(S_{ik}S_{kj} - \frac{1}{3}S_{mn}S_{nm}\delta_{ij}\right) + \dots \right.\right.$$
$$\left.\left. C_2\left(S_{ik}\zeta_{kj} - \zeta_{ik}S_{kj}\right)\right]\right\}. \tag{2.14}$$

Here Δ is is a length scale related to the grid size and the model parameter, $\zeta_{ij} = \frac{u_{i,j}^{r} - u_{j,i}^{r}}{2}$, is the rotation rate tensor based on the resolved velocity field, and C_i (i= 1,2) are model parameters determined so that the model provides correct energy transfer and captures the normal stress effects observed in homogeneous shear flows. C_e is related to the Smagorinsky constant C_s by,

$$C_e = \pi^{1/3}\left(\frac{2}{3C_k}\right)^{1/2} C_s^{4/3} = \left(\frac{8\pi}{27}\right)^{1/3} C_s^{4/3},$$

where C_k denotes the Kolmogorov constant. The first term on the right hand side of Eq. 2.14 is the Smagorinsky-Lily term from Eqs. 2.9 and 2.11 that represents the transfer of energy from resolved scales to unresolved scales. The second term on the right hand side represents the transfer of energy from unresolved scales to resolved scales. The third term represents strain from rotational shear. This model has been shown to yield the experimentally observed and theoretical predicted mean velocity profile when applied to an LES of a shear-driven atmospheric boundary layer.[17]

2.5 Numerical Solution

The governing equations of motions found in Eqs. 2.5 and 2.6 in Moeng's original LES can be expressed as

$$\frac{\partial u_i}{\partial t} = R_i - \frac{\partial}{\partial x_i}\left(p + \frac{1}{2}u_j u_j + \frac{2}{3}e_{sgs}\right) \tag{2.15}$$

$$\frac{\partial u_i}{\partial x_i} = 0 \tag{2.16}$$

$$\frac{\partial \Theta}{\partial t} = R_t. \tag{2.17}$$

Here, u_i is the velocity vector, Θ is the potential temperature, R_i represents the forcing terms from the Navier-Stokes equations (advection, SGS diffusion, buoyancy, and the Coriolis force), R_t represents the advection and sub-grid diffusion of potential temperature, p is the pressure, and e_{sgs} is the sub-grid kinetic energy. The TKE term $u_j u_j/2$ originates from how the LES computes the advective terms, and the e_{sgs} term results from the subgrid formulation. The code groups all of the divergence terms together, defining a modified pressure P as

$$P = p + \frac{1}{2} u_j u_j + e_{sgs}, \tag{2.18}$$

so that the system of equation can be written as

$$\frac{\partial u_i}{\partial t} = R_i - \frac{\partial P}{\partial x_i}. \tag{2.19}$$

$$\frac{\partial u_i}{\partial x_i} = 0 \tag{2.20}$$

$$\frac{\partial \Theta}{\partial t} = R_t. \tag{2.21}$$

Since, R_i and R_t are functions of u_i and Θ respectively, we have a system of five equations and five unknowns (u_i, Θ, and p) that can be solved numerically.

The numerical method used to obtain the wind and temperature field are described in detail by Moeng.[14] In order to solve the system, the pressure must be determined for the given wind and temperature fields. Taking the divergence of Eq. 2.19 yields a Poisson equation for the pressure,

$$\frac{\partial^2 P}{\partial x_i^2} = -\frac{\partial}{\partial t}\left(\frac{\partial u_i}{\partial x_i}\right) + \frac{\partial R_i}{\partial x_i}. \tag{2.22}$$

The incompressibility condition from Eq. 2.20 has not been applied to Eq. 2.22 yet to allow the numerical possibility that physical processes, initial conditions, or numerical errors have caused the wind field to stray from being nondivergent. Numerically approximating the time derivative in Eq. 2.22 gives,

$$\frac{\partial^2 P}{\partial x_i^2} = -\left(\left.\frac{\partial u_i}{\partial x_i}\right|_{t+\delta t} - \left.\frac{\partial u_i}{\partial x_i}\right|_{t} \right) + \frac{\partial R_i}{\partial x_i}. \tag{2.23}$$

Here the divergence at the next time step must vanish to obey the incompressibility condition, however, there may still be some non-divergence in the current wind field so Eq. 2.23 becomes,

$$\frac{\partial^2 P}{\partial x_i^2} = \left.\frac{\partial u_i}{\partial x_i}\right|_{t} + \frac{\partial R_i}{\partial x_i}. \tag{2.24}$$

For simplicity, the terms on the right-hand side of Eq. 2.24 are denoted as $R(x, y, z)$,

$$\frac{\partial^2 P(x,y,z)}{\partial x_i^2} = R(x,y,z). \tag{2.25}$$

For a periodic, Cartesian domain in x and y, the solution takes the form,

$$P = \sum_{\kappa} \hat{p}(z) e^{i(\kappa_1 x + \kappa_2 y)} \tag{2.26}$$

$$R = \sum_{\kappa} \hat{r}(z) e^{i(\kappa_1 x + \kappa_2 y)} \tag{2.27}$$

where the summation is over all wavenumbers that are represented on the model grid. For simplicity the summation notation will be dropped. Applying Eqs. 2.26 and 2.27 to Eq. 2.25 results in an inhomogeneous Helmholtz equation,

$$\frac{\partial^2 \hat{p}(z)}{\partial z^2} - (\kappa_1^2 + \kappa_2^2)\hat{p}(z) = \hat{r}(z). \tag{2.28}$$

The vertical derivative in Eq. 2.28 can be approximated as,

$$\frac{\partial^2 \hat{p}(z)}{\partial z^2} \sim \frac{\left.\frac{\partial \hat{p}}{\partial z}\right|_{z+\delta z/2} - \left.\frac{\partial \hat{p}}{\partial z}\right|_{z-\delta z/2}}{\delta z} \sim \frac{\hat{p}(z+\delta z) - \hat{p}(z)}{\delta z_+ \delta z} - \frac{\hat{p}(z) - \hat{p}(z-\delta z)}{\delta z_- \delta z}, \tag{2.29}$$

so that Eq. 2.28 can be approximated as,

$$\frac{1}{\delta z_+}\hat{p}(z+\delta z) - \left(\frac{1}{\delta z_+} + \frac{1}{\delta z_-} + |\kappa|^2\right)\hat{p}(z) + \frac{1}{\delta z_-}\hat{p}(z-\delta z) = \delta z \hat{r}(z). \tag{2.30}$$

The right-hand side of Eq. 2.25 is computed and its FFT yields $\hat{r}$. Given $\hat{r}$, a tridiagonal solver is used to solve Eq. 2.30 for $\hat{p}$. The modified pressure P is obtained by transforming the resulting $\hat{p}$ back to real space. The resolvable kinematic pressure is found using Eq. 2.18.

2.6 The Code

The LES code used in this project was developed by Martin Otte [29] and based on Chin-Hoh Moeng's LES [14]. It was used by the National Center for Atmospheric Research (NCAR) and Penn State. The NCAR/Penn State LES uses Kosovic's SGS model [17], that incorporates kinetic energy transfer from smaller scales to larger as well as the usual energy transfer from larger scales to smaller. The code has also been parallelized. Additionally, the code has been modified to automatically convert the modified pressure back to the resolvable kinematic pressure.

CHAPTER 3: CROSS-CORRELATION STUDIES

3.1 Data Analysis

Wind gusts are local coherent structures occurring in an incoherent signal. The spectrum is commonly used to characterize the energy content of turbulence in an incoherent wind field. The Fourier transform of an incoherent velocity field is a decomposition into waves of different wavelengths and random phases with each wave associated with a single Fourier coefficient. A coherent wind gust, however, is associated with many Fourier coefficients with non-random phases. A spectrum of an incoherent wind field is not sufficient in identifying intermittent coherent structures in the wind. A more sophisticated transform is needed to decompose a velocity field into discrete units instead of waves. Additionally, cross-correlating spectra could yield high correlation coefficients when the frequency content of the two signals were similar even if the time evolution of the frequencies were different.

A potential solution to these problems is to use the short term Fourier Transform (STFT). This assumes that some portion of a non-stationary signal is stationary. However, STFT introduce resolution problems. If a narrow window is used to get good time resolution, it yields poor frequency resolution. Likewise, wide windows give good frequency resolution but poor time resolution and may be so wide that they violate the condition of stationarity. For gusts this is far from ideal because they are short duration signals with small spacing between peak frequencies.

Wavelet transforms have been developed that can identify gusts in a wind fields. Previous research has used continuous wavelet transforms (CWTs) to identify and study gusts.[30] Gust candidates will be identified visually and a CWT of this event will be performed. A CWT of the pressure on the ground below the gust candidate will also be performed.

This will yield the frequencies contained in each gust and pressure response along with the corresponding amplitude and time. A cross correlation between the two CWTs provides an estimate of the relationship between the two signals.

3.1.1 Continuous Wavelet Transform

The continuous wavelet transform (CWT) was developed as an alternative approach to the STFT to overcome the resolution problem. The main difference between CWTs and STFTs is that the width of the window is changed as the transform is computed for every single spectral component.

The CWT of a signal $f(t)$ is defined as,

$$\tilde{f}(t) \equiv \int_{-\infty}^{\infty} \psi^{*}_{s,t}(u) f(u) du \tag{3.1}$$

where

$$\psi_{s,t}(u) \equiv \psi_s(u-t) = |s|^{-1/2} \psi \left(\frac{u-t}{s} \right),$$

is the mother wavelet which serves as a source function to generate the daughter wavelets, which are just translations by t of the mother wavelet. Here s is a scale factor that is related to the Fourier frequency F as

$$F = \frac{\omega_0 + \sqrt{2+\omega_0^2}}{4\pi s}, \tag{3.2}$$

where ω_0 is the dimensionless frequency, taken to be a value that satisfies the admissibility condition $\hat{\psi}(0) = 0$ [31] [32].

Unlike Fourier Transforms, the CWT constructs a representation of a signal that yield time, frequency, and amplitude components providing very good frequency localization.

3.1.2 Wavelet Cross Correlation

The CWTs are computed for the velocity field u at altitude range associated with the gust and the pressure field p on the ground below. The two CWTs will then be cross-correlated,

$$(\tilde{u} \star \tilde{p}) \equiv \int_{-\infty}^{\infty} \tilde{u}^*(\tau)\tilde{p}(t+\tau)d\tau. \tag{3.3}$$

Here τ is lag and t is time. This will provide an estimate of how related these two signals are.

In essence, $\tilde{p}$ is slid along the t-axis and the integral of its product with $\tilde{u}$ is calculated at each time. When the functions match it means that they have the same frequency content. When this happens the value of $(\tilde{u} \star \tilde{p})$ is maximized. This means that the time evolution of the frequency spectra for u up high at a time t is similar to the time evolution of the frequency spectra for p near the ground at a time $t + \tau$.

3.2 Science Run I

A sunny day with sparse cloud cover and medium winds was generated using a CBL LES. The LES domain was a 2500 m square in the horizontal and 1000 m deep. The LES code used 1250 x 1250 grid points in the horizontal plane for the first 200 m of altitude giving it a horizontal resolution of 2500 m $\div$ 1250 = 2 m. The remaining 800 m of altitude used 64 x 64 grid points giving it a horizontal resolution of 2500 $\div$ 64 $\approx$ 39 m. The vertical resolution was 2 m up to z = 10 m but is changed to 10 m for the remaining levels from z = 10 m to 200 m. A geostrophic wind speed of 10 m/s in the x-direction was used to force convection. The surface temperature flux was 0.24 K m/s and the capping inversion height was approximately 600 m. The initial inversion strength was 0.1 K/m and the temperature gradient above the inversion was 0.002 K/m. The data were analyzed at a model times between 3000 $-$ 4000 s. A LES reaches equilibrium when the altitude versus the heat flux becomes nearly linear under the capping inversion as shown in Fig. 3.1 for science run I.

As a test to see if the simulation was generating gusts that agreed with experimental data, a virtual tower of points from the LES data was chosen at altitudes ranging from 10 m to 119 m and the velocities at each point were extracted over 1000 s. Turbulent intensities were used rather than gust factors. Turbulent intensities are the same as gust factors but without restriction on the duration of the elevated wind. Turbulent intensities at each time step were calculated using a 300 s mean wind speed. The first turbulent intensity was calculated after 300 s so that a mean wind speed could be determined and the mean wind speed was recalculated at each second thereafter. The final turbulent intensity was calculated at 1000 s. This provided 700 data points for each of the 19 elevations yielding a total number of 13,300 data points. Fig. 3.2 shows a plot of the turbulent intensity versus the altitude. The turbulent intensities trend down exponentially with increasing altitude in agreement with the White Sands tests discussed in Chapter 1. The mean wind field increases with altitude at a faster rate than the turbulent intensity does. Further away from the ground there is less shear to slow the mean wind velocity and so it increases with altitude. Also, further away from the heated ground there is less turbulent energy being supplied by convective processes and so the ratio between the maximum gust velocities and the mean wind field become smaller.

3.3 Results

Three gust candidates from this LES run are presented. The candidates were visually identified through graphical analysis of animations that are similar to the velocity contour plots shown in Figs. 3.4, 3.9, and 3.14. Once a coherent velocity structure was identified visually, the ground level in the region below was checked for a coherent pressure footprint that moved at a similar group velocity to the coherent velocity event above. To diminish the chance that it was coincidence that these signals were visually similar, CWTs of the velocity event and the pressure event were cross-correlated to check if the time evolution of their frequency content was similar. Contour plots of the magnitude versus the horizontal

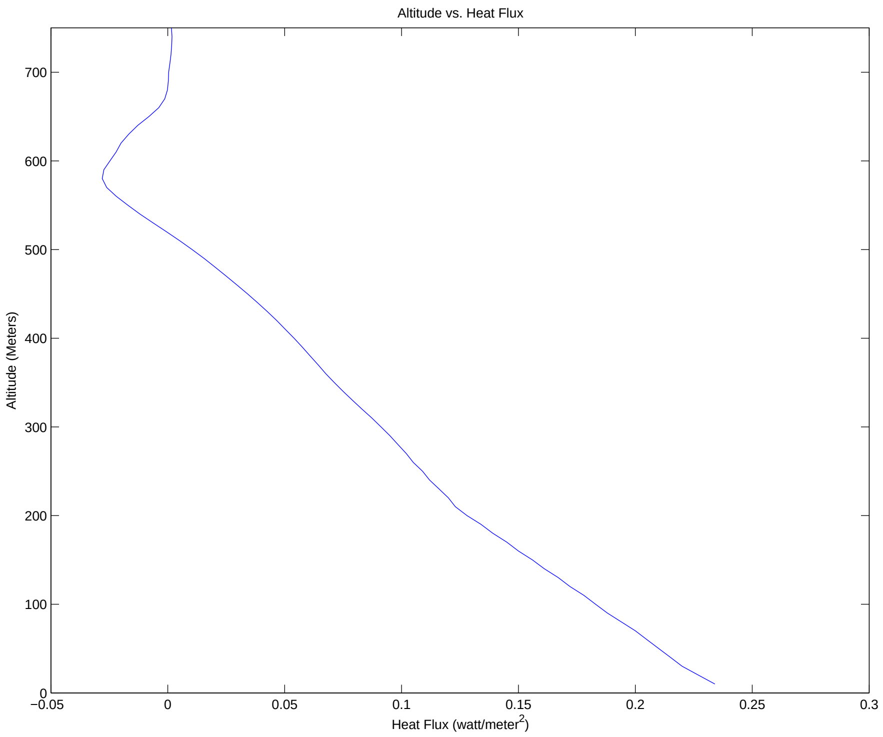

Figure 3.1. Science Run I: Altitude vs. Heat Flux (wt). From the plot, the capping inversion is at $z \approx 580$ m. The nearly linear behavior beneath the capping inversion indicates that the simulation has reached equilibrium.

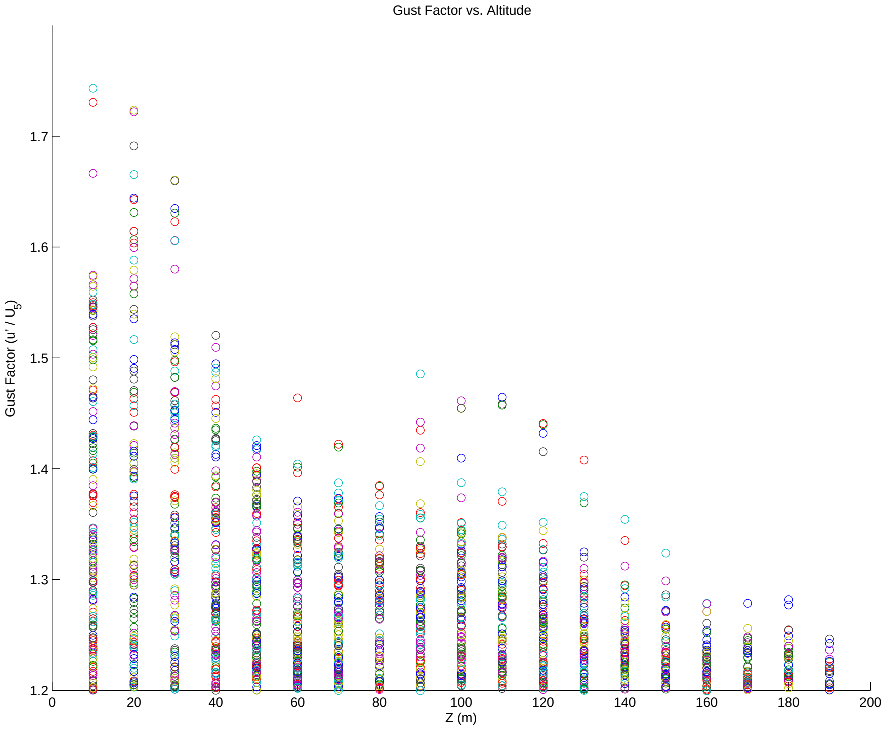

Figure 3.2. Gust factors plotted against altitude along a tower of data collected from the LES.

plane for the coherent pressures and associated velocities of each candidate were analyzed to compare their horizontal paths.

3.3.1 Candidate A

A time series of pressure at the ground and velocities at various elevations were extracted at $y = 400$ m for 1250 grid points in the x-direction. Fluctuations in the pressure time series that flowed downstream faster than the mean flow were identified. One such example, candidate A, is shown in Fig. 3.3a and downstream in Fig. 3.3b on pg. 32.

This particular pressure fluctuation is propagating downstream at 4.0 m/s. The mean flow at the ground is 3.0 m/s. Fig. 3.4 on pg. 33 shows a vertical slice of x velocity for candidate A at several time steps. Fluctuations from the velocity time series at each elevation were analyzed for signals that matched the pressure fluctuations in x velocity, general horizontal location, and near time of occurrence is also shown in blue in Fig. 3.3a and downstream in Fig. 3.3b. This shows that these signals are visually and spatially similar and they occur at the same time. The associated velocity fluctuation is propagating at the same speed at an altitude of 30 m in a flow with a mean velocity of 6.6 m/s that peaks at 10.6 m/s. The time series were converted to CWT space as shown in Fig. 3.3c. Frequencies that corresponded to a range of altitudes near where the velocity fluctuation occurred were isolated for each time series and the time evolution of their frequency structure was compared using cross-correlations as shown in Fig. 3.3d. The cross-correlation between the CWTs of the pressure at the ground and the velocity at 30 m had a correlation coefficient that peaked at approximately 0.9 and fell off as the signals moved downstream and broke apart.

Contour plots of the pressure and velocity signals from Figs. 3.3a and 3.3b were constructed and animated to further analyze the signal evolution. Two such slices of the animation that correspond to the pressure at the ground at times shown in Figs. 3.3a and 3.3b are shown in Figs. 3.6 and 3.5 on pgs. 35 and 34.

The gust candidate moves diagonally through the horizontal plane triggering secondary structures as it propagates. The pressure event moves along a similar diagonal path in the x-y plane. On the ground during event A, both the instantaneous velocities and the mean velocities have a negative y-component, however, the coherent pressure structure is moving with a positive y-velocity. The associated velocity event at z = 30 m behaves in a similar manner.

The maximum velocity and corresponding location during gust A were found. The ten minute mean velocity at this location was subtracted from the total velocity yielding the fluctuating part of the velocity u'. u' is shown plotted against the duration time. The red line represents the the zero fluctuation or the ten minute mean U. There are two main peaks during this event. The first peak has a duration of 6 s and the difference between the maximum and the minimum is 8 m/s. This ten minute mean velocity is 5 m/s and the peak velocity is 12 m/s yielding a gust factor of 2.4. This event fits the criteria discussed in Chapter 1 to be identified as a gust. The second peak has a duration of 20 s and the difference between the maximum and the minimum is 4.5 m/s. The gust factor for this peak is 2.2. This second peak meets the criteria for gust classification as well.

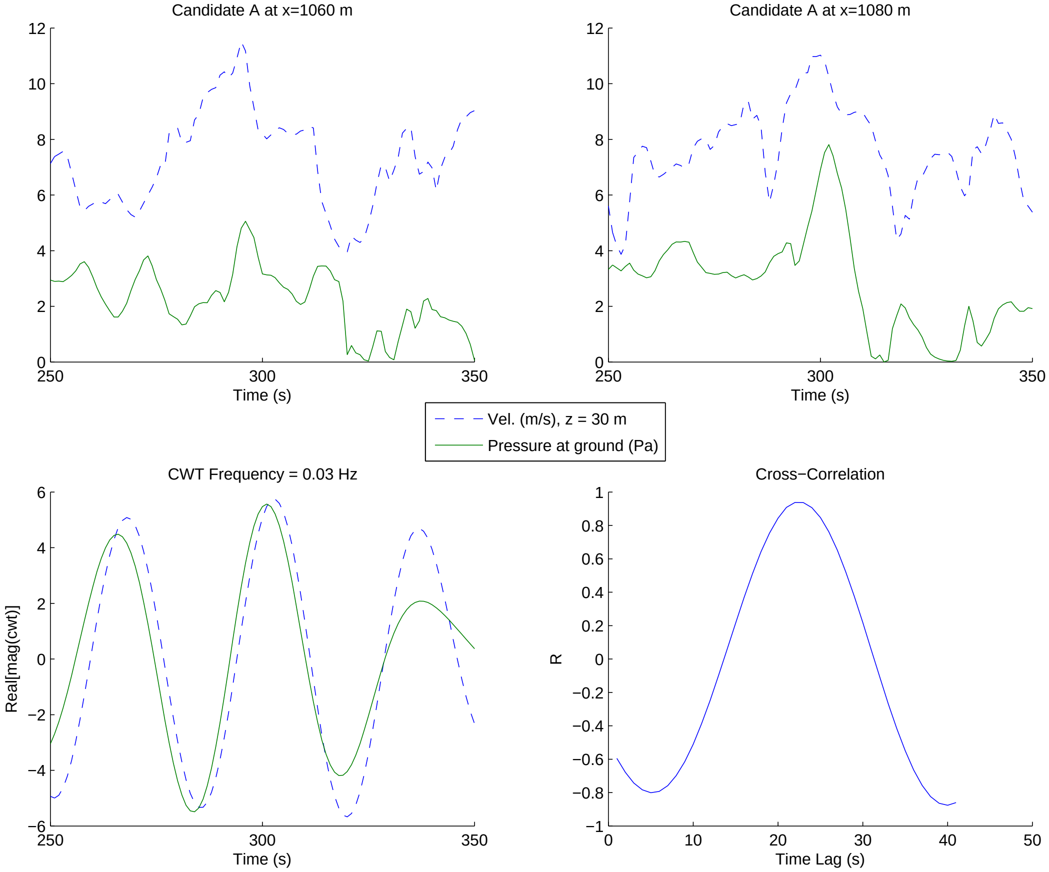

Figure 3.3. Candidate A: (a) V and P versus t at x=1060m. (b) V and P versus t at x=1080m. (c) CWTs of signals from Fig. 3.3b. (d) Cross-correlation of the CWTs from Fig. 3.3c. All pressures are $\sqrt{P^2}$.

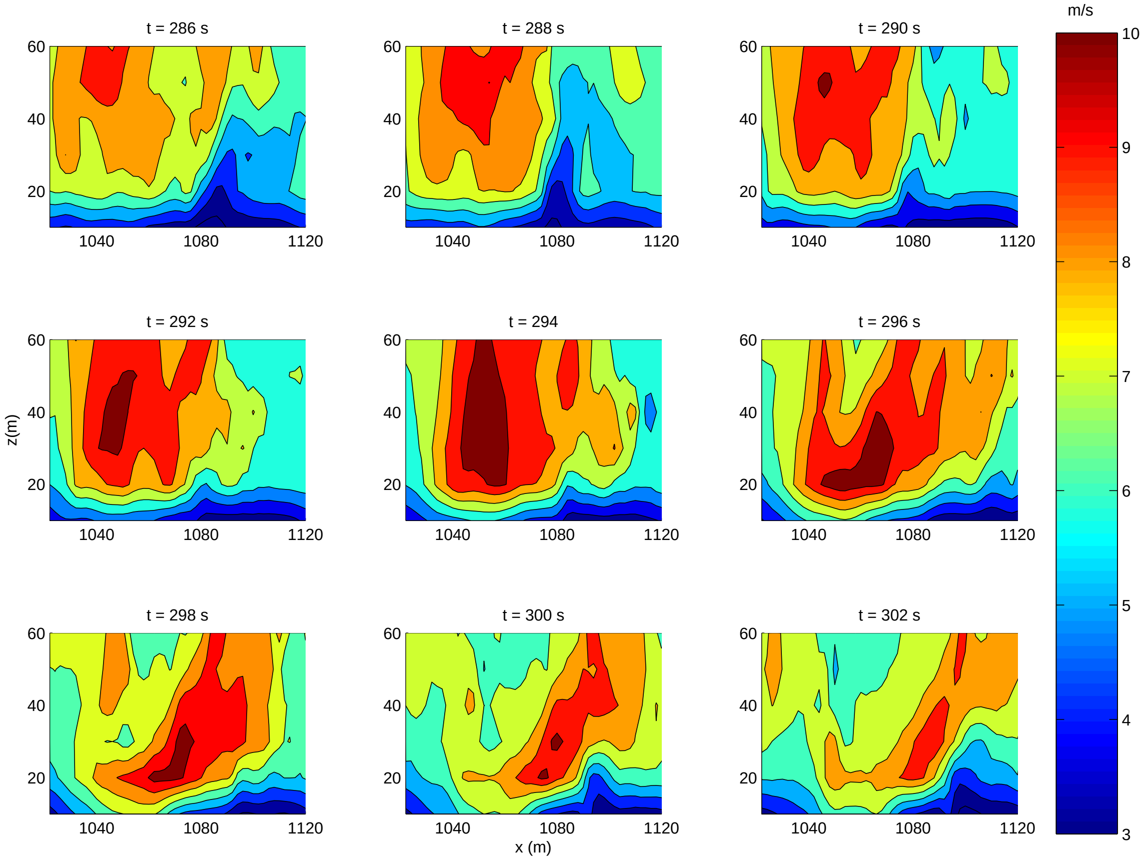

Figure 3.4. Candidate A: Altitude vs. x direction plot of velocity in m/s for times $286 - 302$ s.

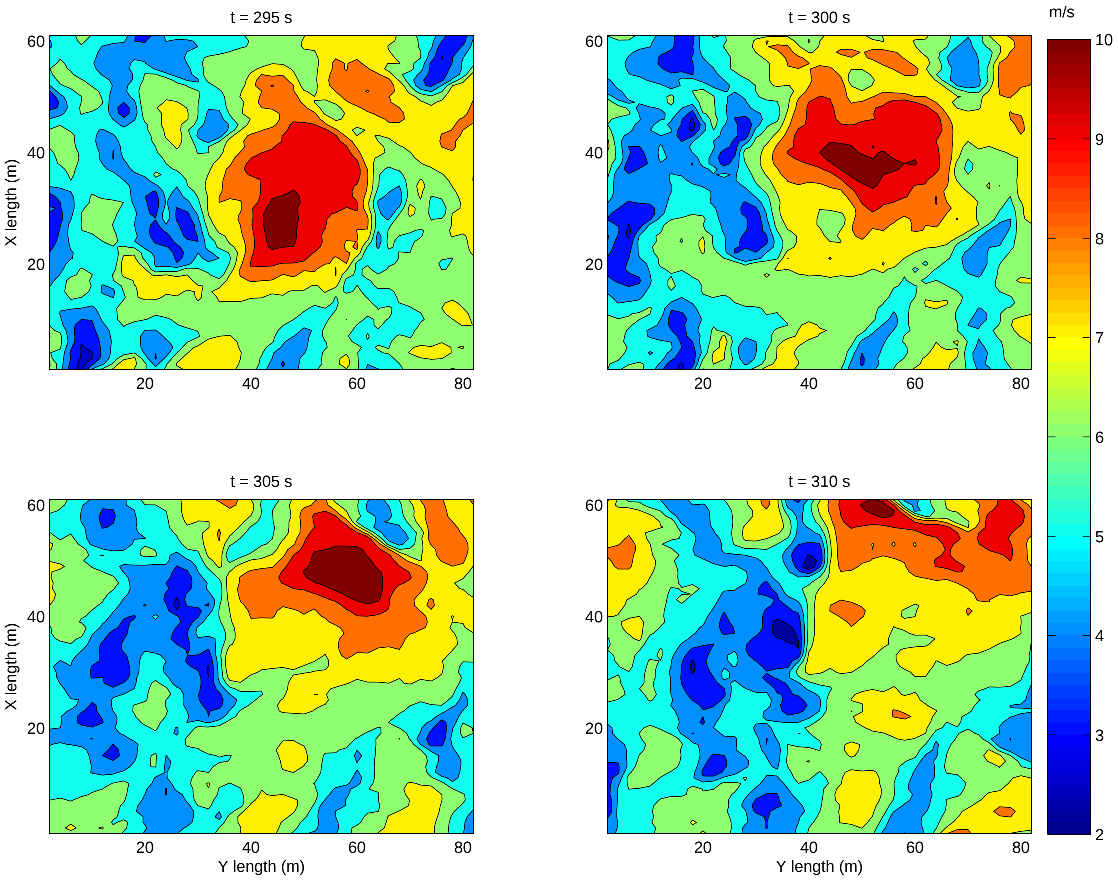

Figure 3.5. Candidate A: x-y Contour plot of the velocity event at z = 30 m from Fig. 3.3a.

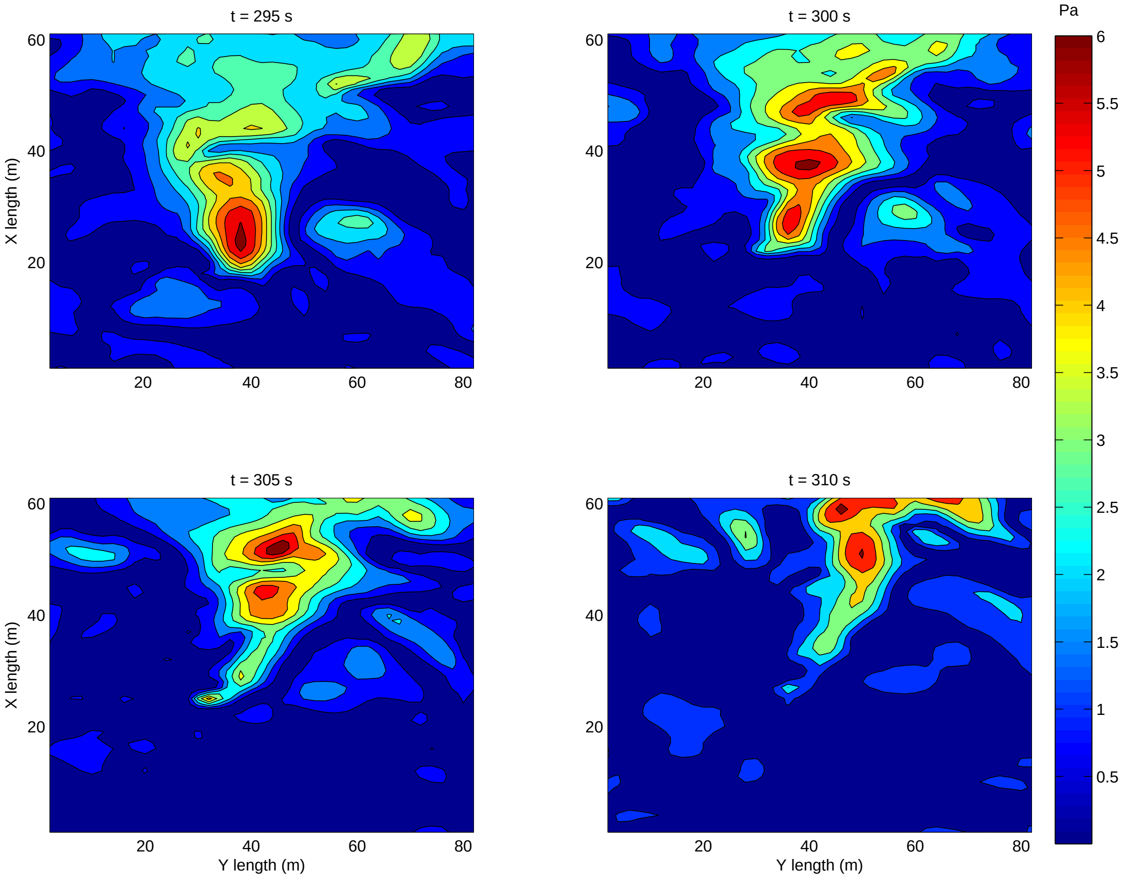

Figure 3.6. Candidate A: x-y Contour Plot of $\sqrt{P^2}$ on the ground from Fig. 3.3a.

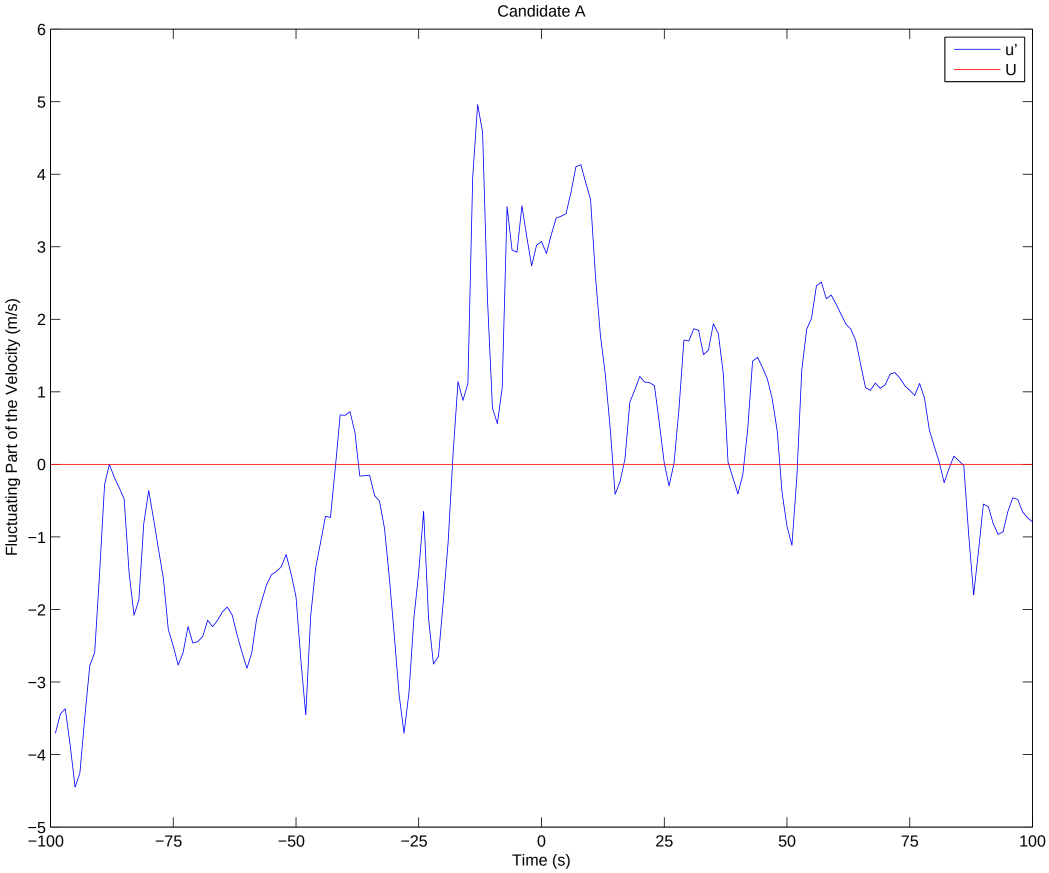

Figure 3.7. Gust A: The fluctuating part of the velocity is shown at each time step for the location where the maximum occurs at z = 30 m during candidate A.

3.3.2 Candidate B

A second example, candidate B, is shown in Figs. 3.8-3.10. Again the solid line shows the pressure at the ground while the dotted line shows the associated velocity. The peak velocity is 10.6 m/s at an altitude of 100 m. Fig. 3.9 on pg. 39 shows vertical slices of the velocity at several time steps during the event. The peak in Fig. 3.8a at x = 820 m travels 20 m downstream in 5 s with a velocity of 4 m/s as shown in Fig. 3.8b.

The mean velocity on the ground is 2.9 m/s while the mean at z = 100 m was 7.5 m/s. The signal was again transformed to CWT space as shown in Fig. 3.8c and cross-correlated as shown in 3.8b. For candidate B, the cross-correlation between the CWTs of the pressure at the ground and the velocity at 100 m had a correlation coefficient that peaked at approximately 0.80 and fell off as the signals moved downstream. Again, contour plots for candidate B are shown in Figs. 3.10 and 3.11. As with candidate A, the events that are correlated in the pressure at the ground and the velocity at 100 m follow similar paths in the x-y plane. At some point the velocity event at z = 100 m for candidate B breaks off into two large pieces and the associated pressure event on the ground does the same.

Fig. 3.12 shows the fluctuating part of the velocity during the duration of candidate B centered at the main peak. The difference between the maximum peak at 0 s and the minimum at 10 s is 3.7 m/s which is just short of the 4 m/s from the criteria for gust identification discussed in Chapter 1. However, due to candidate B meeting the duration requirements and because it was so close in the peak-to-lull difference it is going to be considered a gust like event for the sake of this analysis. The gust factor is 1.6 for event B.

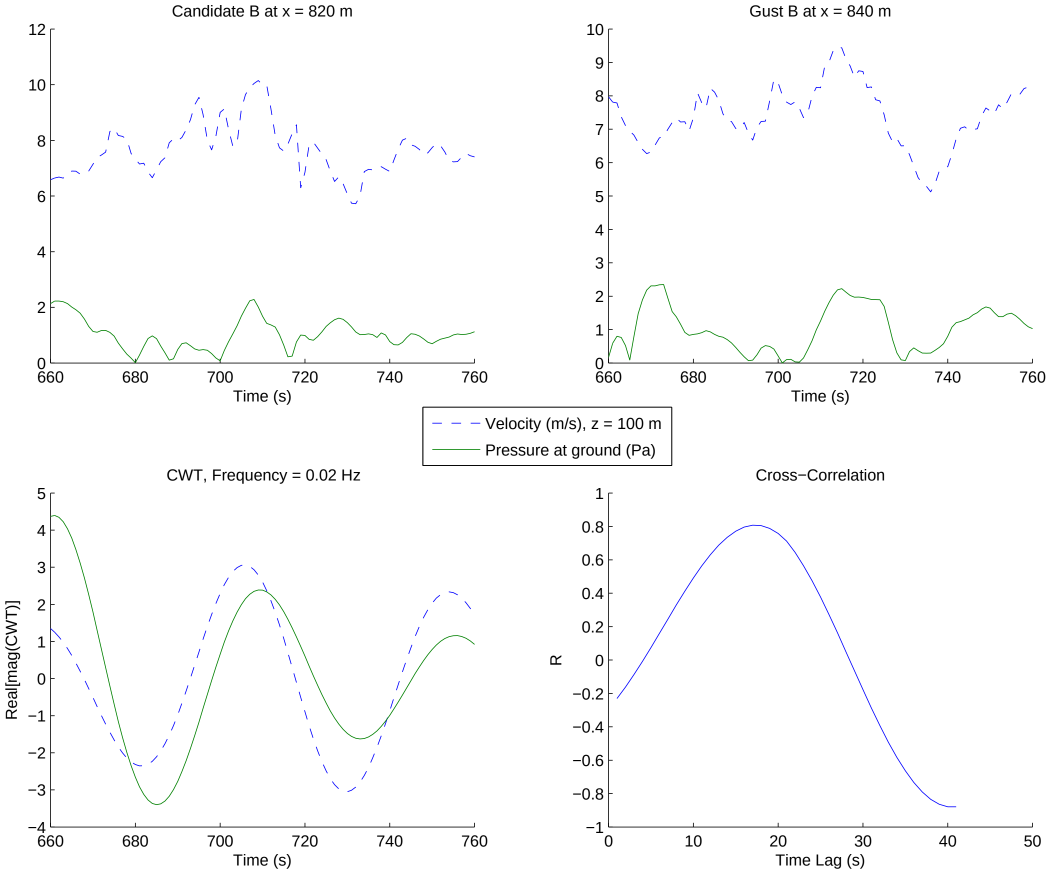

Figure 3.8. Candidate B: (a) V and P versus t at x=820 m. (b) V and P versus t at x=840 m. (c) CWTs of signals from Fig. 3.8a. (d) Cross-correlation of the CWTs from Fig. 3.8c. All pressures are $\sqrt{P^2}$.

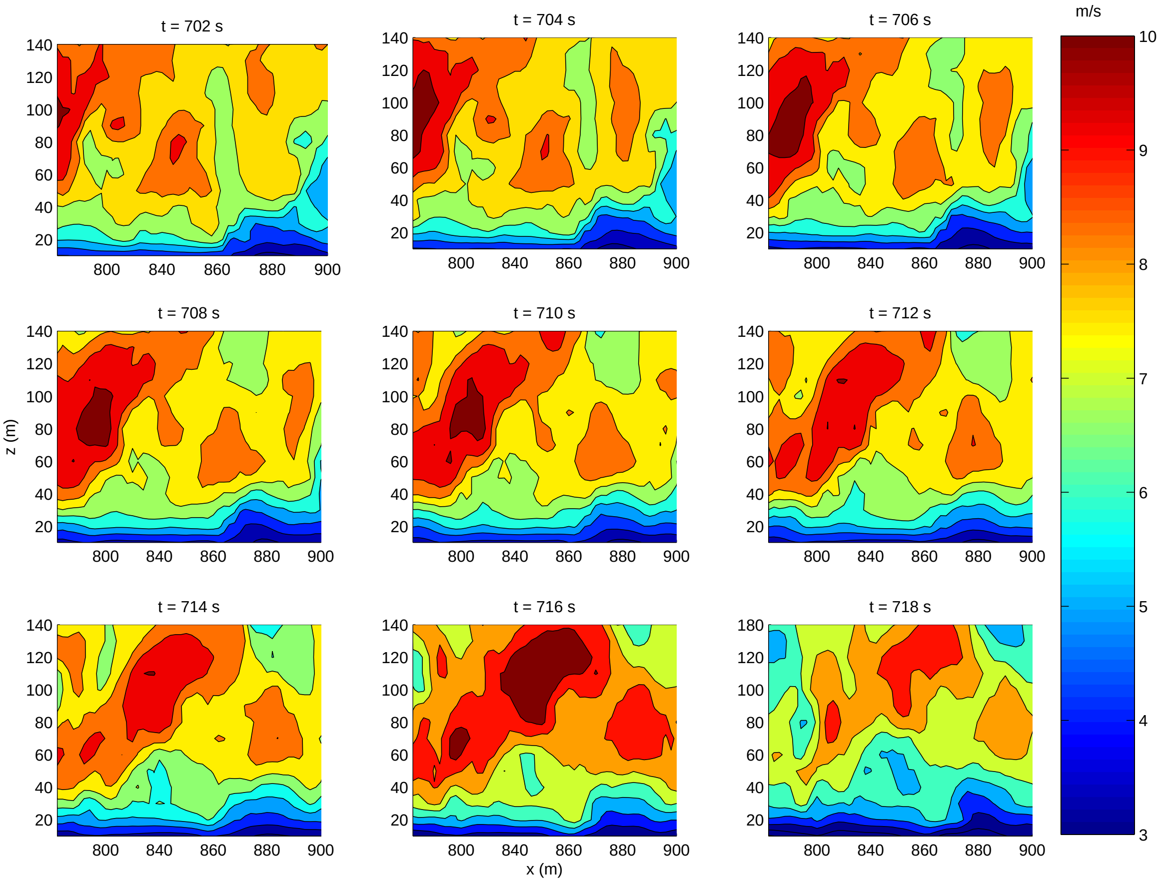

Figure 3.9. Candidate B: Altitude vs. x direction plot of x velocities in m/s for times $702 - 718$ s.

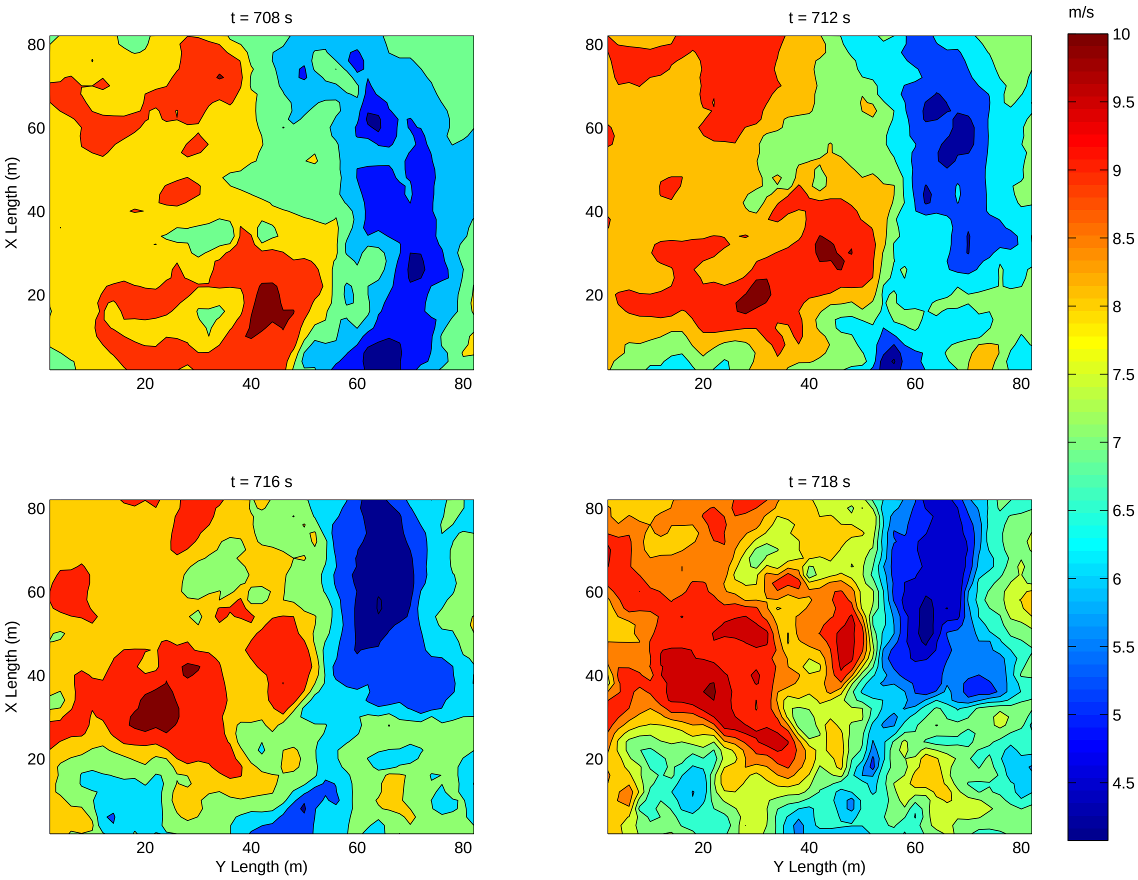

Figure 3.10. Candidate B: Horizontal slice of velocity (m/s) at z = 100 m from Fig. 3.8a.

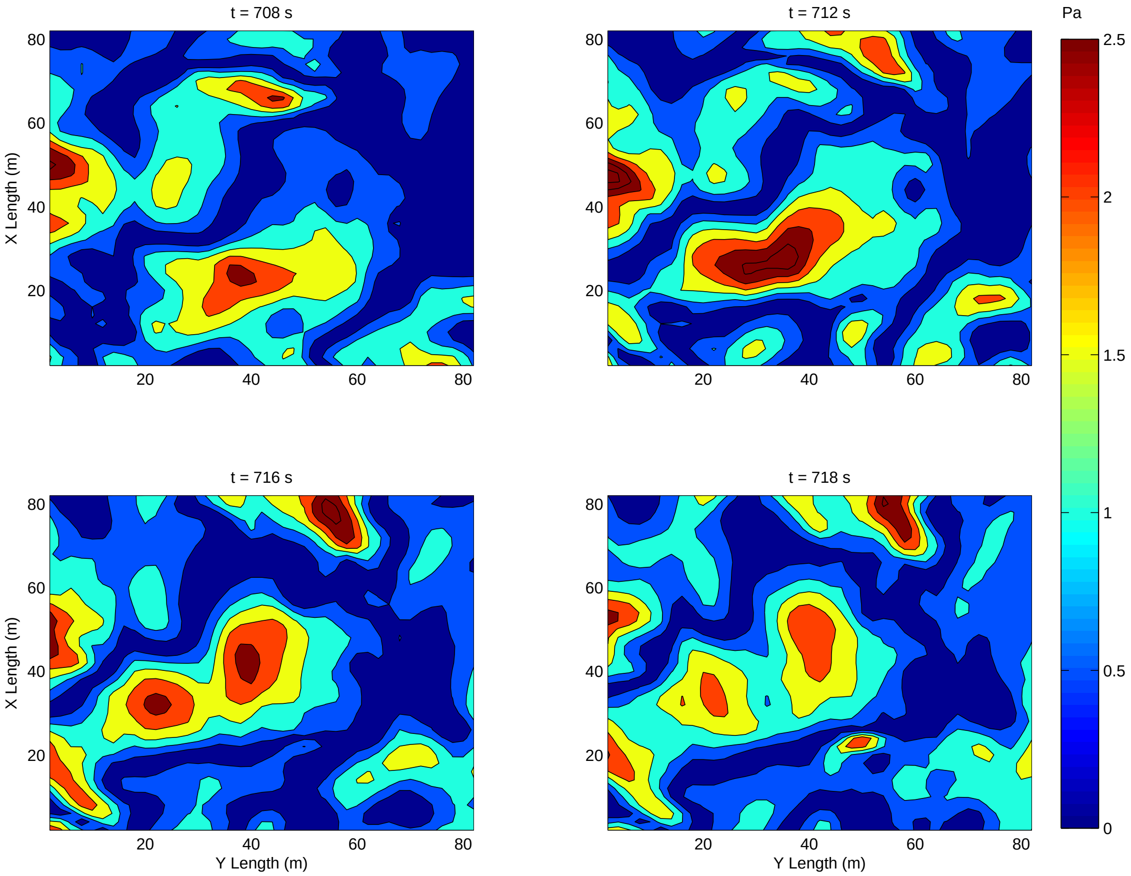

Figure 3.11. Candidate B: Horizontal slice of $\sqrt{P^2}$ in Pa on the ground from Fig. 3.8a.

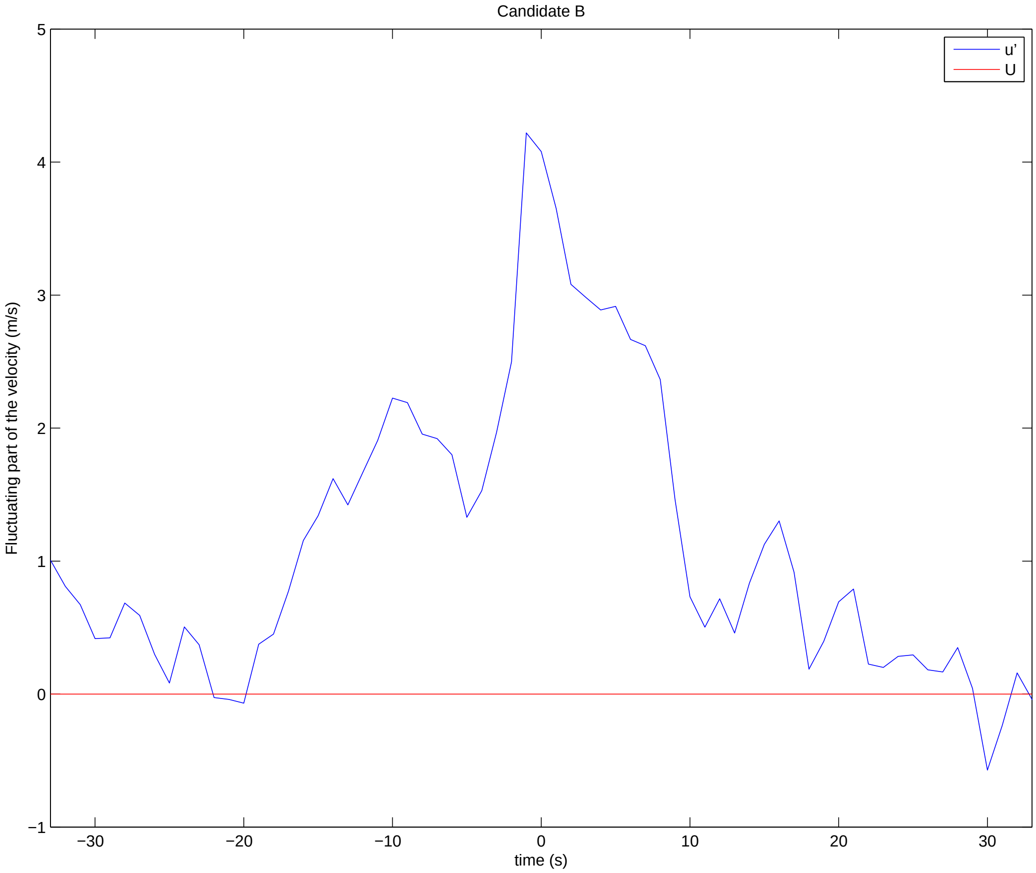

Figure 3.12. Gust B: The fluctuating part of the velocity is shown at each time step for the location where the maximum occurs at z = 100 m during candidate B.

3.3.3 Candidate C

A third example, candidate C, is shown in Figs. 3.13-3.15 starting on pg. 44. The peak in the pressure at the ground is propagating with a velocity of 5.3 m/s as shown in Fig. 3.13 a-b. The mean velocity of the wind at the ground is 2.9 m/s. This pressure fluctuation is associated with a velocity event at z = 100 m that is propagating with a similar speed with a peak gust speed of 12.15 m/s. The cross-correlation of the CWTs yields a maximum correlation coefficient of approximately 0.75 which again falls off as the disturbances travel downstream. Contour plots for candidate C are shown in Figs. 3.15 and 3.16. These plots show that the velocity disturbance at 100 m and the pressure disturbance at the ground follow similar paths in the x-y plane.

Fig. 3.17 shows the fluctuating part of the velocity during the time of its duration. The plot is centered on the main maximum. There are two separate peaks here. If the event is treated as one peak the event fails the gust criteria discussed in Chapter 1. The first peak at -5 s differs from the minimum at -20 by 3.6 m/s. The second peak at 0 s differs from the minimum at 13 s by 4.1 m/s. Both of these events have durations less than 20 s. The gust factor for the main peak at 0 s is 1.8 and for the smaller peak the gust factor is 1.6.

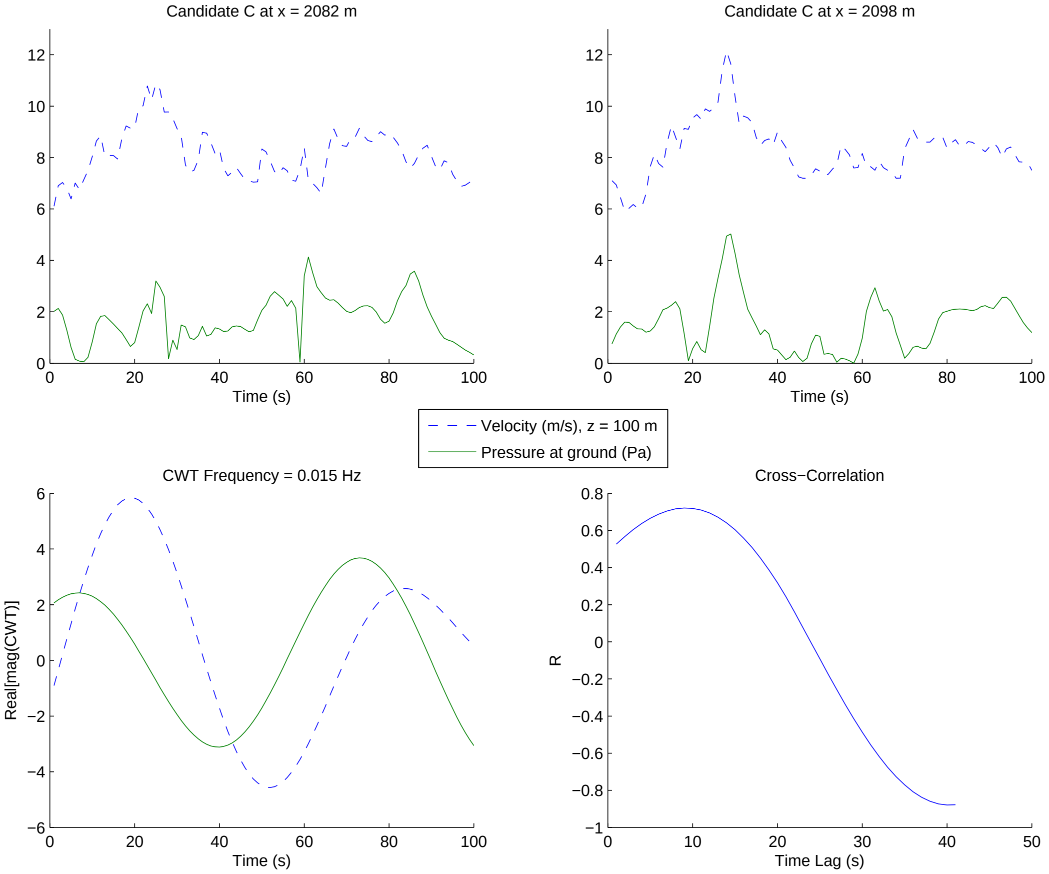

Figure 3.13. Candidate C: (a) V and P versus t at x=2082 m. (b) V and P versus t at x=2098 m. (c) CWTs of signals from Fig.12b. (d) Cross-correlation of the CWTs from Fig. 12c. All pressures are $\sqrt{P^2}$.

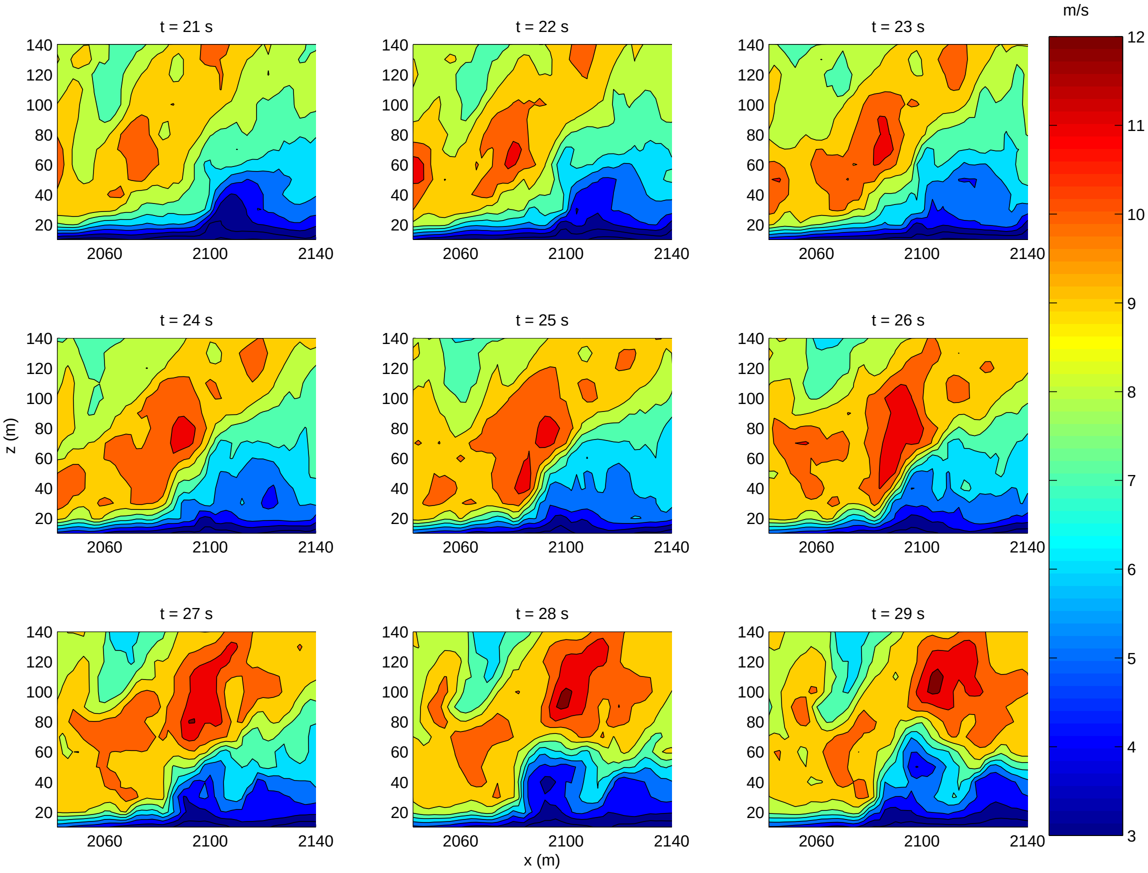

Figure 3.14. Candidate C: Altitude vs. x direction plot of x velocities in m/s for times $21 - 29$ s.

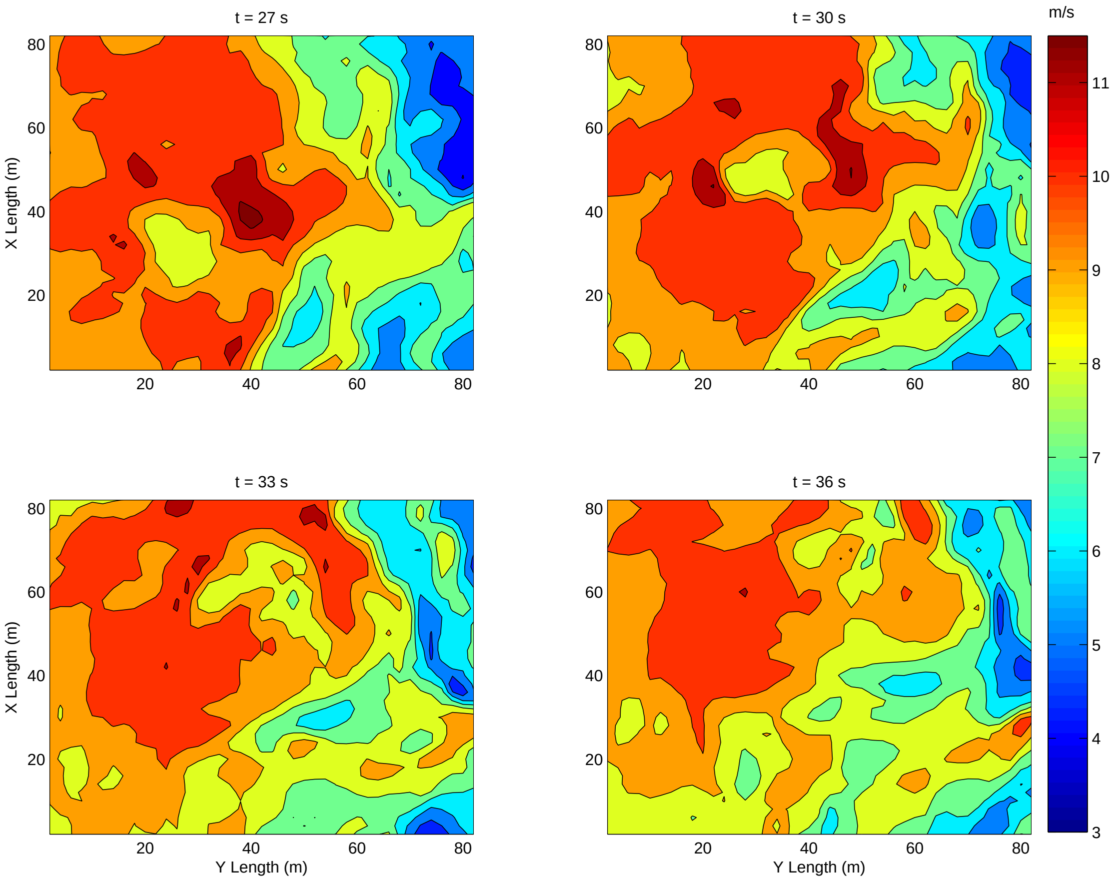

Figure 3.15. Candidate C: Horizontal slice of the velocity (m/s) at z = 100 m from Fig. 3.13a.

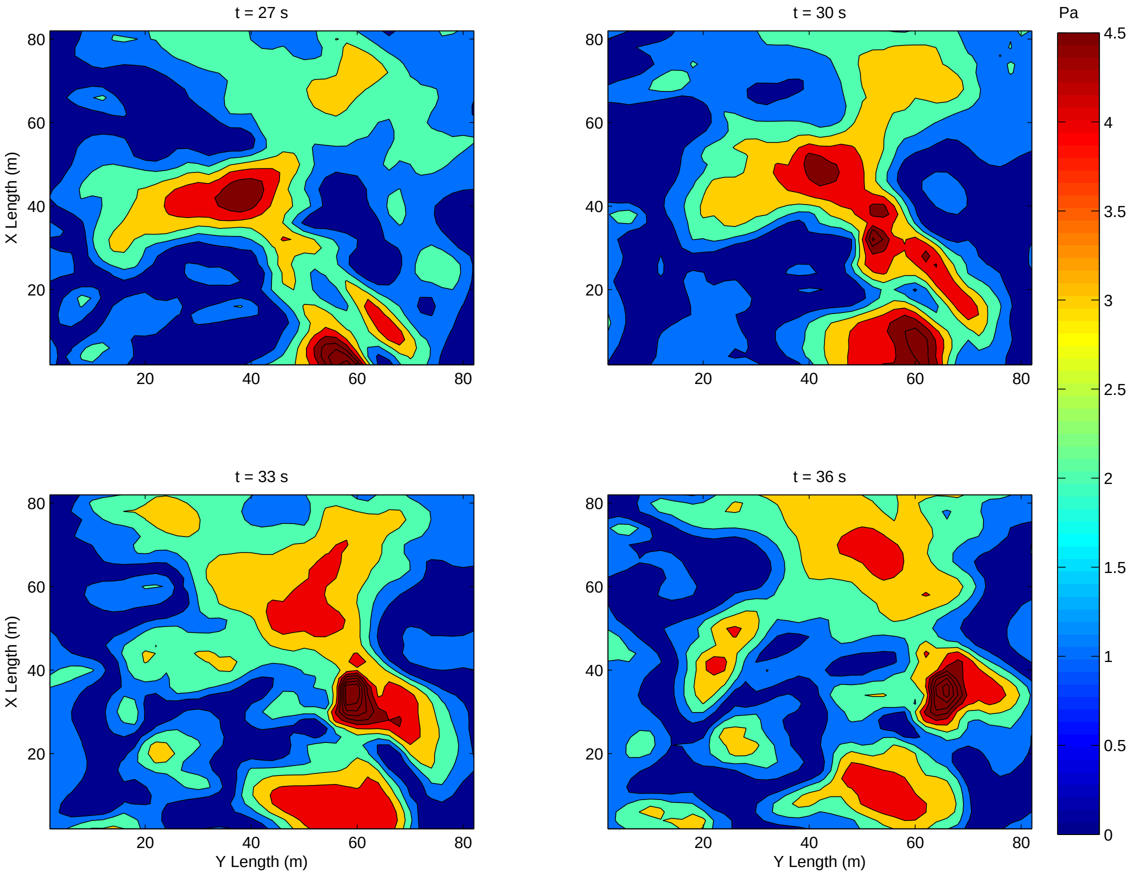

Figure 3.16. **Candidate C: Horizontal slice of $\sqrt{P^2}$ in Pa on the ground from Fig. 3.13a.**

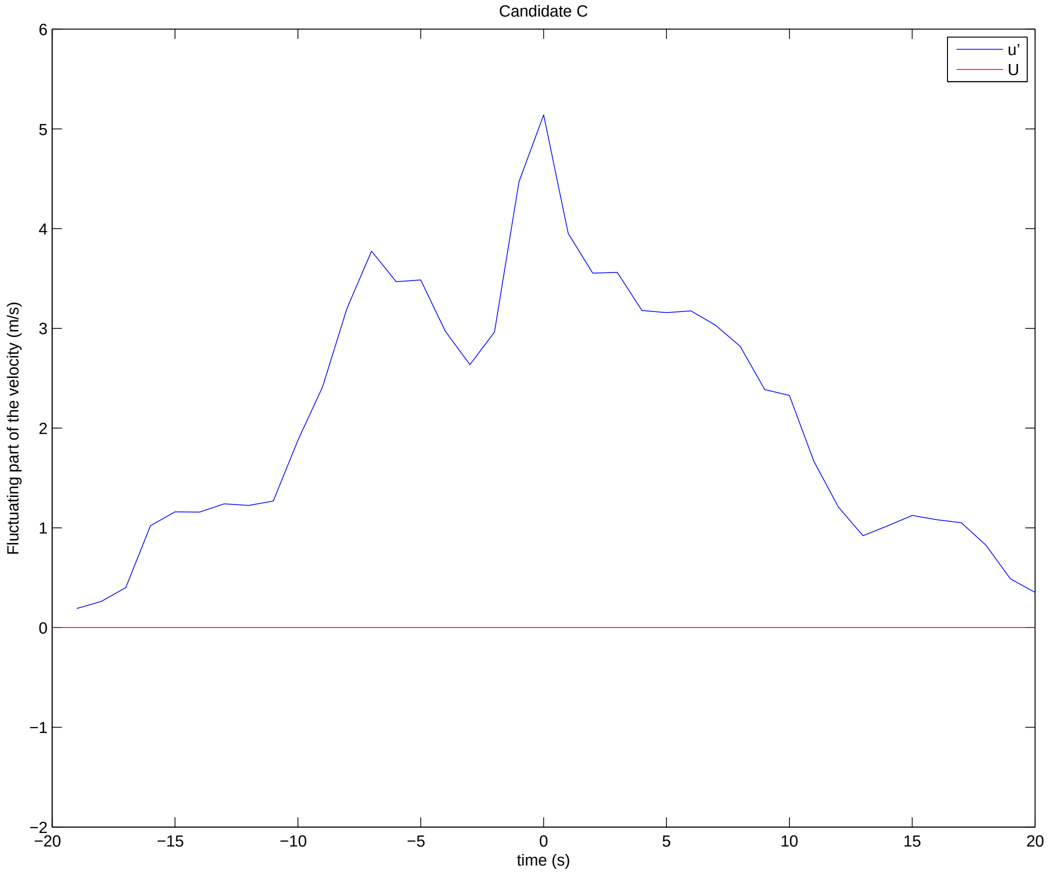

Figure 3.17. Gust C: The fluctuating part of the velocity is shown at each time step for the location where the maximum occurs at z = 100 m during candidate C.

3.4 Summary of Cross-Correlation Studies

The cross-correlation studies show that elevated wind velocities such as gusts do contribute to pressure fluctuations on the ground. The pressure fluctuations move at approximately the same group velocities as the cluster of the elevated wind gusts as well as in the same direction. These studies have shown that clusters of local velocities propagate with a group velocity. The maximum of the local velocities are the maximum gusts in the cluster that are being propagated downstream by the mean flow at the group velocity. For the duration of this work the local velocities, or gusts, are referred to as the maximum gusts and the "gust speed" refers to the speed of the cluster of gusts. The time evolution of the frequency content of the elevated velocity signals are strongly correlated with the time evolution of the frequency content for the corresponding pressure signals on the ground below. A summary of velocities and correlation coefficients can be found in Table 3.1 on pg. 50.

These studies offer some starting points for array and processing design of a detection system. These large pressure fluctuations have several behaviors in common. Each of them consists of a coherent cluster of pressure peaks that move across the surface along an ordered path. The clusters do not abruptly change direction. The group propagation velocities of these moving pressure clusters exceed the wind velocities on the ground and are often in a different direction altogether. The approximate group velocities of each event provide an estimate of what the area and sensor spacing should be for a ground based array. For example, consider a pressure peak that is moving at a velocity of 5 m/s on the ground in the x direction. If the spacing between the sensors is 10 m and the array is 20 x 20 m^2 and data is recorded every 2 s, the processing script might completely miss the gust.

With this information in mind, the prescription for elevated gust identification from pressure measurements on the ground will be to search for pressure peaks which move along an ordered direction and that exceed the wind velocity at the surface. With these parameters a rudimentary array design will be implemented and optimized through testing against candidate A.

Table 3.1. Table of velocities in m/s. U is a mean velocity, u is velocity, z is the altitude of the maximum of the velocity event, and R_{peak} is the peak correlation coefficient.

$Candidate$	A	B	C
z (m)	30	100	100
u_{peak} (m/s)	10.6	10.15	12.15
u_{group} (m/s)	4.0	4.0	5.3
U_{ground} (m/s)	3.0	2.9	2.9
U_{height} (m/s)	6.6	7.5	7
R_{peak}	0.9	0.8	0.75

CHAPTER 4: GROUND-BASED ELEVATED GUST TRACKER

In order for a ground based array to be sensitive to elevated gust induced pressures, a processing method must be devised to interpret the data collected by the array. A processing routine that monitors pressures through a ground based array is presented in this chapter. It is tested using a simulated array within the LES data against Gust A. Design elements that influenced the the script are discussed followed by a description of the routine. The script is called Ground-Based Elevated Gust Tracker (GEGT). GEGT was tested against gust A and it was successful at identifying the gust and determining its direction.

Many different elements went into designing this routine. It needs to identify candidates in the pressure measured by the array and determine whether or not pressure fluctuations were due to gusts. The time between identifying candidates and classifying them as gusts needs to be as small as possible so that there is enough time to function as an early warning detection system for wind turbines. The code needs to adaptable to a variety of geometries so that exploring several array designs would not require time consuming rewrites.

From the results of the correlation studies in Chapter 3, three gusts were identified. These gusts resulted in clusters of pressure fluctuations on the ground that propagated downstream at speeds that exceeded the wind velocity on the ground. The processing routine will have to be able to calculate the rate at which pressures transfer across the array so that this rate can be compared to the wind velocity on the ground. This includes pressure clusters that move in different directions from the wind altogether. The studies from Chapter 3 also showed that the lowest pressure amplitude associated with an elevated wind gust was on the order of 3 Pa. With this in mind, the processing script should have a threshold that can be set by the user. Pressure fluctuations below this threshold will be ignored. With those elements in mind, a processing script called GEGT was designed that identifies pressures that exceed a set threshold, determines if the pressures are moving downstream, calculates the rate that the pressures move, and compares the pressure transfer rate to the wind velocity on the ground.

GEGT monitors a grid of time series data recorded with pressure sensors placed on the ground. At each time step it finds the maximum pressure and compares it to a threshold that is set by the user. If the pressure maximum exceeds the threshold it is considered to be a gust candidate and the location is recorded. The locations of successive pressure maxima that pass the threshold requirements are compared against the previous pressure maximum locations to determine if the maximum is moving along a consistent path. If it is, the x and y components of the pressure transport velocity (PTV) are calculated and compared to the instantaneous velocities measured at that location. If either PTV component exceeds the corresponding components of the instantaneous velocities the event remains a gust candidate. This process is carried into the third time step after the initial peak was identified and if it passes again the location of the peak at the third time step is recorded along with the initial time step location and a point is placed on a plot that represents the grid. At this point a warning is issued that GEGT has detected a pressure peak that is traveling on a non-random path and is highly likely to be associated with a gust. It also notes the direction that the gust is moving, however, it should be noted that if the coherent pressure fluctuation triggers the edge of the array it may misidentify the direction of extremely short duration events that last for 3 s or fewer. The script for GEGT is shown in appendix A.

GEGT was tested on the LES data. The input was a time series of the pressure that included fluctuation caused by gust A. An array under gust A was simulated by selecting a $10x10$ square of grid points with a horizontal resolution of 2 m. GEGT ran for 200 s of LES data and reported back its gust alerts in real time. GEGT was successful in identifying gust A and determining its direction. The output of GEGT for event A is shown in Fig. 4.1. The numbers next to the gust alerts in the plot indicate the time after the run began that the events was identified as a gust. The simulated array that was used during this test is called Array I. If Array I was replicated in the field with real sensors it would require 100 pressure sensors and it would cover 200 square meters of area. The number of sensors in Array I is too high to be practically used in the field, however, Array I will serve as a starting point in Chapter 5 for optimization.

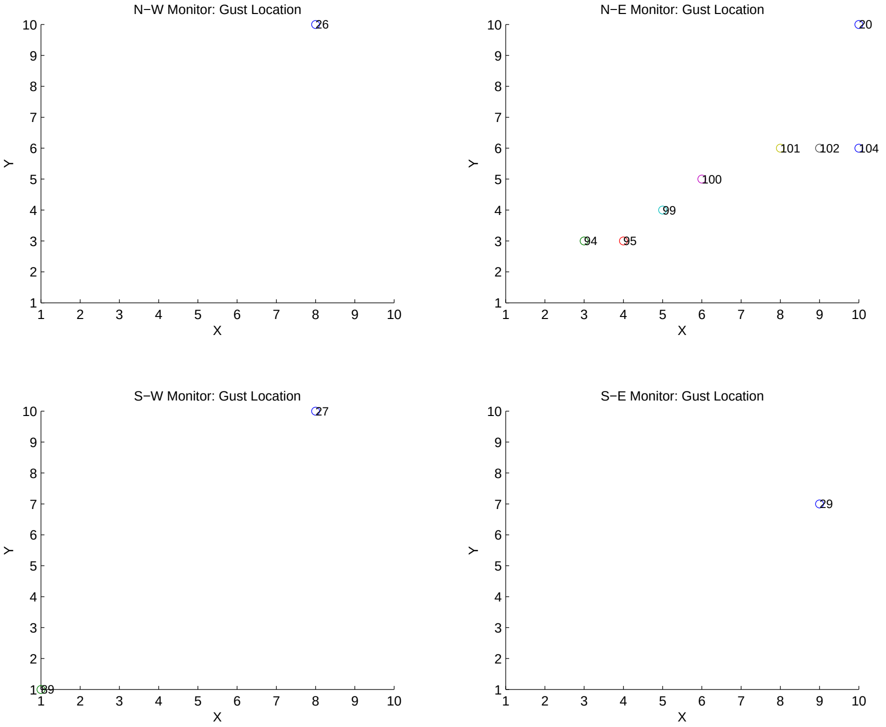

Figure 4.1. GEGT results from the 10 x 10 square of grid points with 2 m spacing between sensors. Gust A was detected by GEGT and is shown in the N-E monitor with the last point at [x,y,t] = (10,6,104) indicating where the pressure disturbance exited the array. This array has too many sensors to be practical but provides a starting point for optimization.

CHAPTER 5: ARRAY DESIGN

Developing an optimized ground based pressure sensing array is one of the goals of this project. This chapter will discuss typical prescriptions for array optimization from the literature, the approach adopted by this project, array parameters based off results from Chapter 3, and the results of applying the approach. In the end, an array design will be selected to be used in Chapter 6.

Typically, arrays are optimized by maximizing a weighted sum of either cross-correlations in the time domain or cross-coincidences in the frequency domain for all pairs of instruments. Methods like these are suited for data that is well separated in time but may not be in frequency. Pressures on the ground induced by elevated gusts are transient signals and therefore these maximum cross-correlation methods are not compatible. Other methods, such as the beamsteering method, sweep a beam of an array through the azimuth of interest until a signal maximum is detected. The time lag between different parts of the array gives the information necessary to determine properties of the signal such as propagation direction and phase speed. However, approaches like the beamsteering method use an array transfer function that is developed using an equation of the cross-power spectral density of a traveling plane wave.[33] A plane wave equation does not describe a gust and a similar equation for the cross-power spectral density for an elevated gust induced surface pressure is not available so this method is also not applicable.

The approaches to array optimization outlined above are similar in that parameters such as the number of sensors and sensor spacing are changed until an optimization is reached. Developing a rigorous array optimization procedure for transient signals, to this author's knowledge, has yet to be done and would involve a significant research project in and of itself. Since there is not a mathematical way to optimize an array for transient signals such as elevated gust induced pressure fluctuations, a different approach is adopted that will also vary the sensor number and spacing but with respect to a known elevated gust induced pressure. The pressure induced by gust A will be used as a basis signal. Gust A was chosen because it does not break into multiple clusters over the array or trigger large secondary events as it propagates. The control parameters in the array are the number of sensors and the sensor spacing. The shape needs to be symmetric so that directional bias is minimized. Due to the limitations set by the data resolution, a square array is chosen as the shape. Also, the minimum resolution in the array that can be explored with the LES data is 2 m and the spacing can only be expanded in even increments. Each array will be rated on two criteria: the number of identifications GEGT makes on the array during gust A and the number of identifications GEGT makes prior to the center of the array during gust A. Since the direction of A is fairly consistent, any array configurations that fail to provide the data required by GEGT to calculate direction will be rejected.

This array needs to be sensitive to the elevated gust induced surface pressure characteristics revealed in Chapter 3. These characteristics are pressure transfer rates and pressure cluster size. The pressures transfer rates were found to be between 4 - 5.3 m/s. The mean flow on the ground was approximately 3 m/s and because of the small sample size the range of speeds considered here will be 3 - 6 m/s. The sizes of the pressure clusters ranged from 10 - 40 m and so the array needs to be large enough to be able to measure these structures. A minimum of 2 detections prior to the gust reaching the center of the array are needed so that the array can be used to protect structures such as wind turbines. The starting geometry will be a 4×4 sensor array and sensor spacing of 2, 4, 6, and 8 m will be explored. Once an array fails to produce an identification, the current and following sensor spacings will be rejected. In the end, a balance between the number of identifications made, the number of identifications made prior to the center, and the number of sensors used will be chosen.

Ideally, the number of sensors should be as low as possible to minimize cost while the area of coverage should be maximized to increase the area that is being monitored for gusts.

A 200 s time series of a horizontal slice of the surface pressure containing gust A was used. The threshold for GEGT was set to 4 Pa. Each new array configuration was adjusted so that it would be directly in the path of gust A so that location bias would be minimized. Table 5.1 summarizes the results of each array configuration. The minimum number of identifications prior to gust A reaching the center of the turbine is two. The array configuration with the minimum number of sensors that has two identifications is the 6 × 6 array. The 2 m sensor spacing provided the least amount of coverage area but it had the highest number of identifications whereas the 5 m sensor spacing provided the most coverage area but with the lowest number of identifications. The 8 m sensor spacing failed to provide two identifications prior to gust A reaching the center. The array that is chosen to conduct blind searches is the 6 × 6 sensor array with 4 m spacing between the sensors because it provided a balance between the number of identifications and coverage area.

For the most part a pattern is evident if one studies the table closely. As the sensor spacing increases the number of total identifications, and thus the number of identifications prior to center contact, decreases. This happens because the sensor spacing has increased but the group velocity of the pressure fluctuation induced by gust A remains the same. Consider a linear array in the path of a gust induced pressure which moves along the array at 4 m/s. If the pressure maximum registers on sensor one at 1 s and there is 2 m spacing between the sensors, at 0.5 s later the pressure maximum will have reached sensor two and traveled 2 m. With 8 m spacing the pressure maximum will reach sensor number two in 2 s. The linear array with 2 meter spacing would have 4 identifications in 2 s whereas the the linear array with 8 m spacing would only have 2. GEGT can be set to report 2 s after identification, however, this would increase the number of false alarms caused by randomness. By default GEGT is set to report 3 s after identification and so the latter linear array would not be identified as a gust until 4 seconds later when it collects 3 identifications. The number of identifications decreases as the number of sensors decreases as well. This happens because the area of coverage is shrinking and so there is less space for the gust induced pressure signal to move through and be identified by GEGT.

In summary, an array was optimized for use with GEGT by varying the number of sensors and sensor spacing in a square array. Twenty-eight configurations were analyzed but the 6 × 6 sensor array with 4 m spacing was chosen as the optimized array and will be used in the following chapter to conduct blind searches. This array has 400 m^2 of coverage area and uses 36 sensors. The 6 × 6 sensor array with 6 m spacing could also be used with a slight loss to the number of identifications but with a coverage area of 900 m^2.

Table 5.1. Summary of array optimization. Entries in a/b format where a is the total number of identifications during gust A and b is the number of identifications prior to the center of the array during gust A. Rejections due to failing to determine direction or making identifications will be marked with an X.

$SensorSpacing:$	$2m$	$4m$	$6m$	$8m$
4 × 4	3/1	3/1	X	X
5 × 5	4/1	4/1	3/1	2/0
6 × 6	5/2	4/2	3/2	3/1
7 × 7	6/2	4/2	4/2	4/1
8 × 8	7/4	5/2	5/2	4/1
9 × 9	8/4	8/3	5/2	4/1
10 × 10	6/3	8/3	6/2	4/2

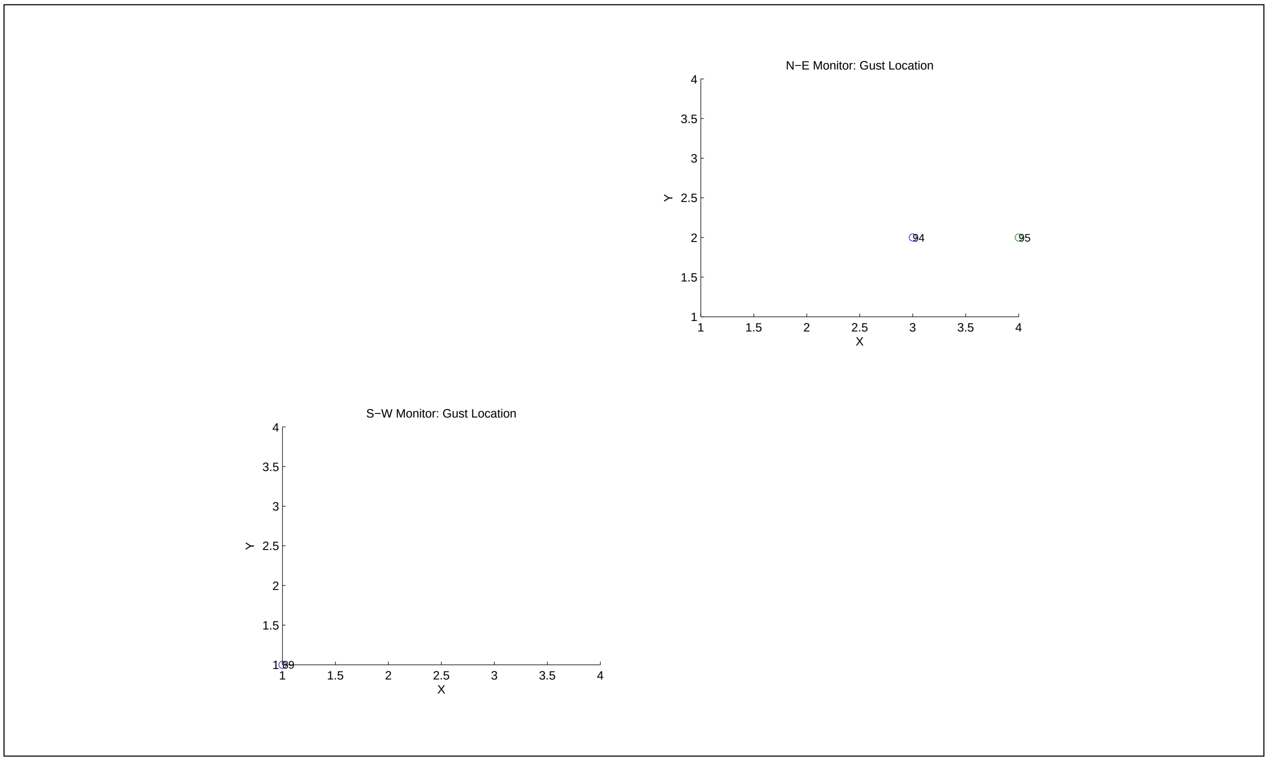

Figure 5.1. GEGT output for 4×4 sensor array with 2 m sensor spacing.

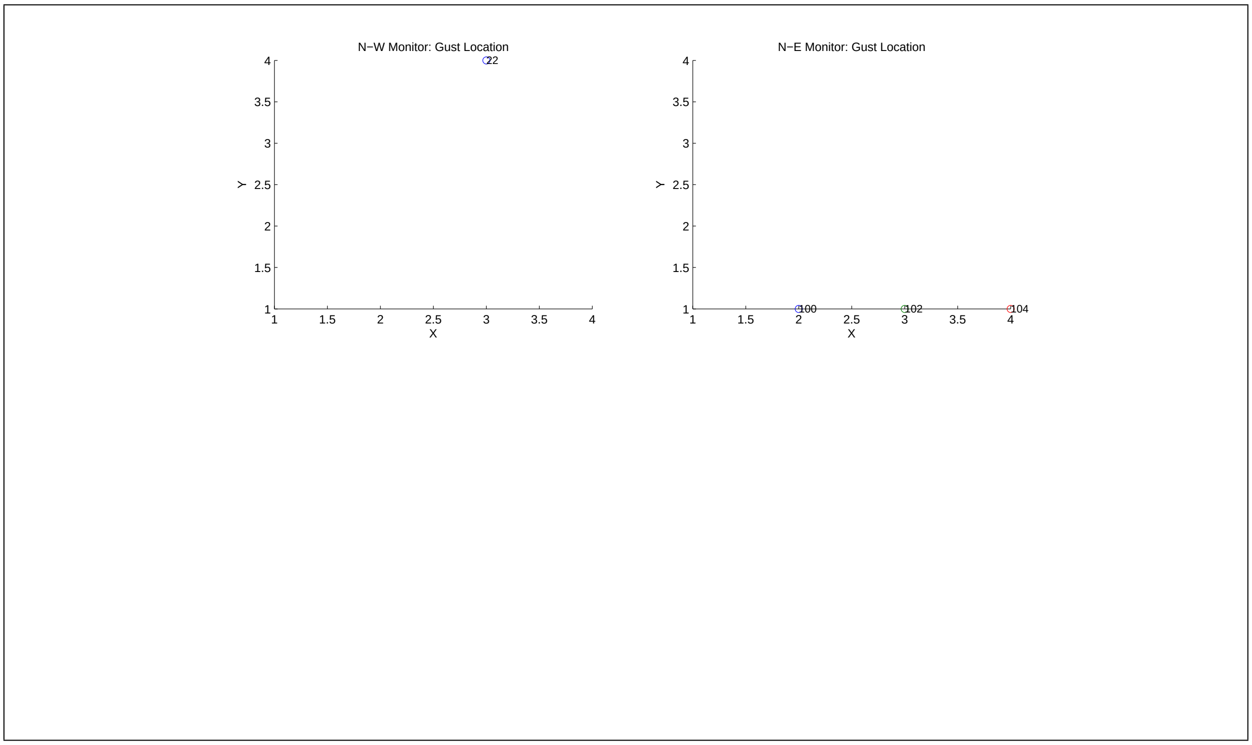

Figure 5.2. GEGT output for 4×4 sensor array with 4 m sensor spacing.

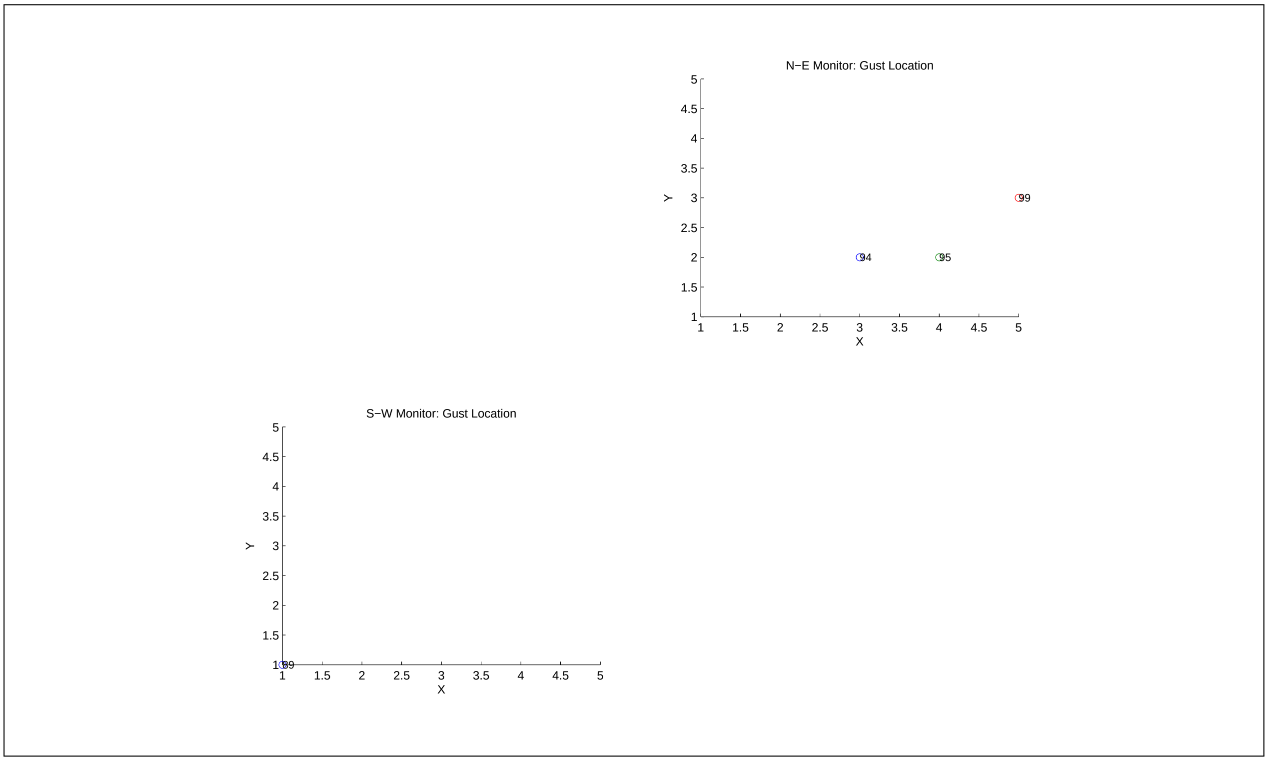

Figure 5.3. GEGT output for 5×5 sensor array with 2 m sensor spacing.

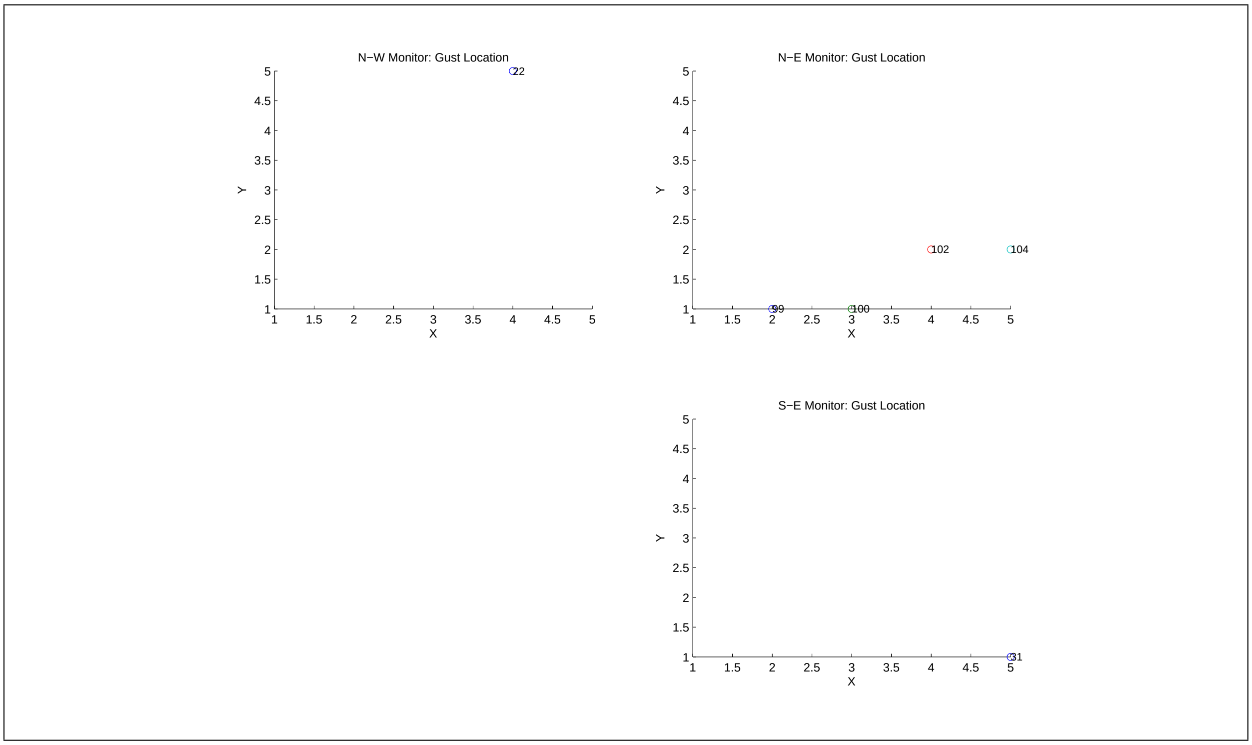

Figure 5.4. GEGT output for 5×5 sensor array with 4 m sensor spacing.

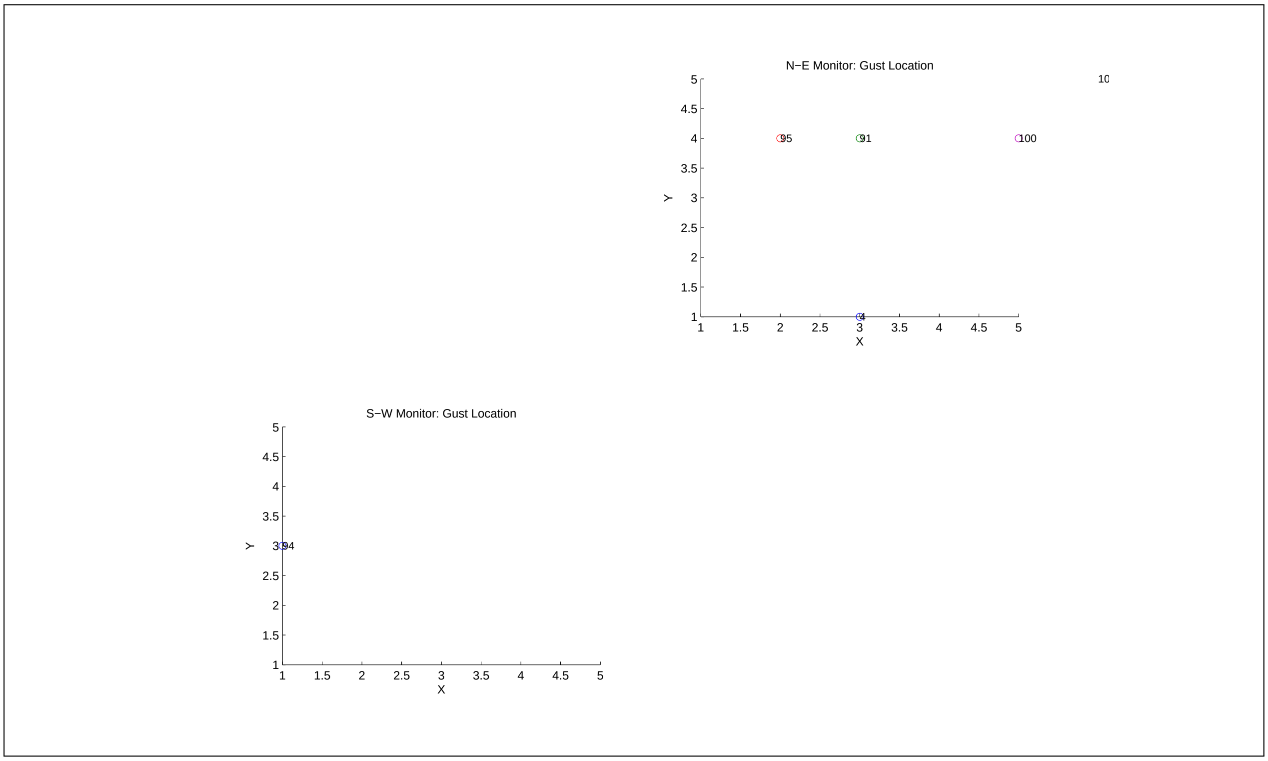

Figure 5.5. GEGT output for 5×5 sensor array with 6 m sensor spacing.

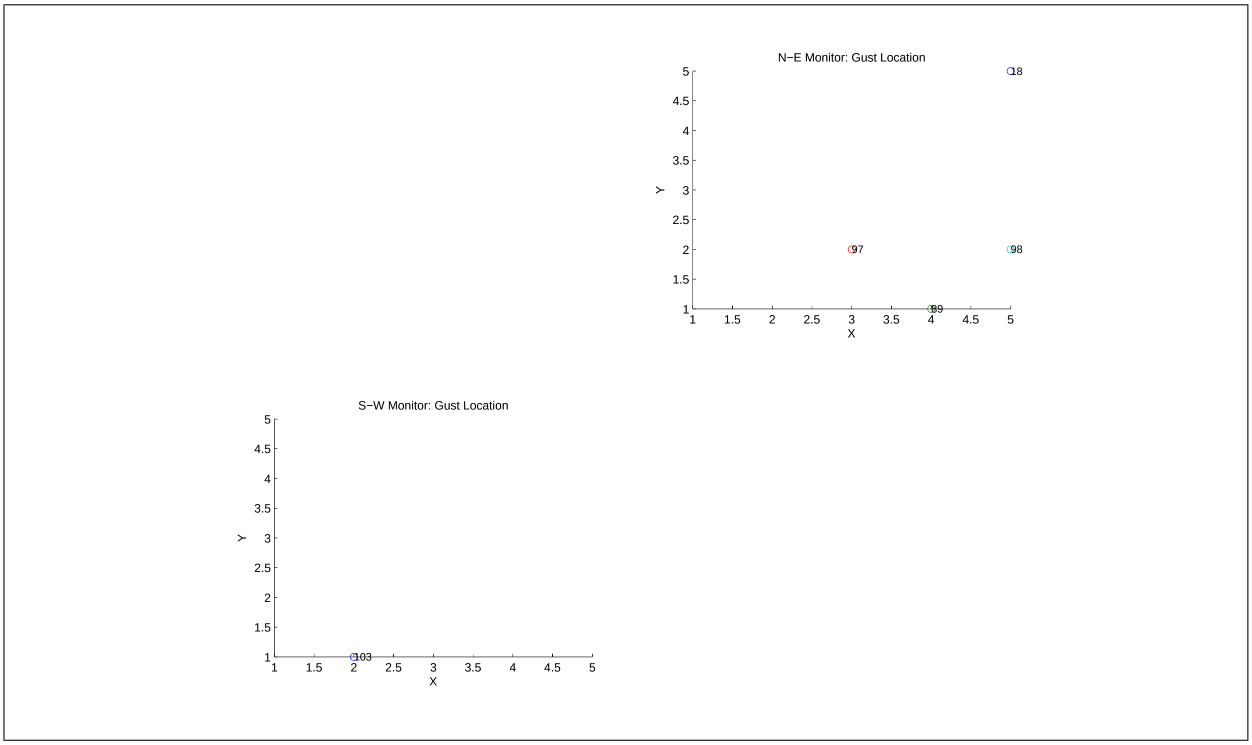

Figure 5.6. GEGT output for 5×5 sensor array with 8 m sensor spacing.

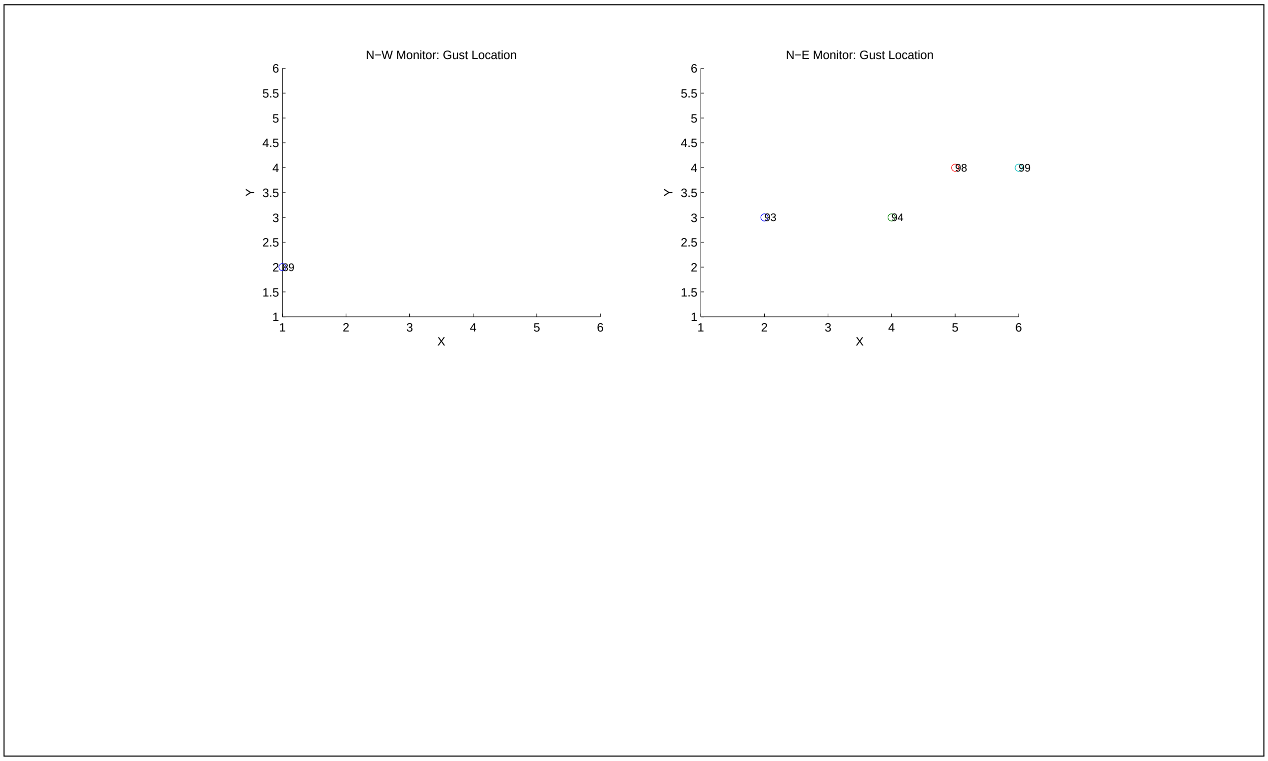

Figure 5.7. GEGT output for 6×6 sensor array with 2 m sensor spacing.

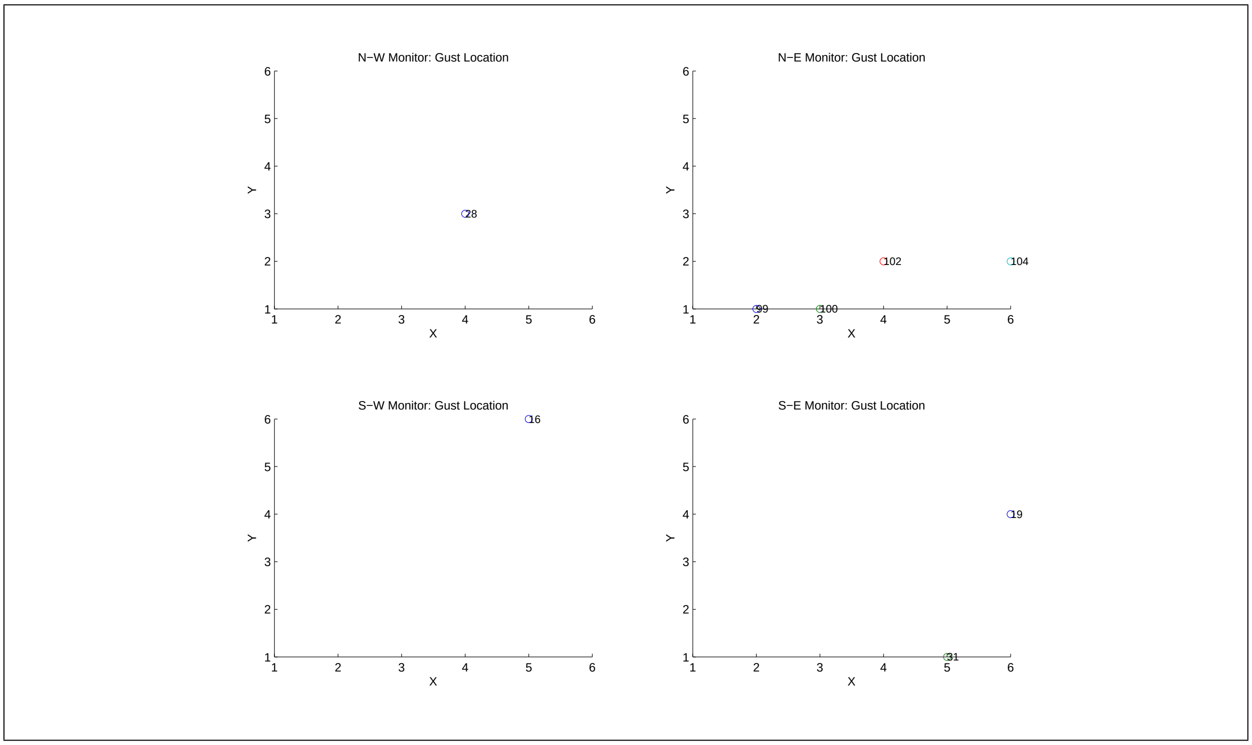

Figure 5.8. GEGT output for 6×6 sensor array with 4 m sensor spacing.

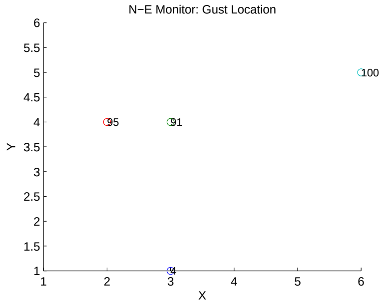

Figure 5.9. GEGT output for 6×6 sensor array with 6 m sensor spacing.

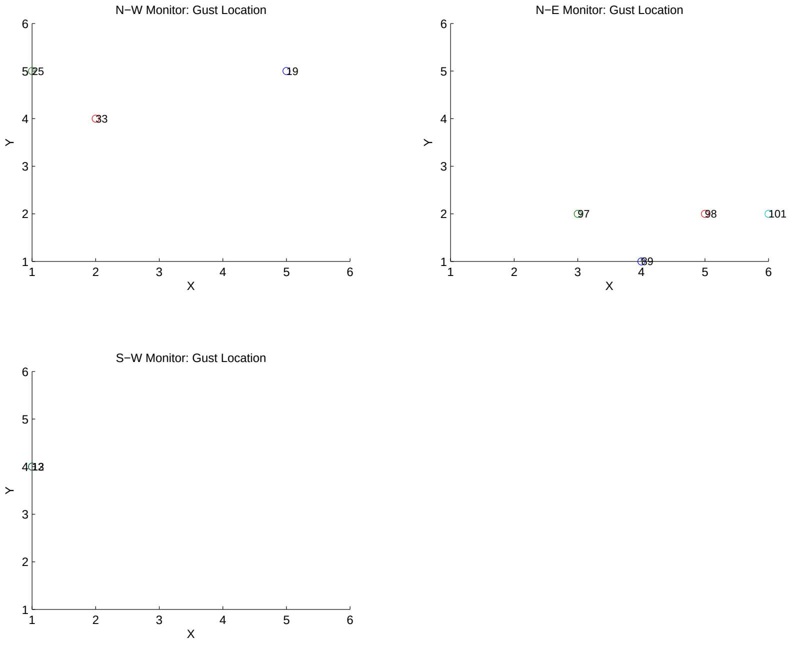

Figure 5.10. GEGT output for 6×6 sensor array with 8 m sensor spacing.

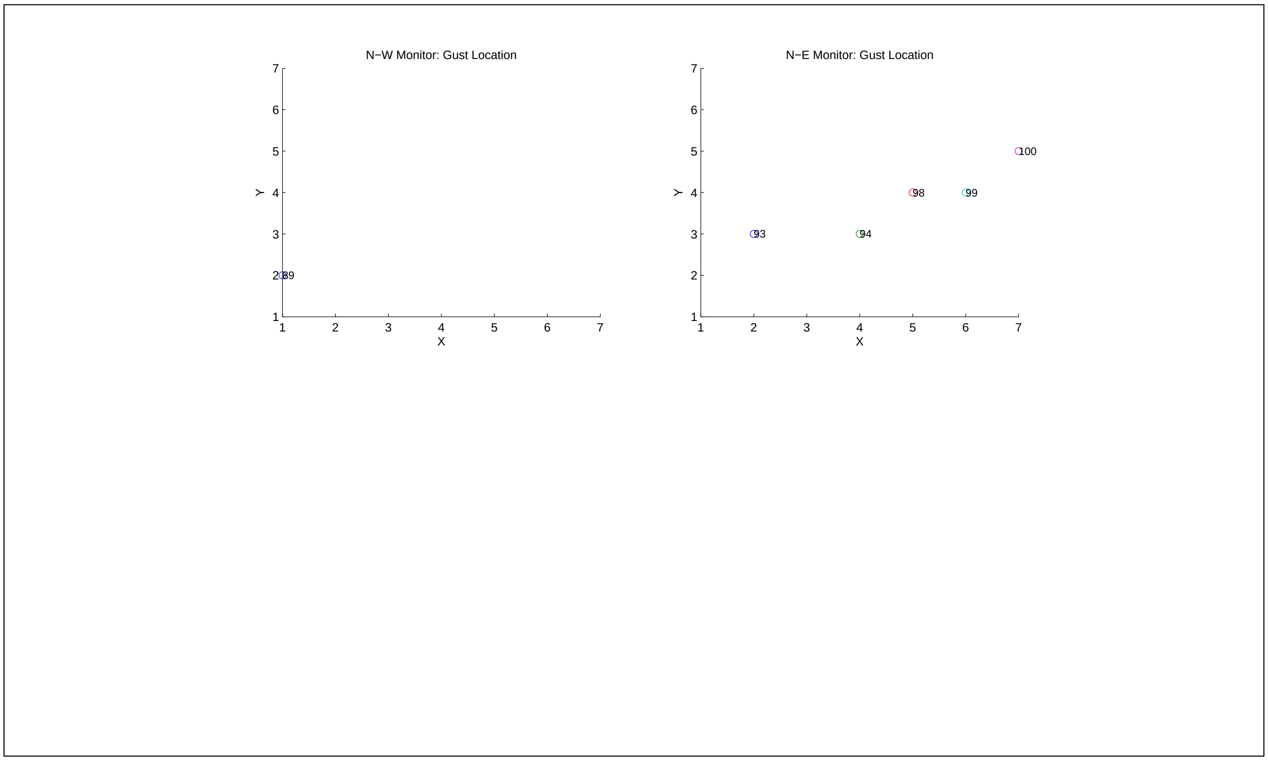

Figure 5.11. GEGT output for 7×7 sensor array with 2 m sensor spacing.

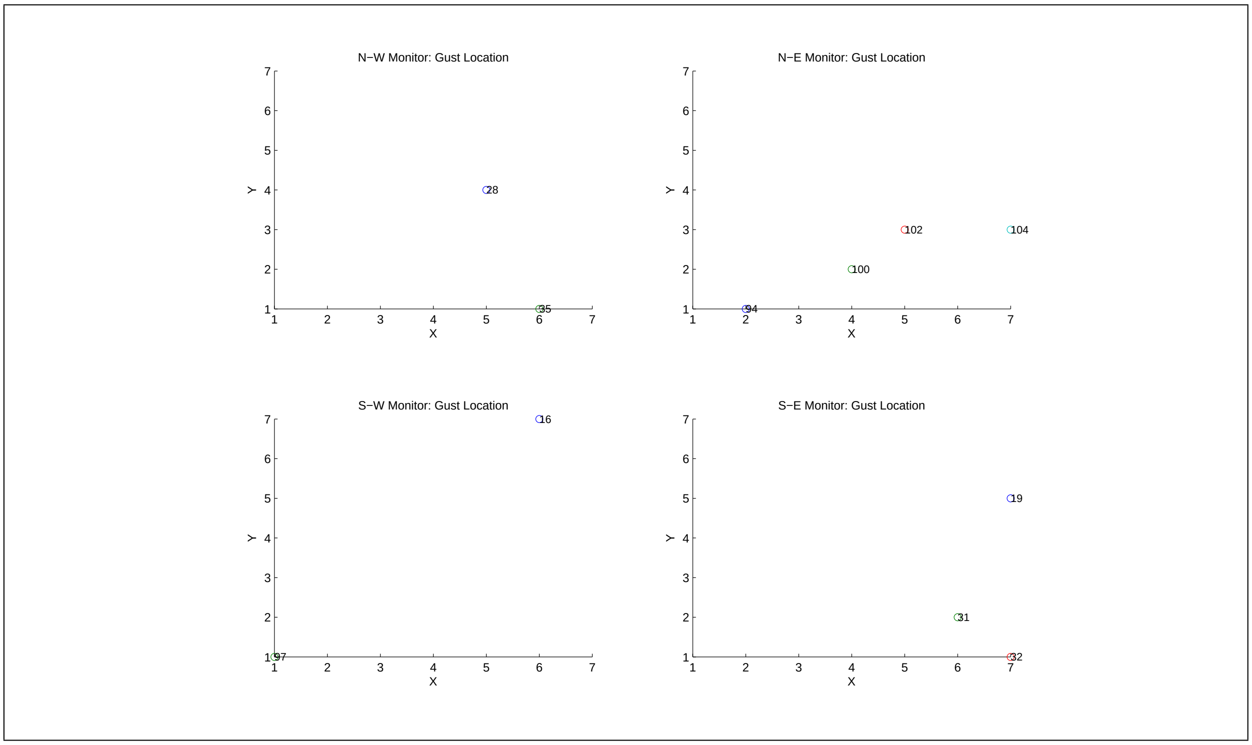

Figure 5.12. GEGT output for 7×7 sensor array with 4 m sensor spacing.

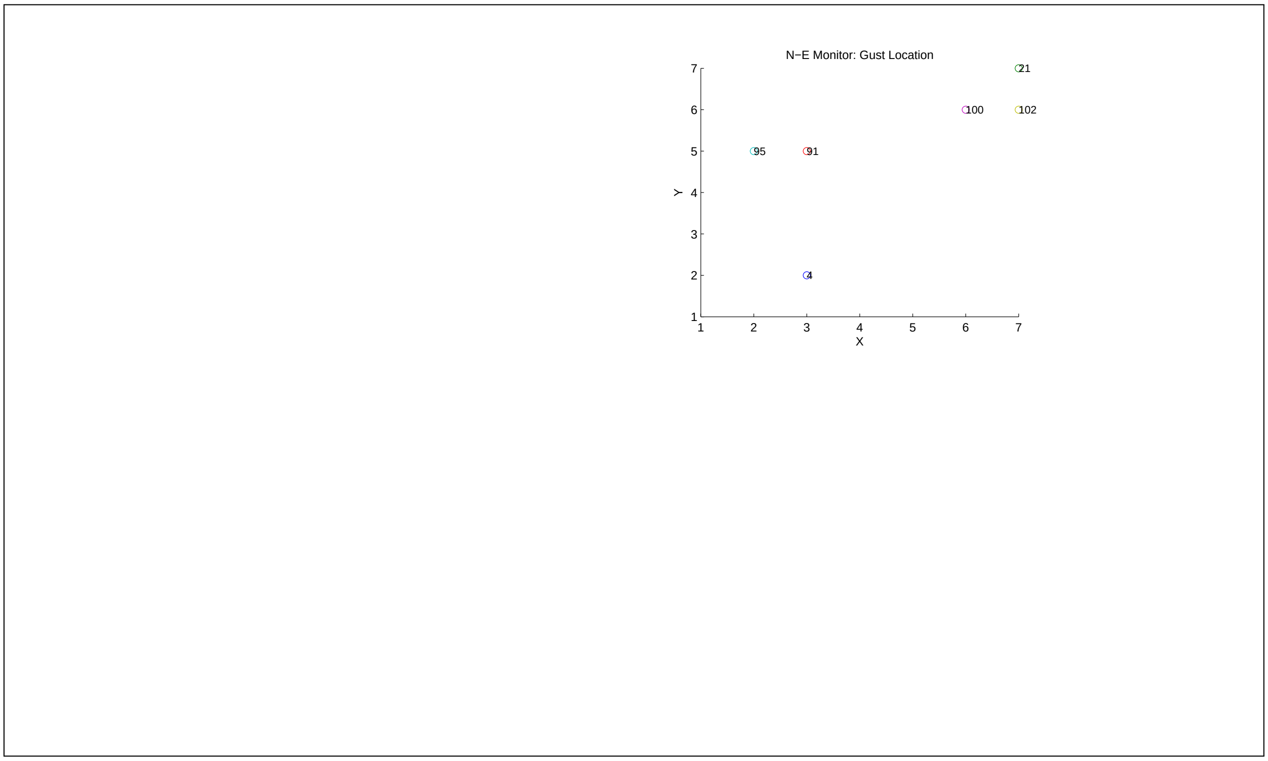

Figure 5.13. GEGT output for 7×7 sensor array with 6 m sensor spacing.

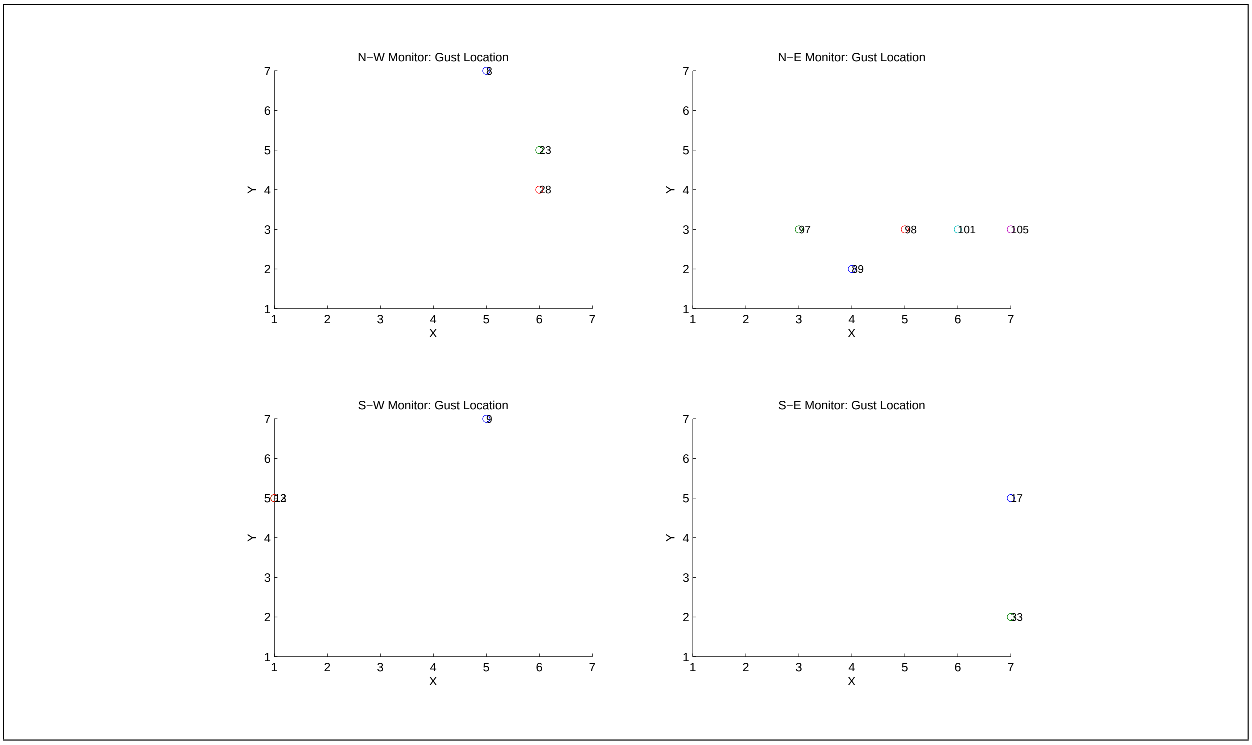

Figure 5.14. GEGT output for 7×7 sensor array with 8 m sensor spacing.

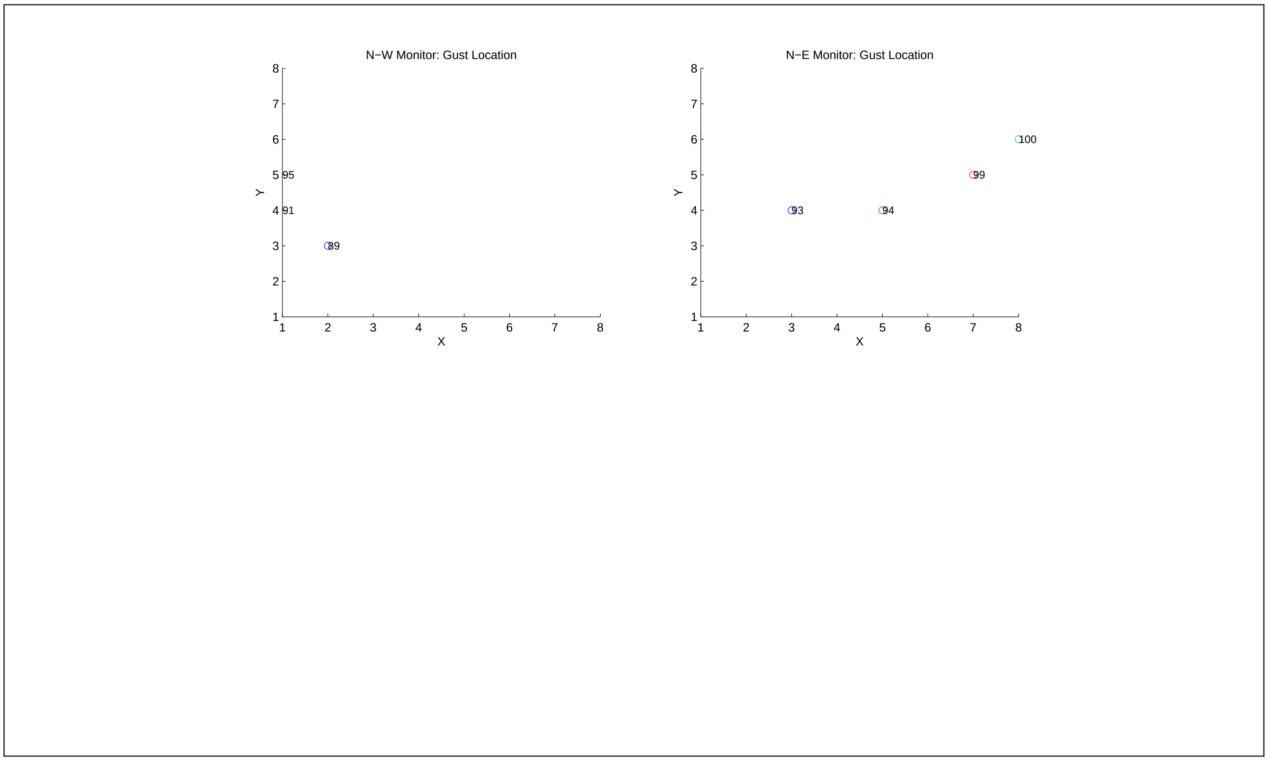

Figure 5.15. GEGT output for 8×8 sensor array with 2 m sensor spacing.

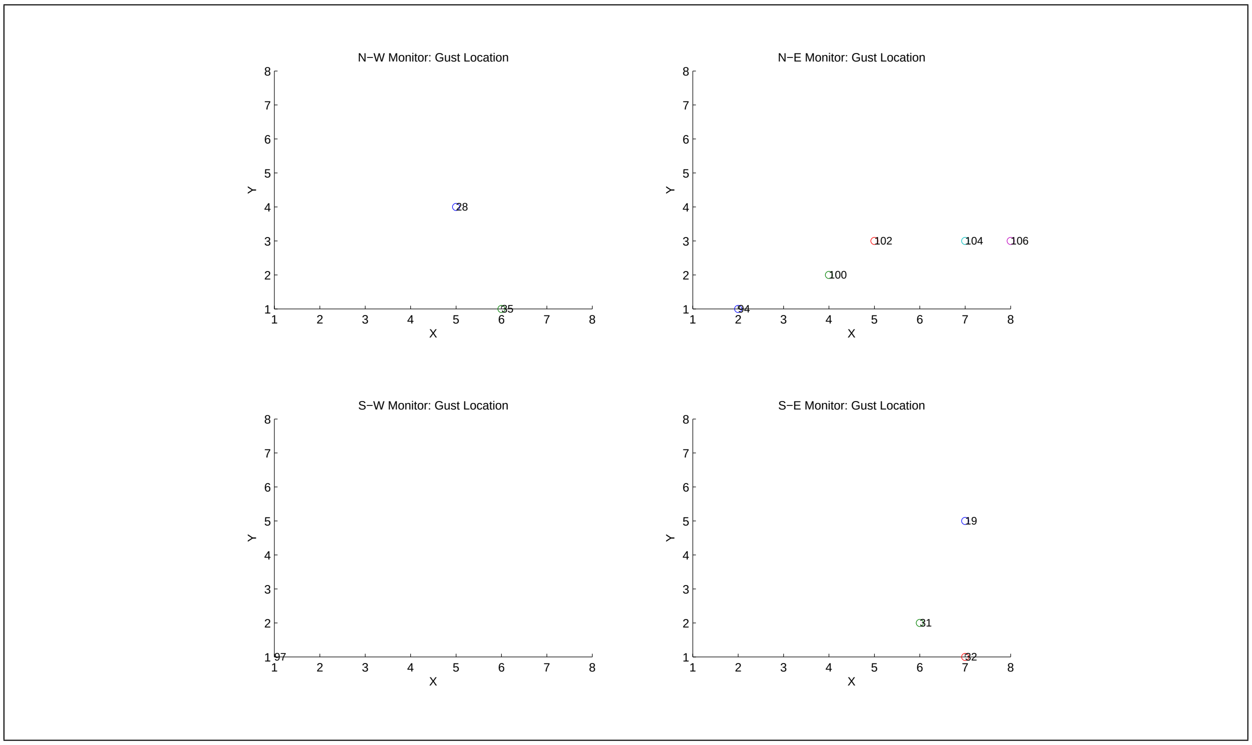

Figure 5.16. GEGT output for 8×8 sensor array with 4 m sensor spacing.

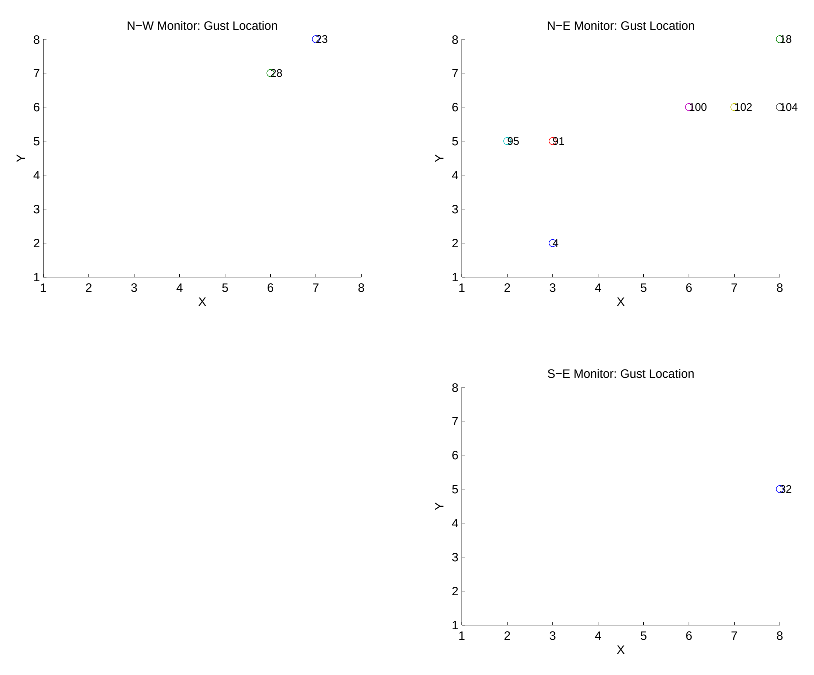

Figure 5.17. GEGT output for 8×8 sensor array with 6 m sensor spacing.

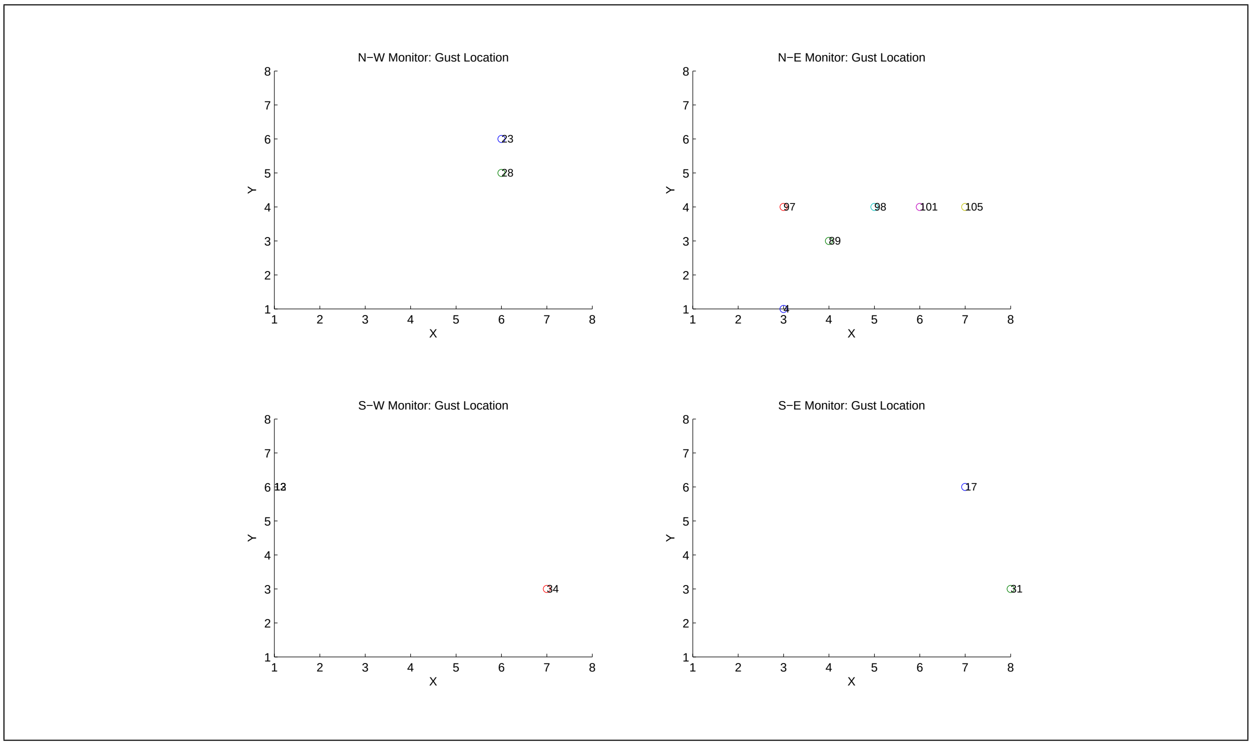

Figure 5.18. GEGT output for 8×8 sensor array with 8 m sensor spacing.

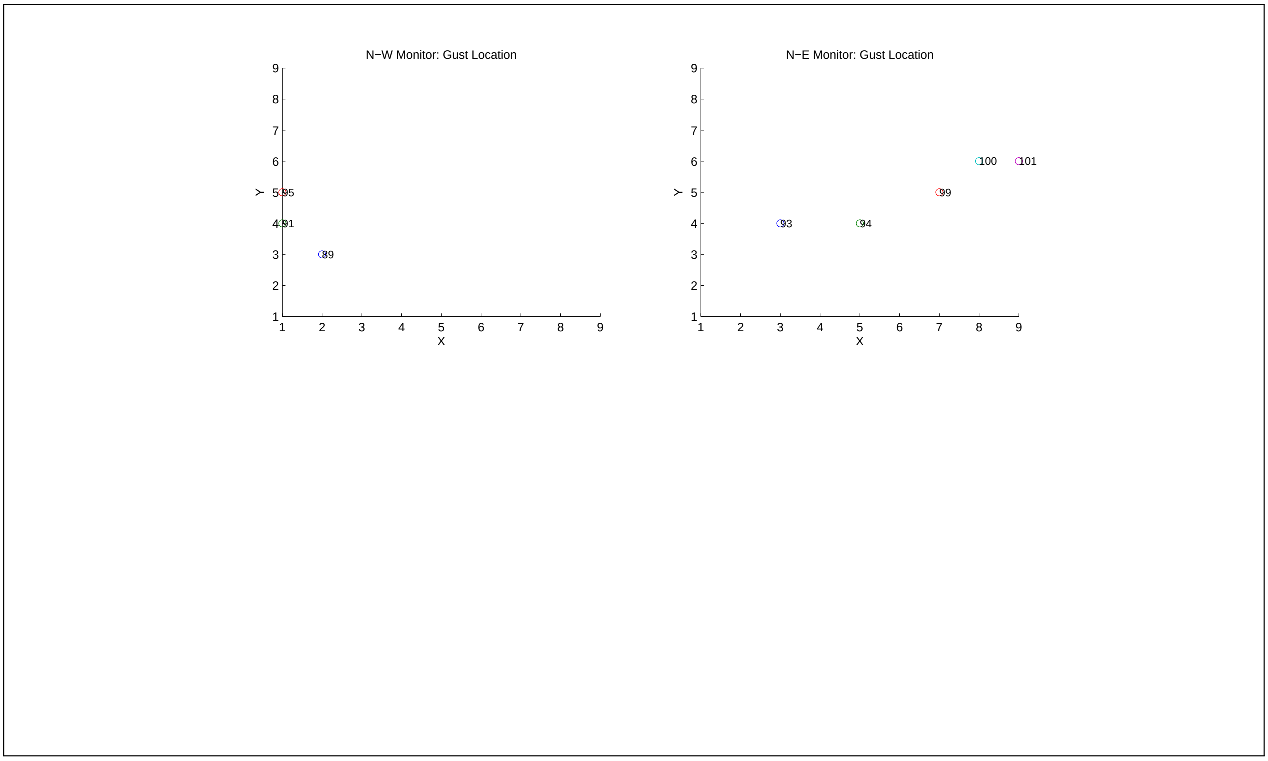

Figure 5.19. GEGT output for 9×9 sensor array with 2 m sensor spacing.

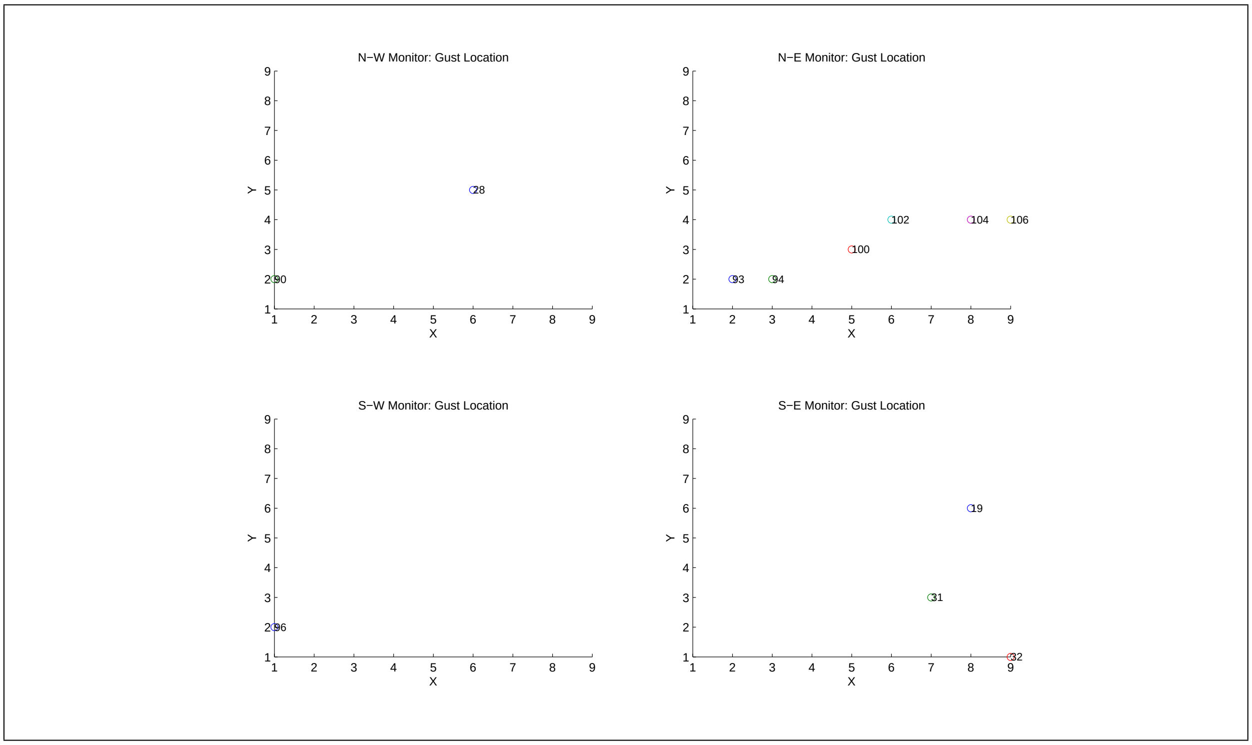

Figure 5.20. GEGT output for 9×9 sensor array with 4 m sensor spacing.

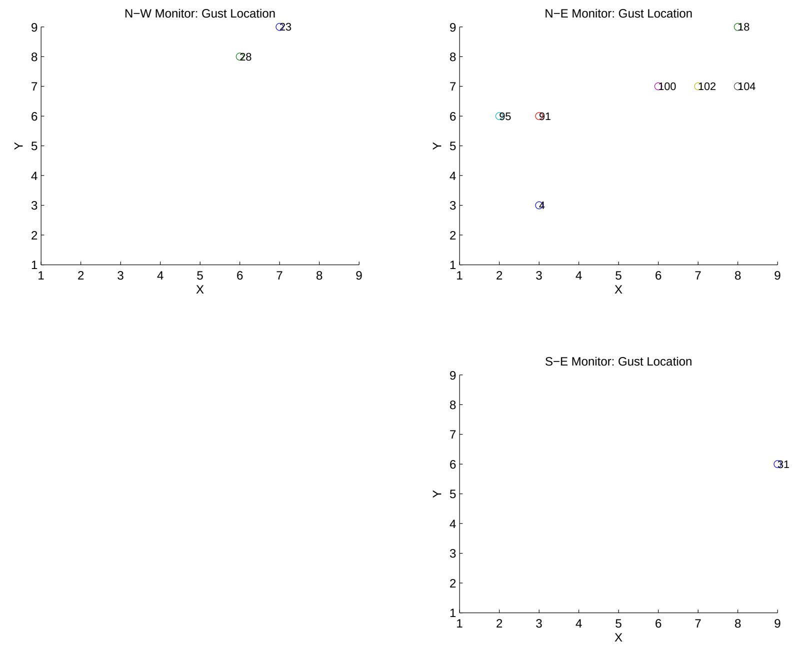

Figure 5.21. GEGT output for 9×9 sensor array with 6 m sensor spacing.

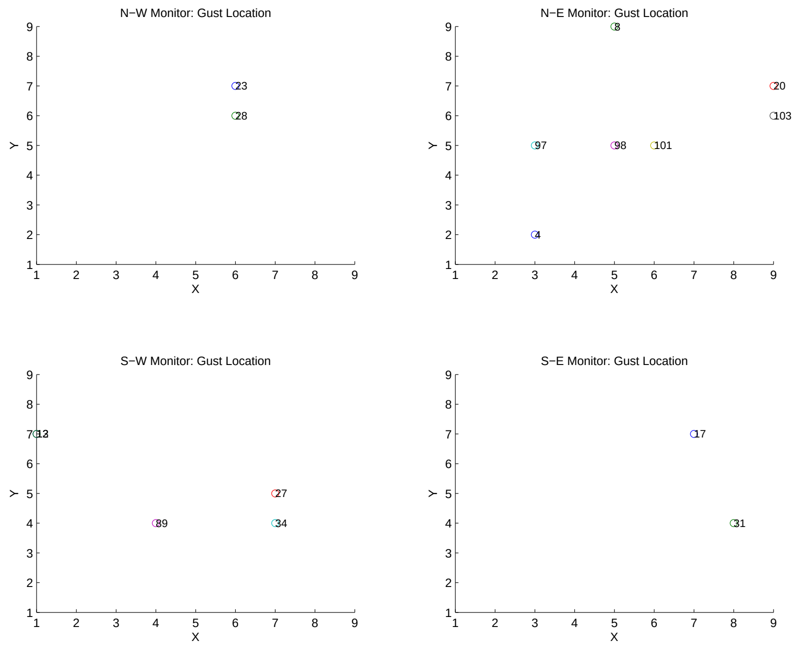

Figure 5.22. GEGT output for 9×9 sensor array with 8 m sensor spacing.

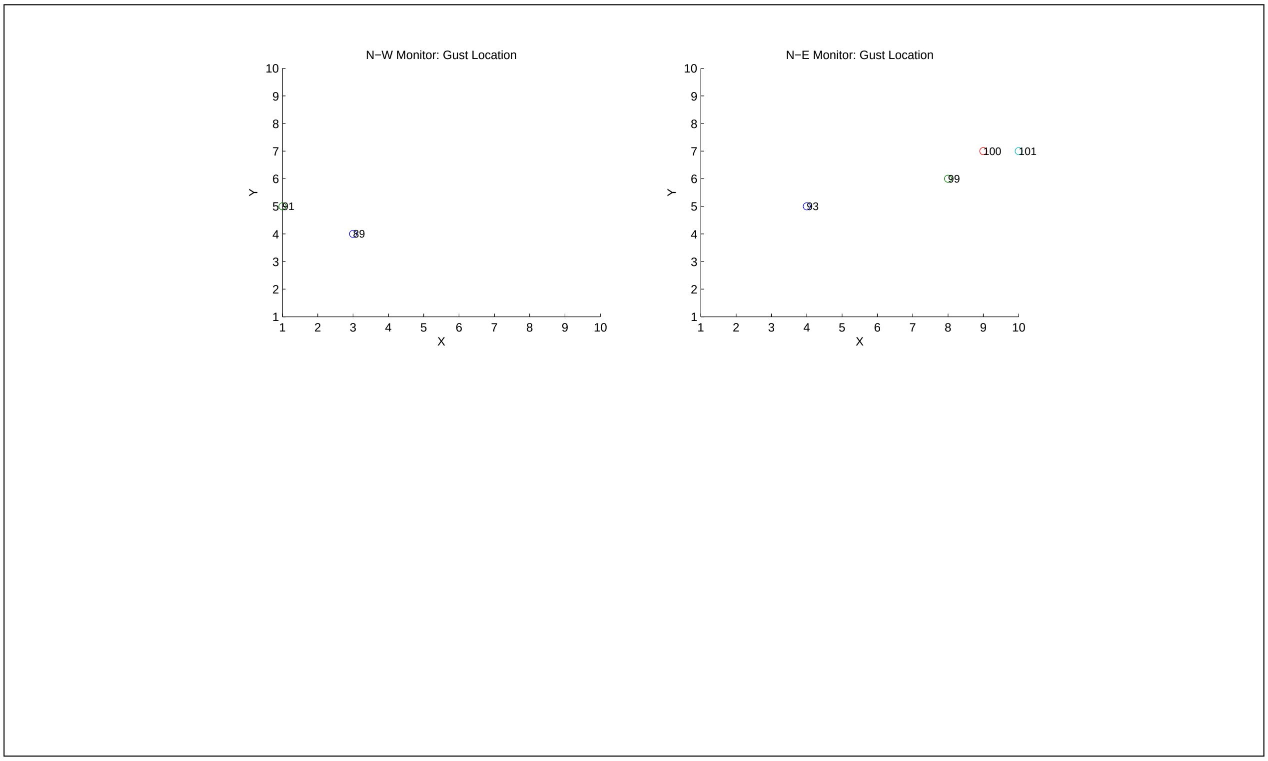

Figure 5.23. GEGT output for 10×10 sensor array with 2 m sensor spacing.

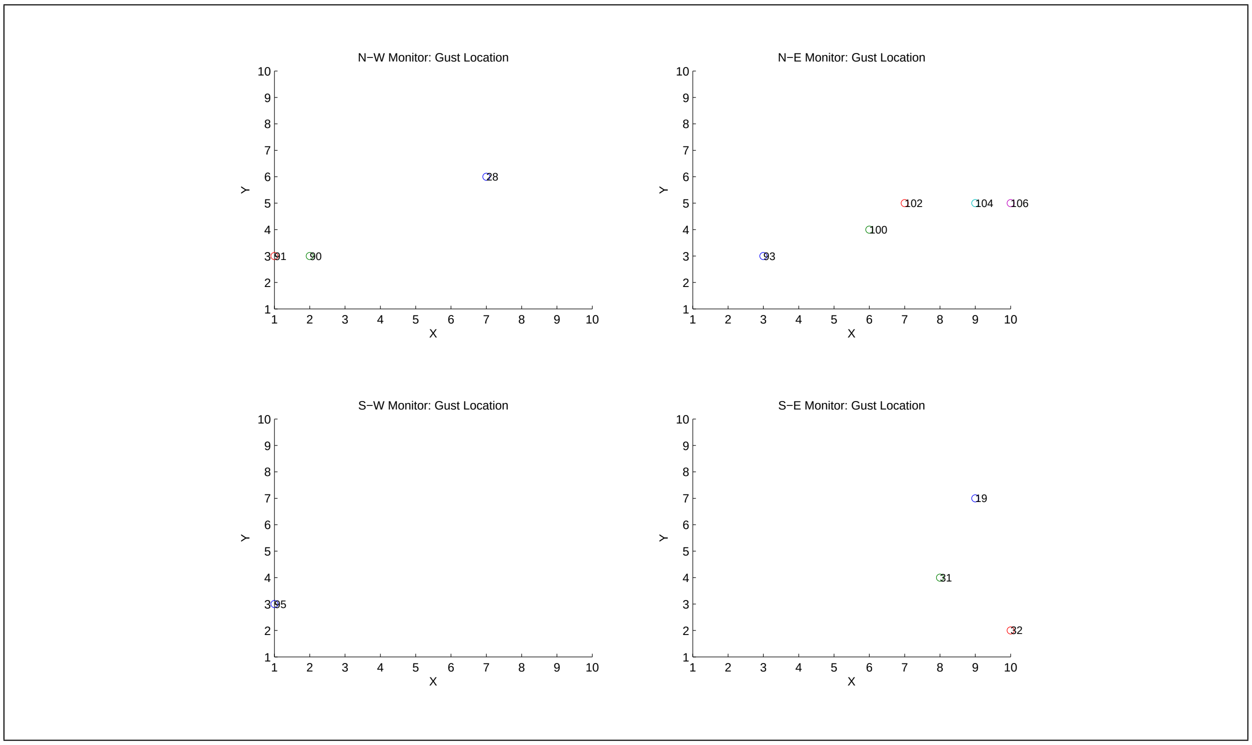

Figure 5.24. GEGT output for 10×10 sensor array with 4 m sensor spacing.

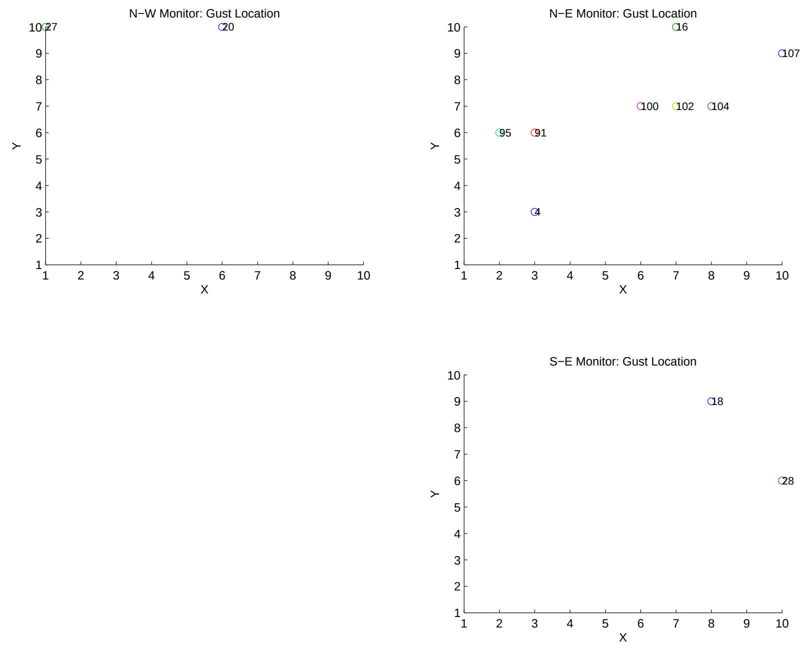

Figure 5.25. GEGT output for 10×10 sensor array with 6 m sensor spacing.

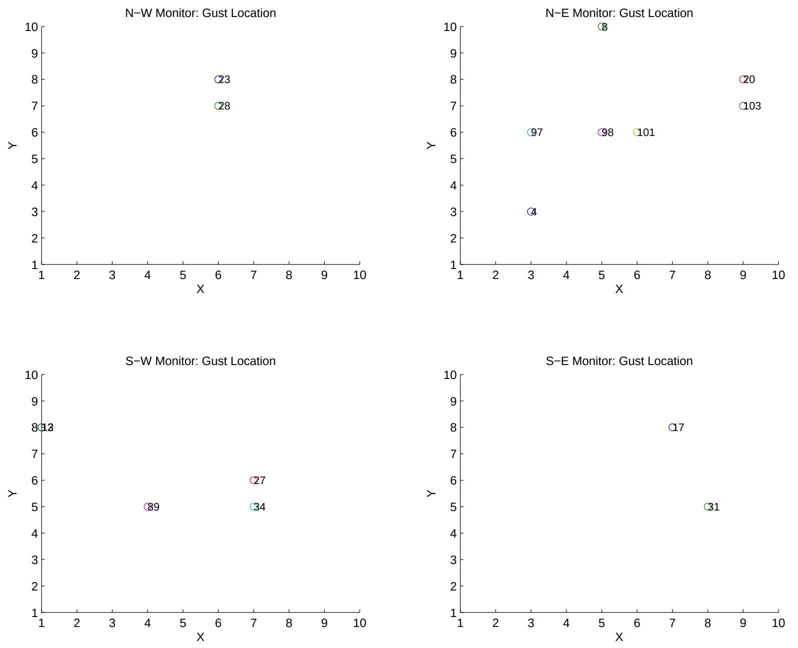

Figure 5.26. GEGT output for 10×10 sensor array with 8 m sensor spacing.

CHAPTER 6: TESTS OF GROUND-BASED ELEVATED GUST TRACKER

6.1 Chapter Overview

In order to increase the confidence that GEGT and the array design are capable of detecting gusts from pressures on the ground several blind searches were conducted. A blind search for this project means that the simulated array is placed in an unexplored location within the LES data while GEGT interprets the time series at each time step to make gust identifications. In order to increase the amount of data available to test GEGT with, a separate LES run was performed with the same conditions. This LES is called Science Run II (SRII). It calculated the velocities and pressures for a daytime convective boundary layer. The simulation reached equilibrium near 3000 s as the altitude versus the heat flux became nearly linear under the capping inversion as shown in Fig. 6.1. The time steps were decreased at 4000 s to output a data file every second for 1000 s. The data was analyzed at model times between 4000 and 5000 s.

Locations on the surface were chosen to be at least 200 m from the numerical boundaries. Other than that, the locations were chosen at random. The 6 × 6 sensor array with 4 m sensor spacing (Array II) from Chapter 5 was the chosen design for these blind searches. After choosing a location, the array recorded data for 1000 s while GEGT processed the data at each time step and reported identifications as they were happening. Once a gust induced pressure was identified, horizontal slices of time series pressure data were plotted. If a moving cluster of elevated pressures was present in the plots, maximum velocities in the wind field above were searched for. When a maximum velocity was found, horizontal plots of the velocity were made at the altitude where the maximum occurred to check for visual similarity between the cluster of velocities aloft and the pressure cluster on the ground below.

The similarities that were considered were location, time, group velocity, and propagation path. Lastly, the new event's velocity from the altitude that contained the maximum was analyzed to determine if it fit the criteria for gust identification from Chapter 1 by plotting the fluctuating part of the velocity against time.

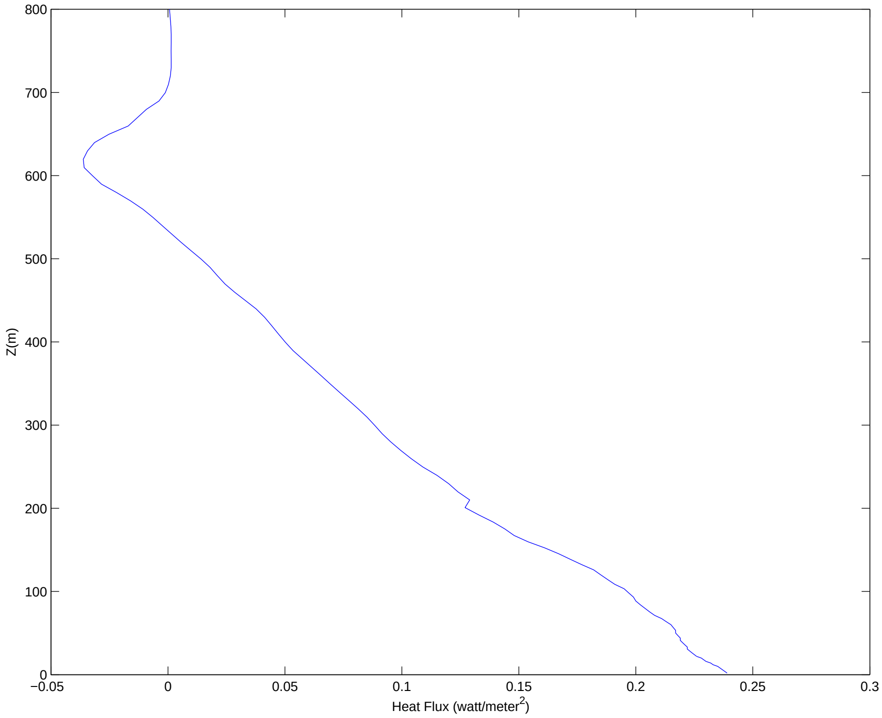

Figure 6.1. Science Run II: Altitude vs. Heat Flux (wt). From the plot the capping inversion is approximately 610 m. The near linear behavior beneath the capping inversion suggests that the simulation has reached equilibrium.

6.2 Blind Search A

Array II was placed between $(x, y) = (560m : 580m, 480m : 500m)$ at the surface level within the simulated atmosphere in SRII. It monitored 1000 s of data and reported back several gust events as shown in Fig. 6.2 beginning around t = 478 s. The pressure data during this period of time was converted to a contour plot and it is shown in Fig. 6.3. In order to capture the entire two dimensional structure of the event the area shown in Fig. 6.3 was increased as shown in Fig. 6.4 and shown for several time slices. This event peaks in pressure magnitude at 61 Pa and just as GEGT identified it moves in the northeast direction with an average speed of 2.7 m/s.

A plot showing z versus x of the velocity at a constant y during this event is shown in Fig. 6.5 at time slices corresponding to those shown in Fig. 6.4. In this figure, a very large velocity disturbance that occupies several altitudes can be seen moving in the x-direction. The maximum velocity above the pressure event occurs at z = 20 m. An x-y slice of velocity at z = 20 meters directly above the pressure event is shown in Fig. 6.6. The pressure on the ground shown in Fig. 6.4 and the velocity at z = 20 m shown in Fig. 6.6 move along the same trajectory.

Fig. 6.7 shows time series for the point where the maximum velocity occurs above the pressure event at z = 20 m. The maximum peak is centered with time and is at t = 0 s. The maximum at t = 0 has a duration of 10 s. That central maximum differs from the nearest minimum by 4.1 m/s. This peak appears to develop off of a squall at higher altitude. The gust factor for this event is 2.

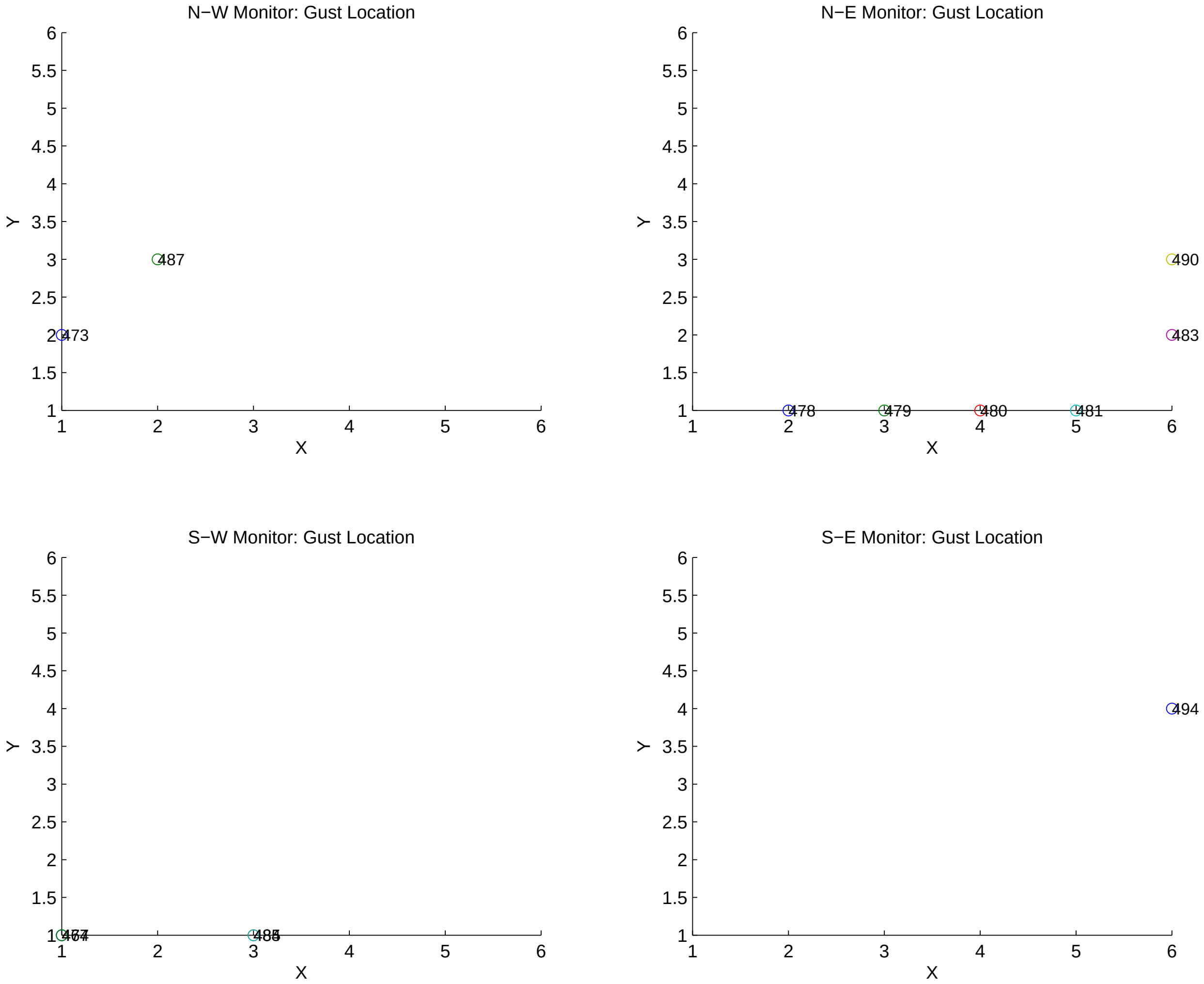

Figure 6.2. BSA: GEGT detected a new gust candidate labeled BSA.

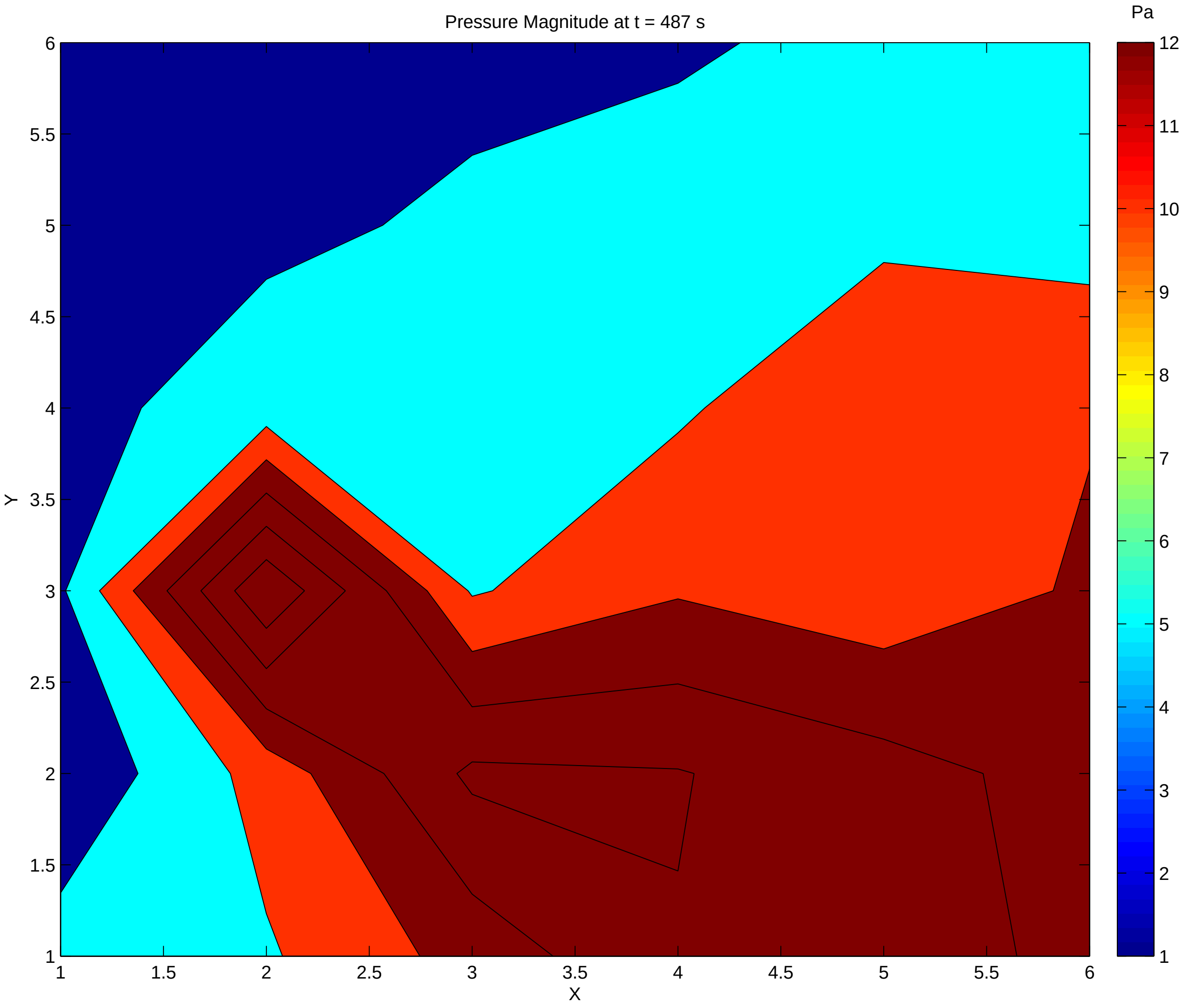

Figure 6.3. BSA: Contour plot of the pressure magnitude with an x-y footprint that is the same size as the array used in Fig. 6.2.

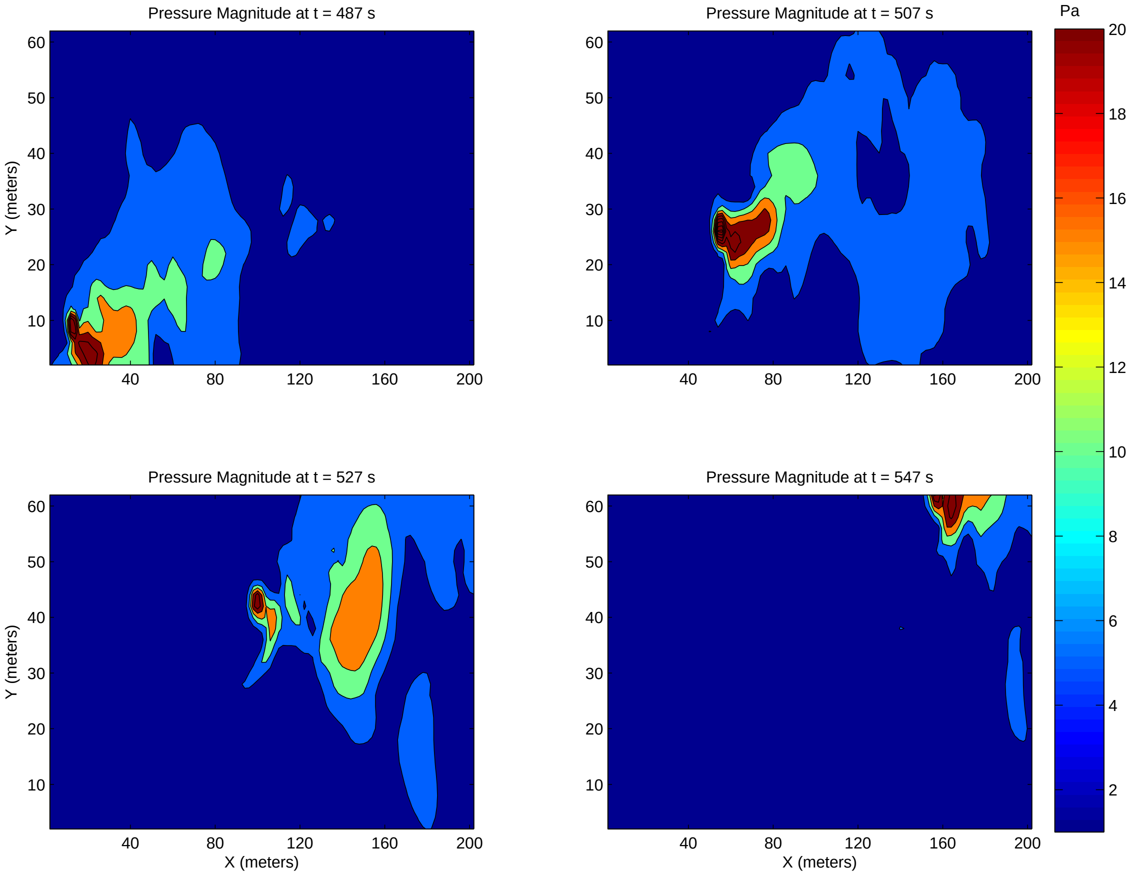

Figure 6.4. BSA: Zooming out from Fig. 6.3 to see the large pressure structure of candidate BSA at several slices in time.

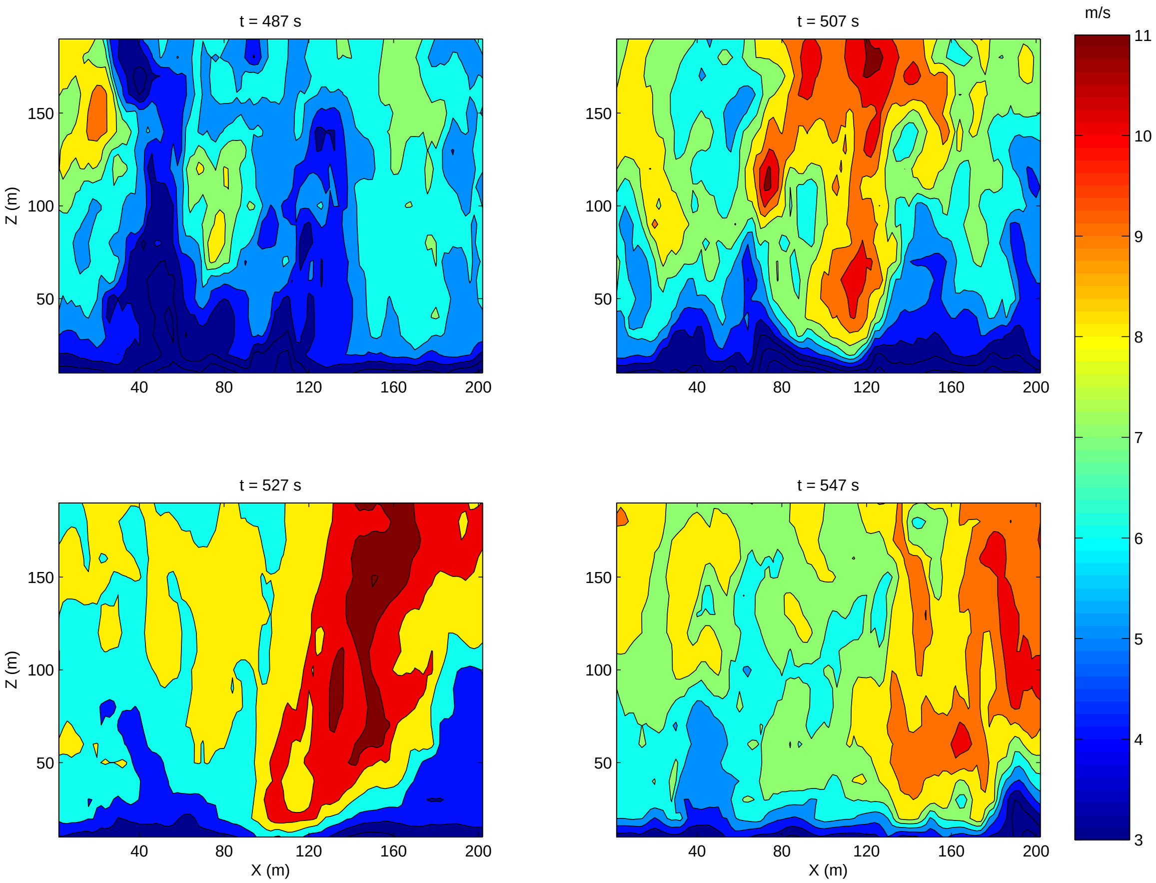

Figure 6.5. BSA: Velocity vs. altitude of candidate BSA as it moves through y = 30 m.

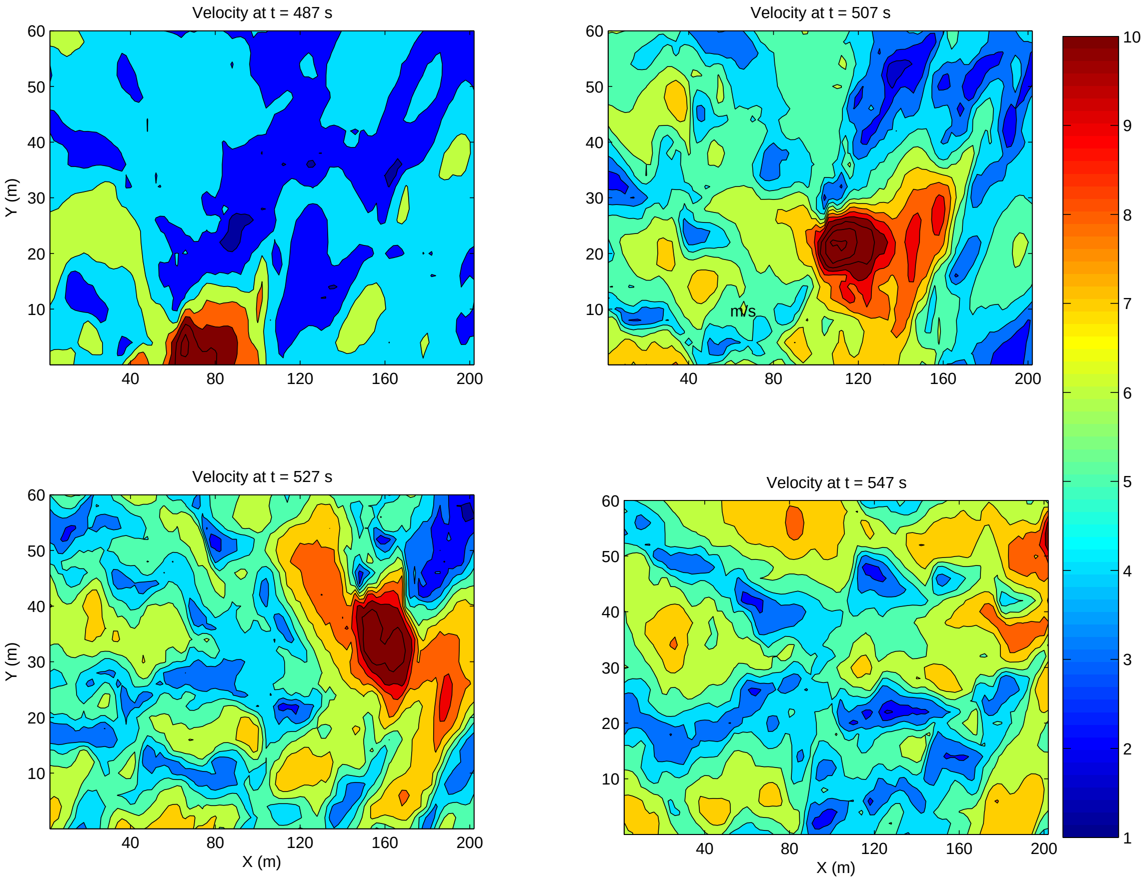

Figure 6.6. BSA: Horizontal slice of velocities at z = 20 m at times corresponding to Fig. 6.4.

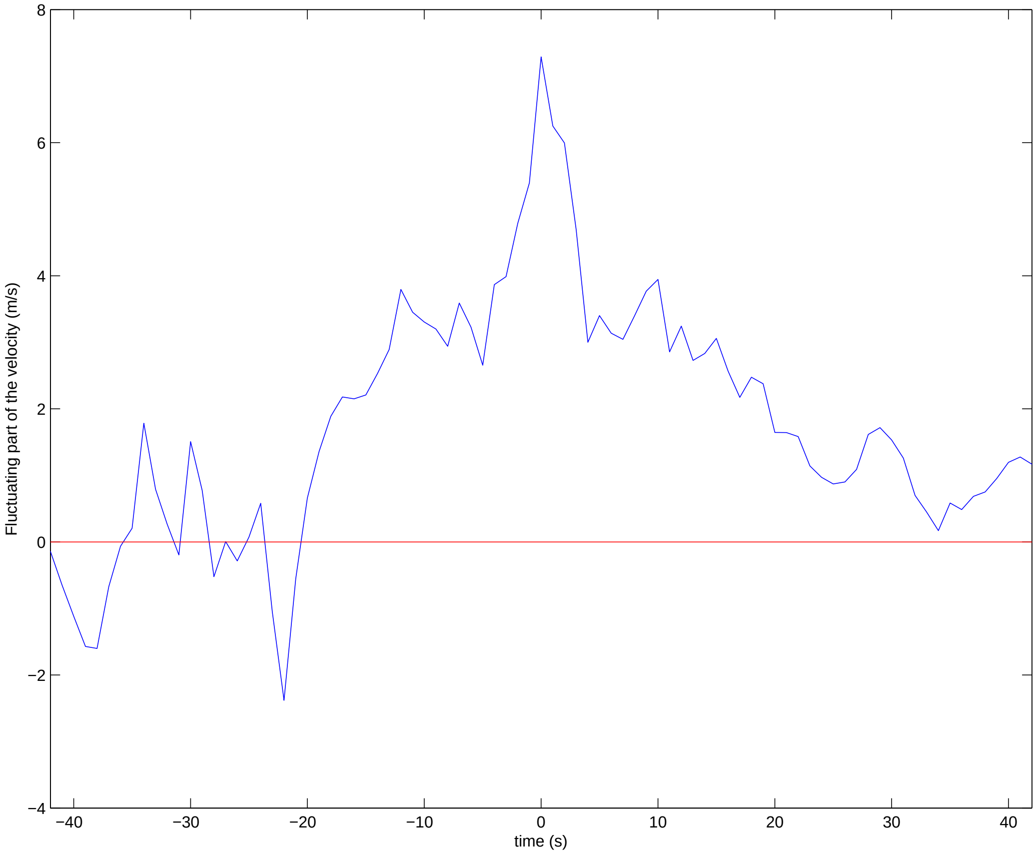

Figure 6.7. Gust BSA: The fluctuating part of the velocity is shown at each time step for the location where the maximum occurs at z = 20 m during candidate BSA.

6.3 Blind Search B

Array II was placed between $(x, y) = (460m : 480m, 640m : 660m)$ at the surface level within the simulated atmosphere in SRII. It monitored 1000 s of data and reported back a large gust event as shown in Fig. 6.8 beginning around t = 419 s. The data during this period of time was converted to a contour plot and it is shown in Fig. 6.9. A larger view of the two dimensional structure is shown in the contour plot in Fig. 6.10 for several time slices. This event peaks in pressure magnitude at 13 Pa. This event moved largely in the y direction with an average speed of 3.6 m/s.

A plot showing z versus y at a constant x during this event is shown in Fig. 6.11 at time slices corresponding to those shown in Fig. 6.10. A constant x was chosen as opposed to y due to the northward propagation of the event. As can be seen in the plot, the event moves through y with strong local x velocity components. This suggests some vorticity created through transverse shear. The maximum velocity above the event occurred at z = 120 m. Fig. 6.12 shows an x-y slice of velocity at z = 120 m. The velocity cluster at z = 120 m moves along a similar trajectory to the pressure event on the ground until it begins to break apart.

GEGT had a difficult time determining the direction of this event because as it propagated northward it shed secondary gusts with significant pressure peaks as can be seen in Fig. 6.10 before breaking up completely. For real world applications of GEGT, users might want to include pressure events that appear at random locations on the array if they occur at the same time. It is highly likely that these events are associated with gusts that are in the process of completely breaking apart. An event in this stage has a high potential to damage structures due to multiple gust loads interacting with the structure from extremely varying angles.

Fig. 6.13 shows time series for the point where the maximum velocity occurs above the pressure event at z = 120 m. The maximum peak is centered with time and is at t = 0 s. This peak differs from the lowest minimum with a 20 s interval of time by 4.2 m/s and has a duration of 12 s. The gust factor associated with BSB is 1.72. BSB meets the criteria discussed in Chapter 1 for gust identification.

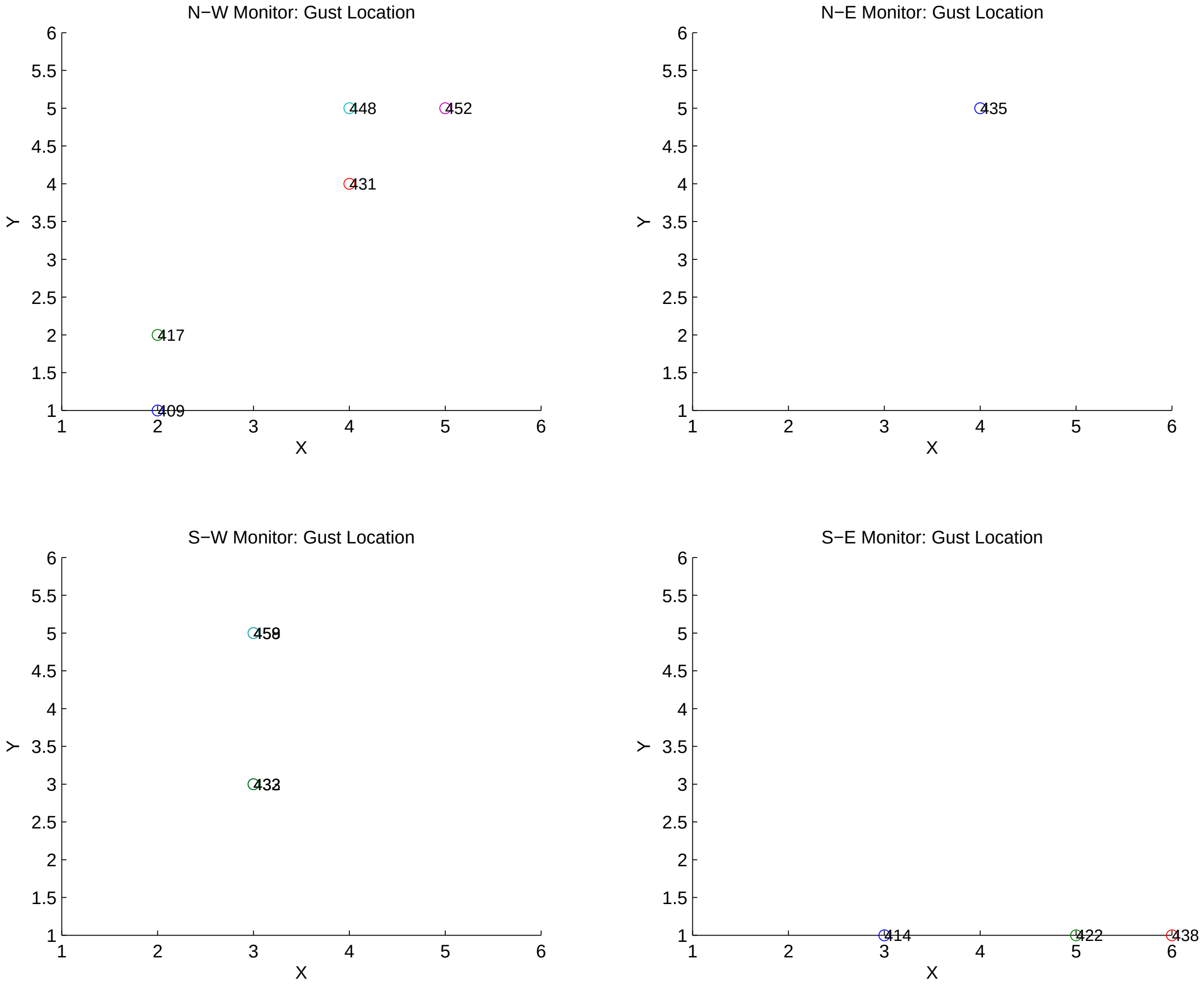

Figure 6.8. BSB: GEGT detected a new gust candidate labeled BSB.

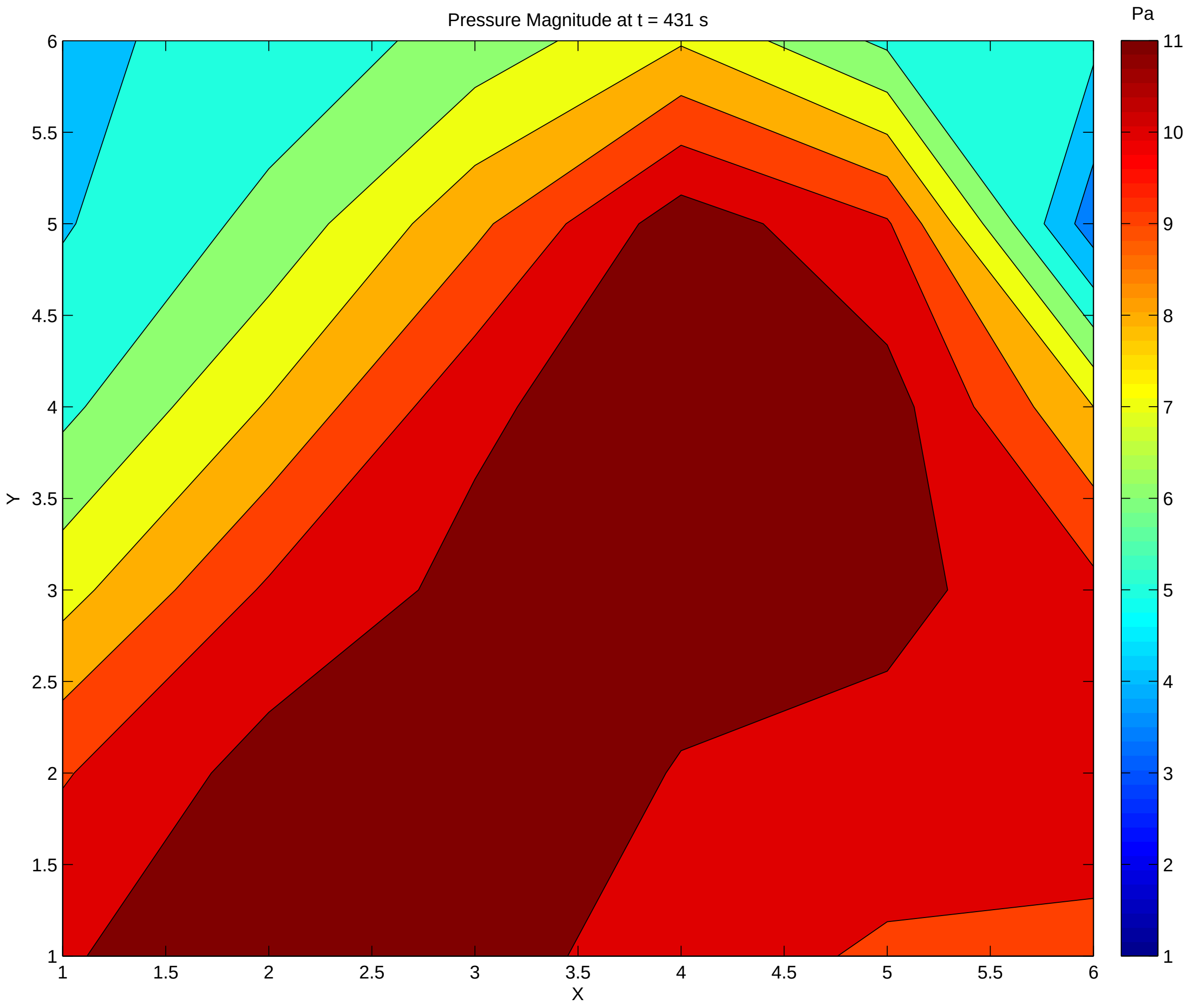

Figure 6.9. BSB: Contour plot of the pressure magnitude with an x-y footprint that is the same size as the array used in Fig.6.8.

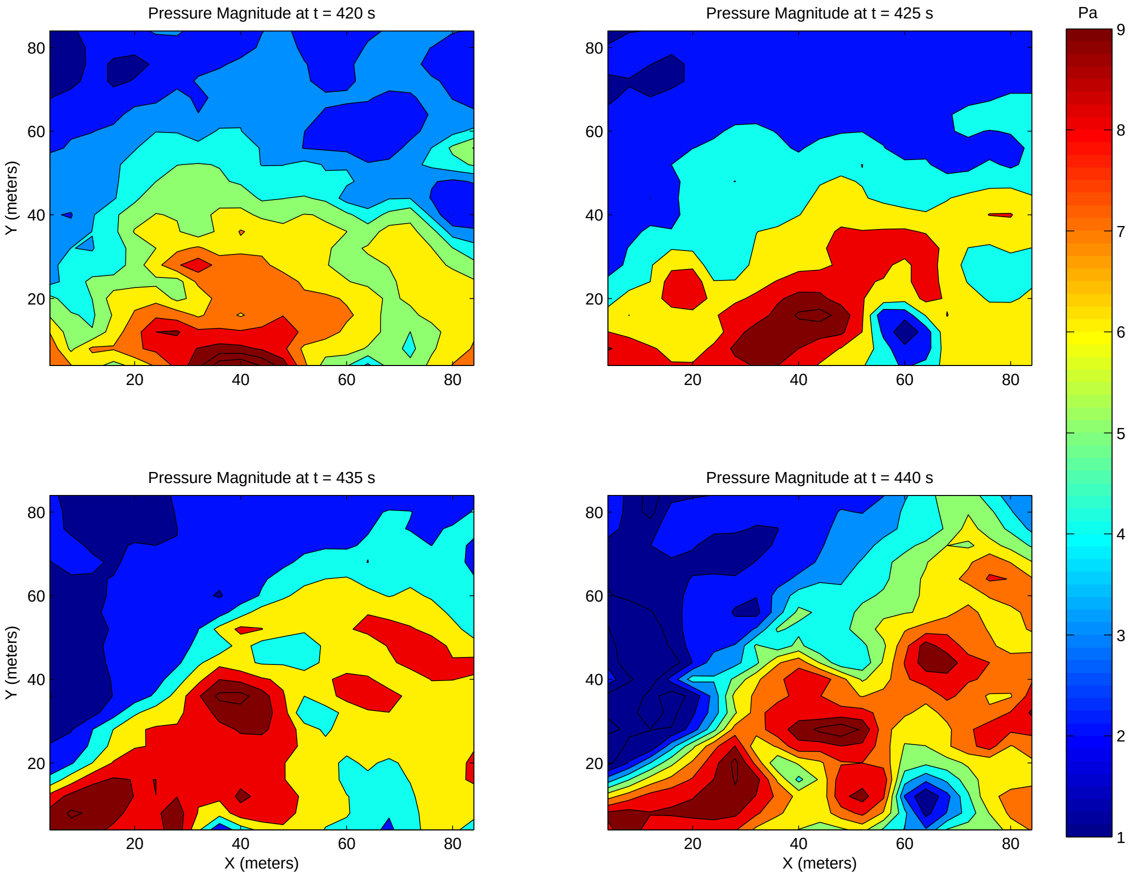

Figure 6.10. BSB: Zooming out from Fig. 6.9 to see the large structure of candidate BSB at several slices in time.

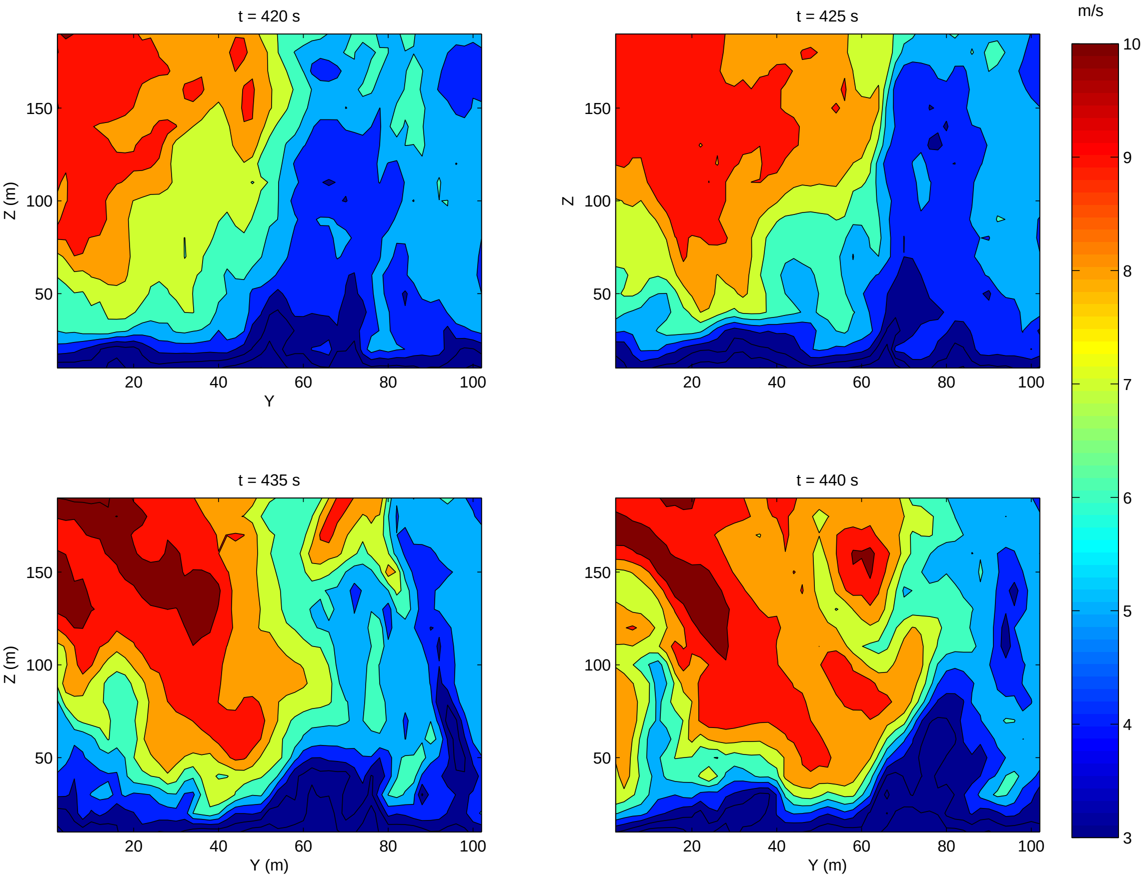

Figure 6.11. BSB: Velocity vs. altitude of candidate BSB as it moves through x = 50 m.

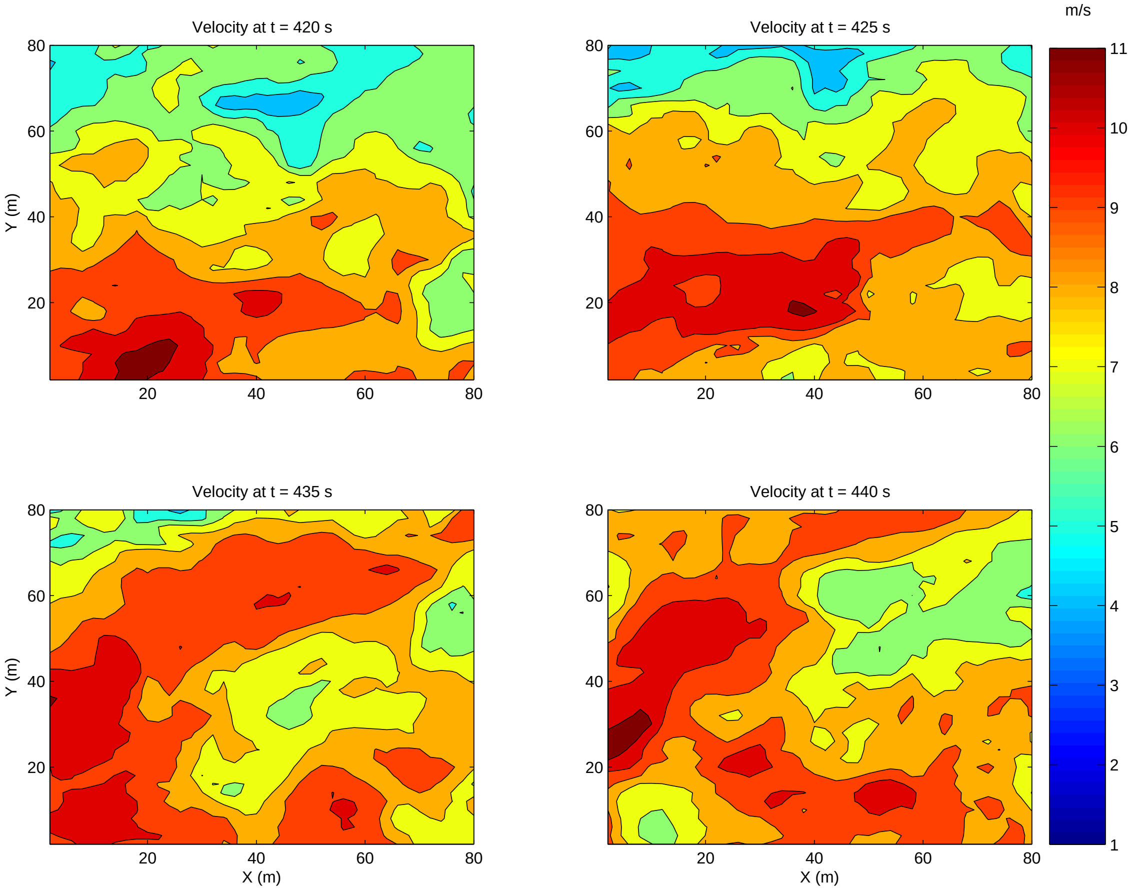

Figure 6.12. BSB: Horizontal slice of velocities at z = 120 m at times corresponding to Fig. 6.10.

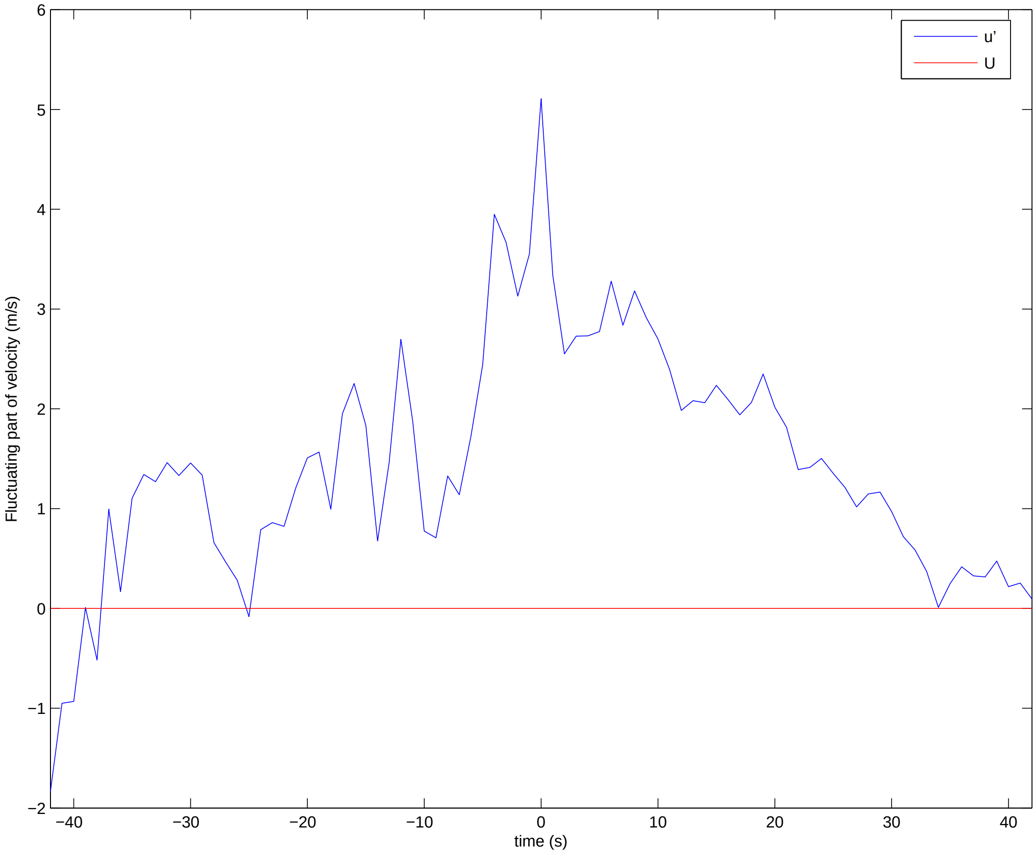

Figure 6.13. Gust BSB: The fluctuating part of the velocity is shown at each time step for the location where the maximum occurs at z = 120 m during candidate BSB.

6.4 Blind Search C

Array II was placed between $(x, y) = (1240m : 1260m, 432m : 452m)$ at the surface level within the simulated atmosphere in SRI. It monitored 1000 s of data and reported back a large gust event shown in Fig.6.14 beginning around t = 360 s. The data during this period of time was converted to a contour plot and it is shown in Fig.6.15. A larger view of the two dimensional structure is shown in the contour plot in Fig.6.16 for several time slices. This event peaks in pressure magnitude at 38 Pa. This event moved largely in the x-direction with an average speed of 3.33 m/s.

A plot showing z versus x for a constant y = 430 m during this event is shown in Fig. 6.17 at time slices corresponding to those shown in Fig. 6.16. The maximum velocity above this event occurred at an elevation of z = 90 m. This suggests that the source of the gust may have originated around this elevation. The x-y velocity time series for this elevation was extracted and shown in Fig. 6.18 at times corresponding to Fig. 6.16. The event here moves almost completely in the x direction just as the pressure disturbance on the ground beneath it as shown in Fig. 6.16. Also, the two events move at nearly the same velocity.

Fig. 6.19 shows time series for the point where the maximum velocity occurs at z = 90 m. The maximum peak is centered with time and is at t = 0 s. This peak differs from the lowest minimum with a 20 second interval of time by 3.8 m/s and has a duration of 20 s. The gust factor associated with BSC is 1.64. Even though the peak-to-minimum difference was just short of the 4 m/s given in Chapter 1 for gust classification criteria it is close enough that BSC is considered to be a gust event.

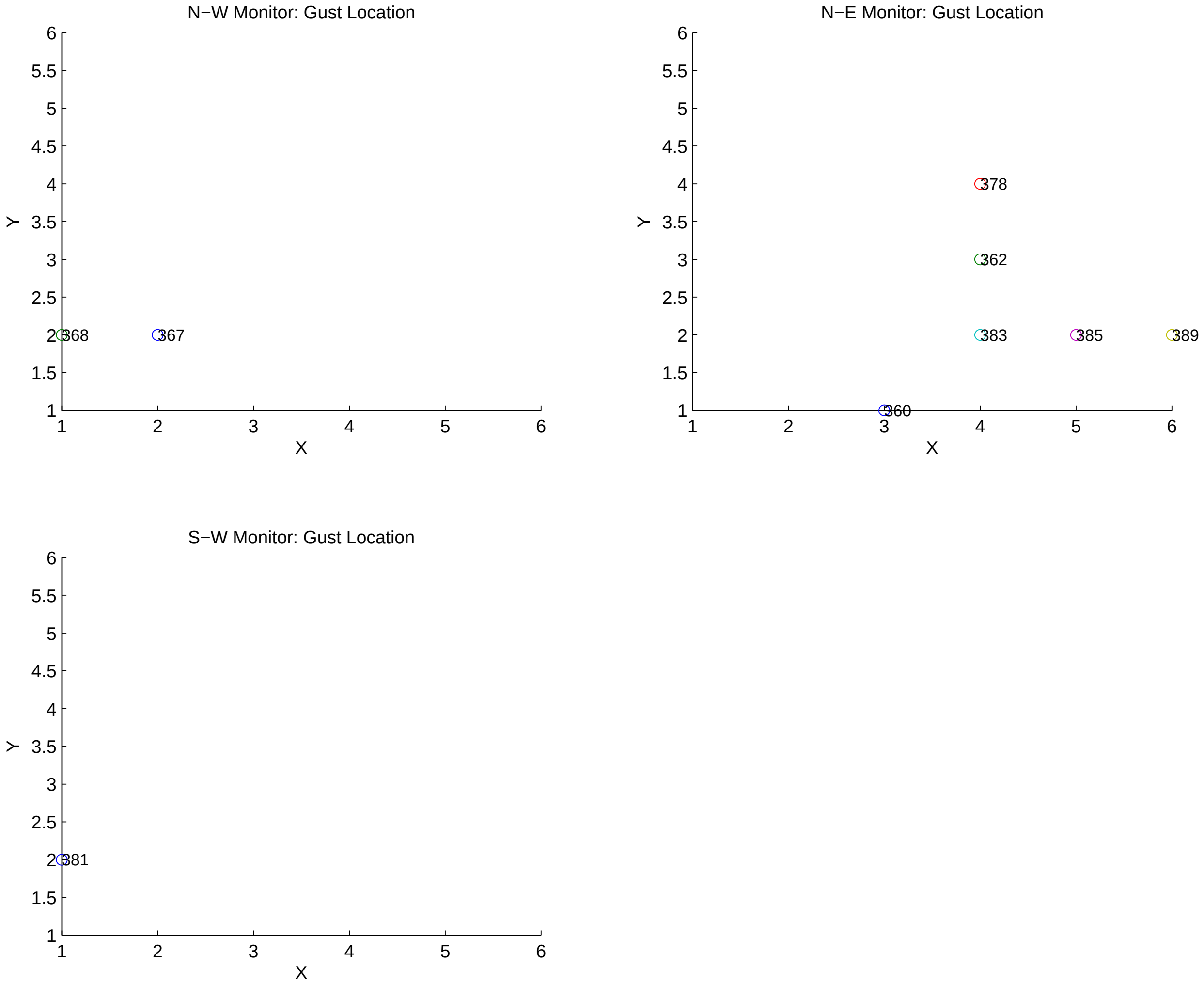

Figure 6.14. BSC: GEGT detected a new gust candidate labeled BSC.

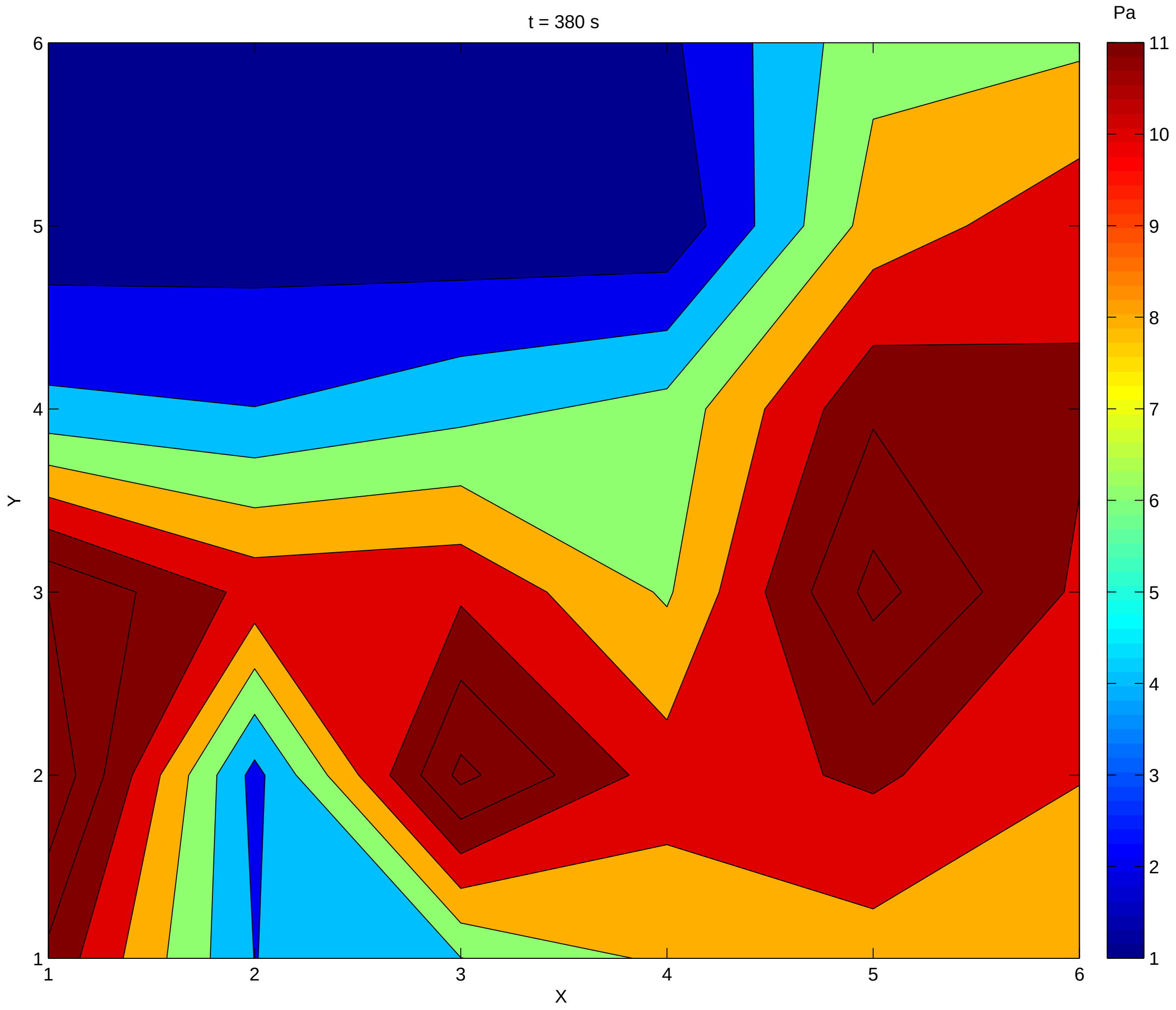

Figure 6.15. BSC: Contour plot of the pressure magnitude with an x-y footprint that is the same size as the array used in Fig. 6.14.

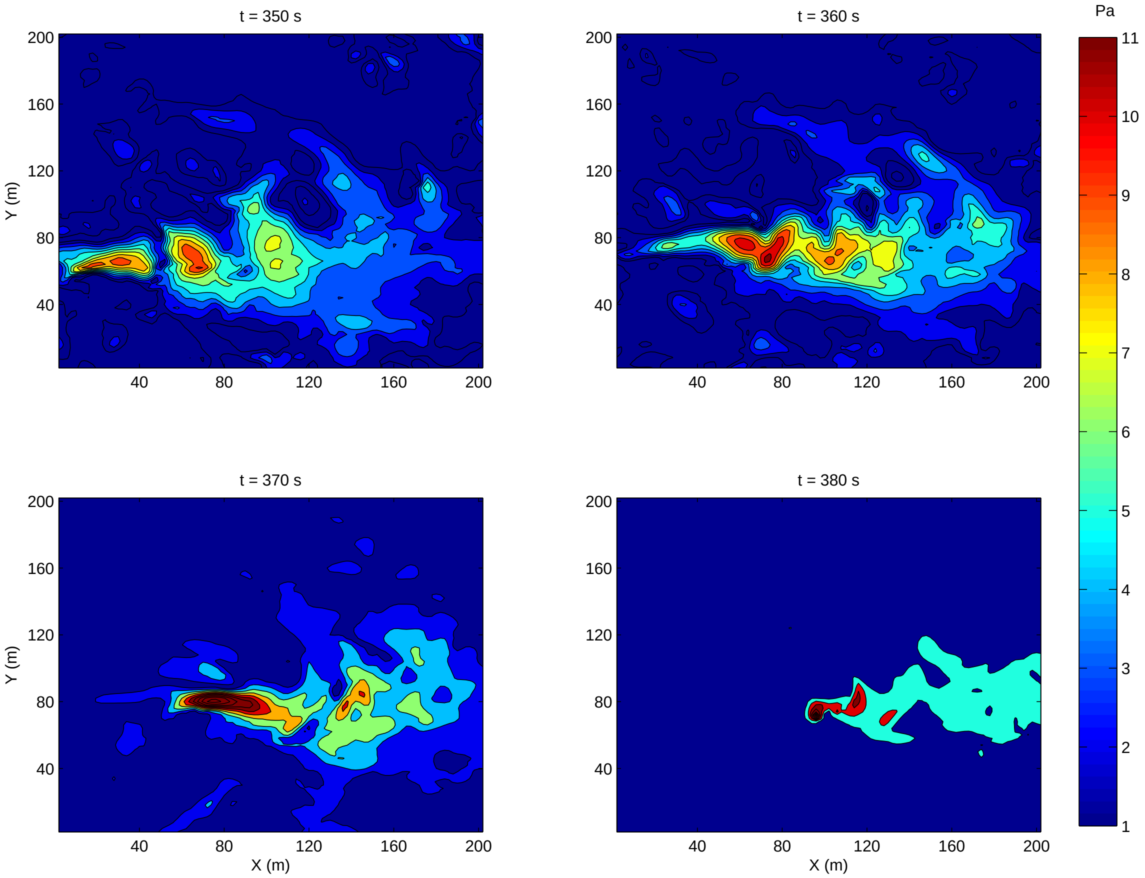

Figure 6.16. BSC: Zooming out from Fig.6.15 to see the large structure of candidate BSC at several slices in time.

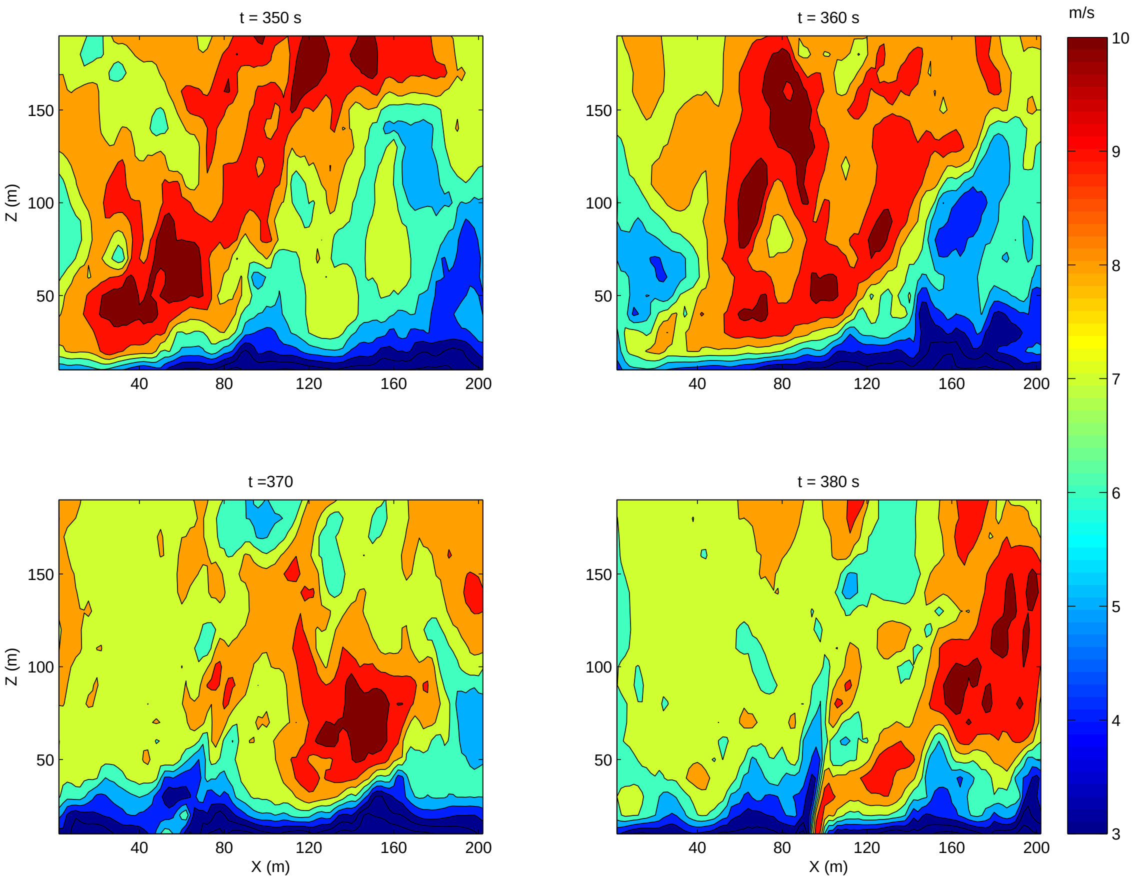

Figure 6.17. BSC: Velocity vs. altitude of candidate BSC as it moves through y = 430 m.

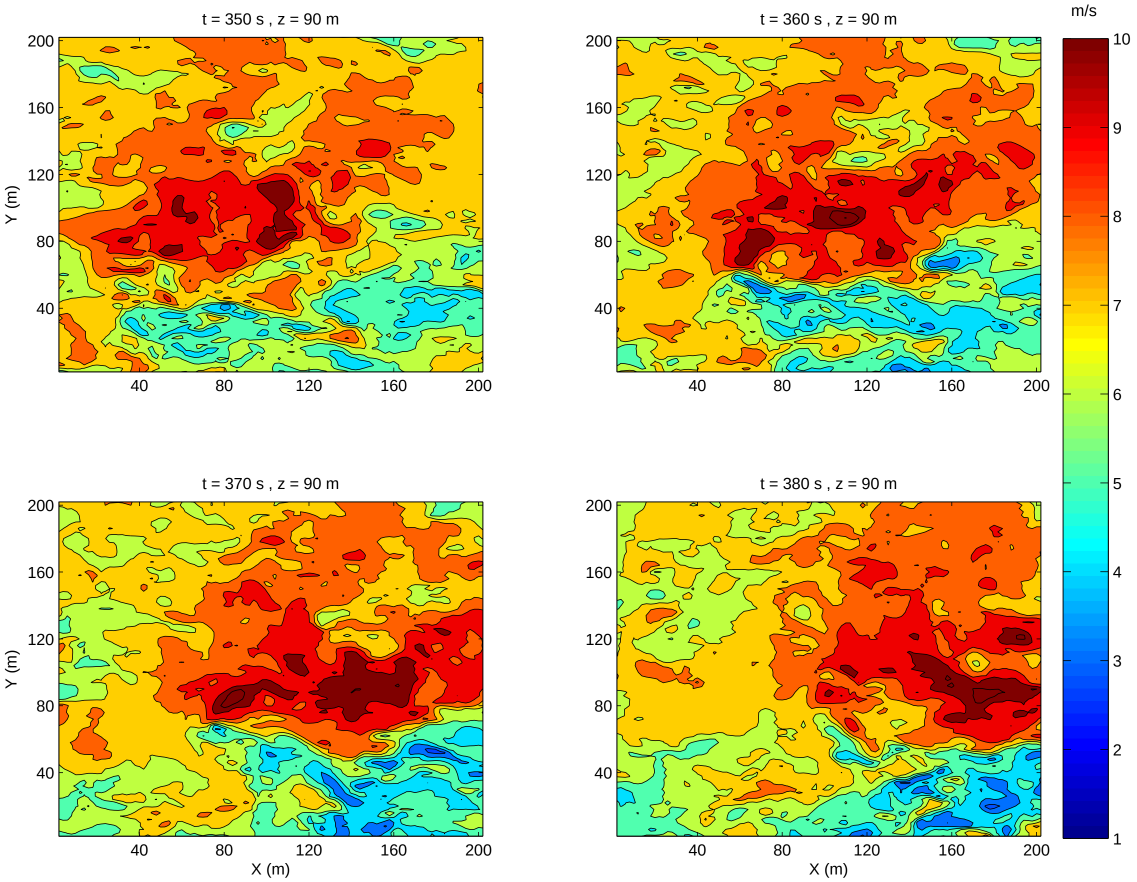

Figure 6.18. BSC: Horizontal slice of velocities at z = 90 m at times corresponding to Fig. 6.17.

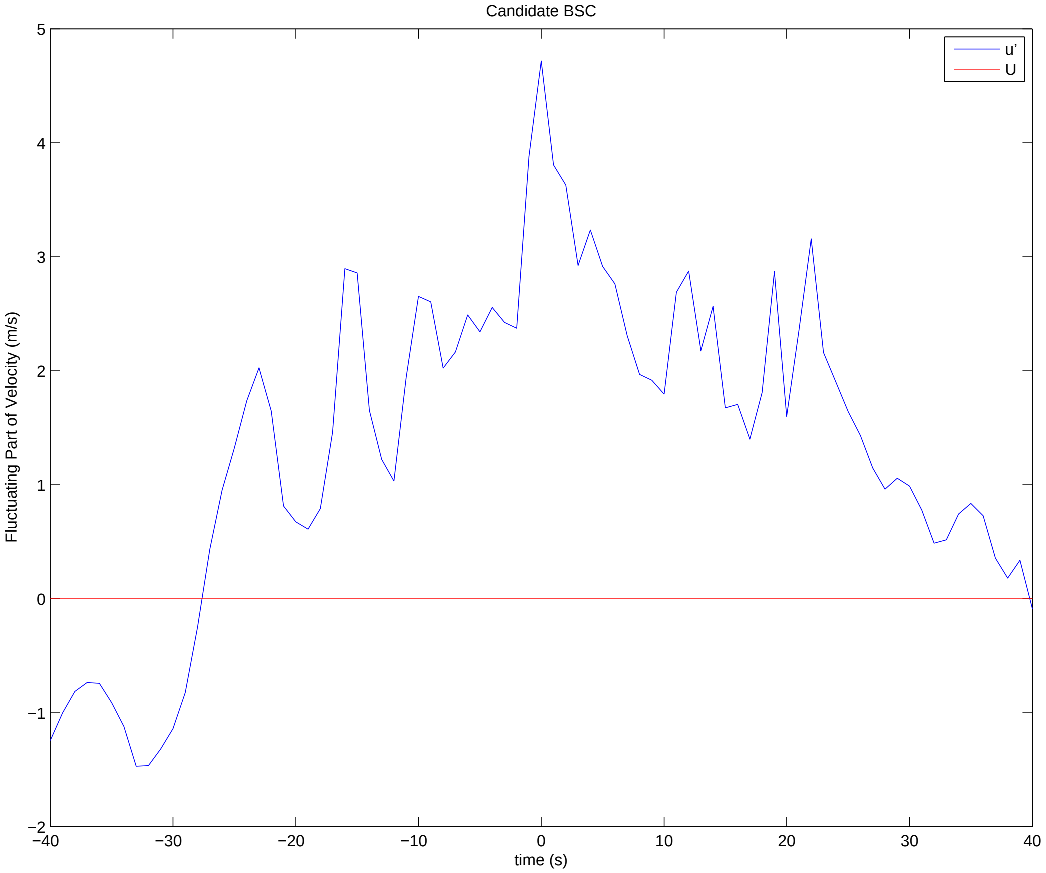

Figure 6.19. Gust BSC: The fluctuating part of the velocity is shown at each time step for the location where the maximum occurs at z = 90 m during candidate BSC.

6.5 Blind Search D

Array II was placed between $(x, y) = (1060m : 1080m, 940m : 960m)$ at the surface level within the simulated atmosphere in science run II (SRII). It monitored 1000 s of data and reported back a gust event shown in Fig. 6.20. Fig. 6.21 shows a contour plot of the same foot print occupied by the simulated array. The pressure cluster has an average speed of 3.5 m/s almost entirely in the y direction. Note that the cluster breaks into two separate clusters after t = 745 s and that GEGT detected both of the new clusters and reported them as gusts.

Fig. 6.22 is Fig. 6.21 zoomed out to show the entire two dimensional pressure cluster. There are two distinct clusters along x = 1080 m at approximately y = 940 m and y = 1060m. These correspond to the two large features shown in the altitude versus y plot shown in Fig. 6.23 for x = 1080 m. The maximum velocity occurs at z = 40 m just above the pressure feature near y = 940 m and it is u = 10.7 m/s.

Fig. 6.25 shows a time series for the point where the maximum velocity occurs at z = 40 m. Within a 20 second duration the maximum peak at t = 0 differs from the lowest minimum at t = -13 s by 5.1 m/s. A new peak begins at t = -4 s. The duration for this event was 17 s. The maximum location at z = 40 m was found to be 10.7 m/s. The ten minute mean was U = 6 m/s yielding a gust factor of 1.78. BSD falls well within the gust classification criteria discussed in Chapter 1.

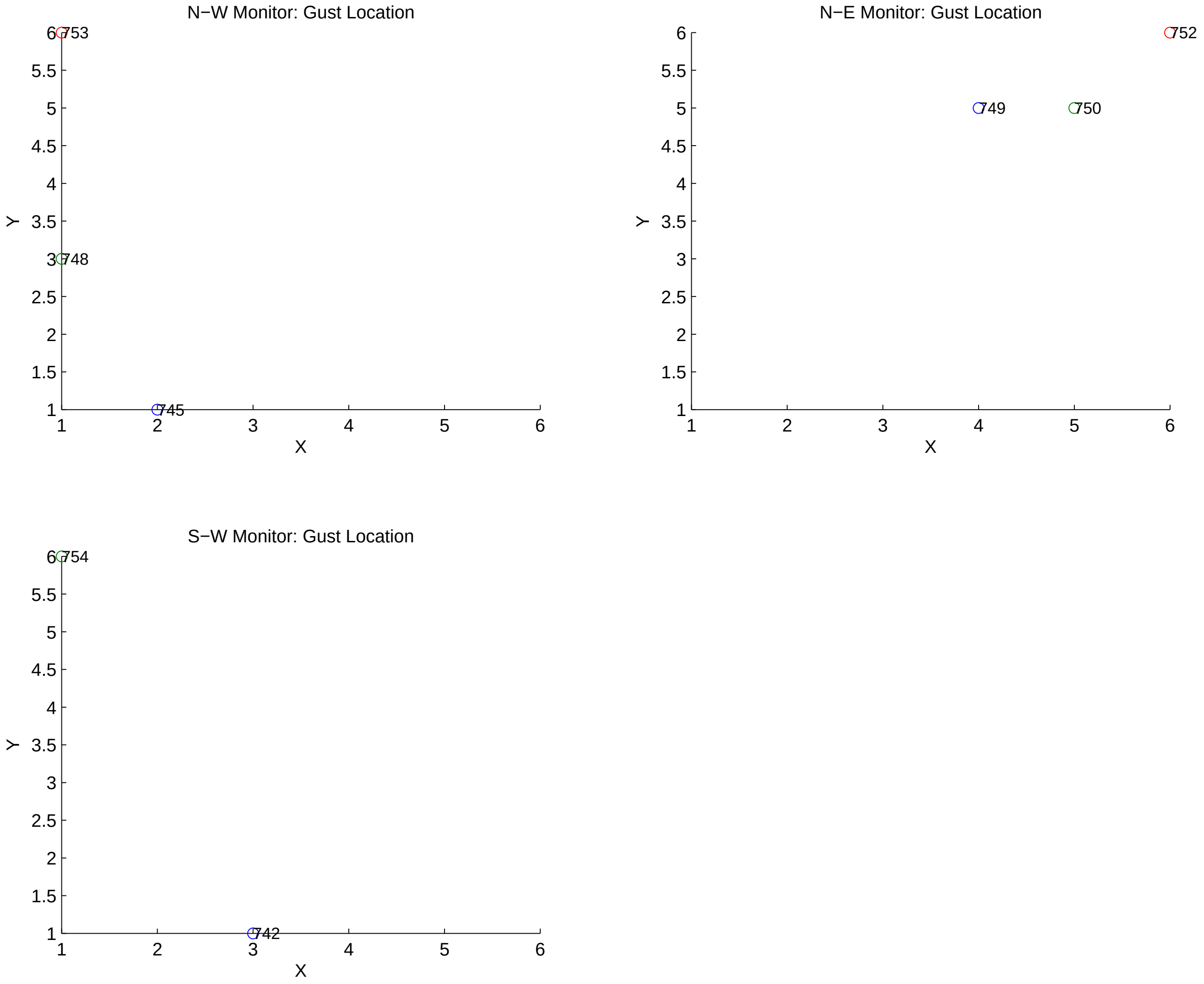

Figure 6.20. BSD: GEGT detection of candidate BSD.

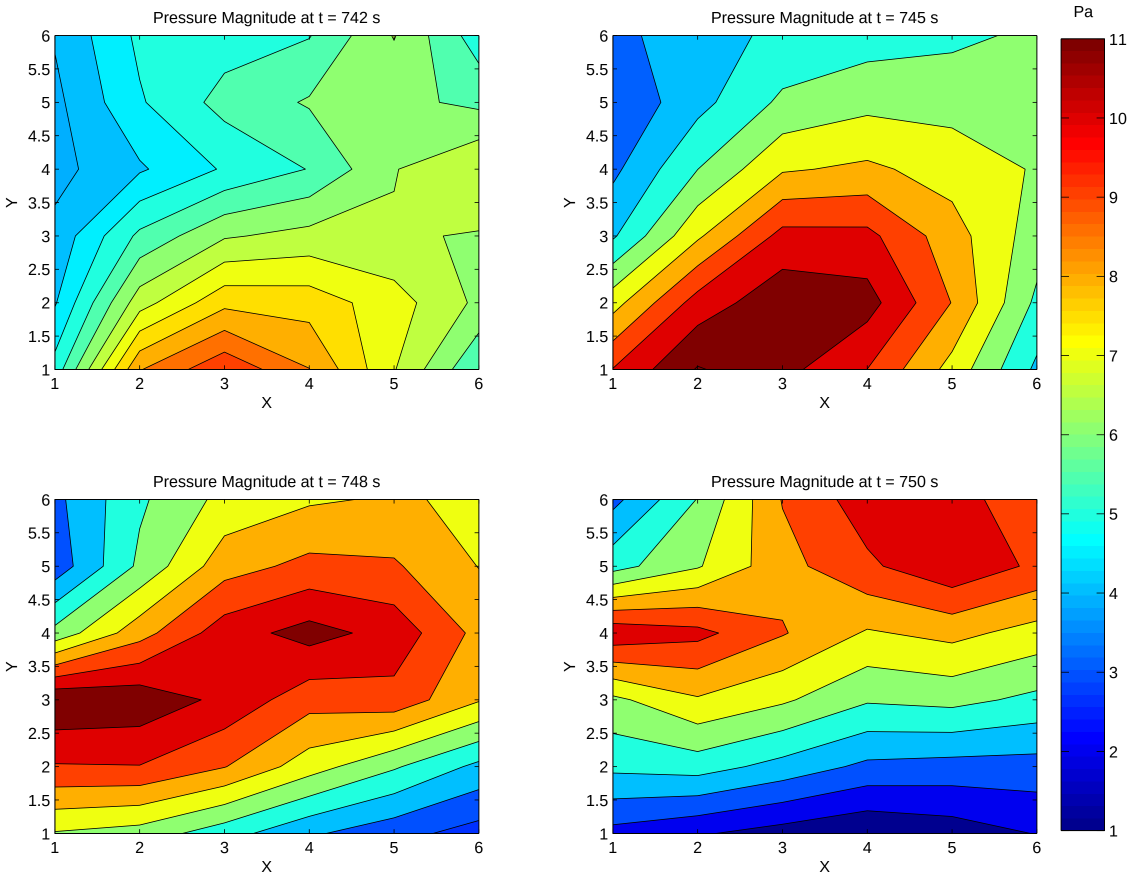

Figure 6.21. BSD: Horizontal slice of the pressure magnitude (Pa) with an x-y footprint that is the same size as the array used in Fig. 6.14 at several time steps.

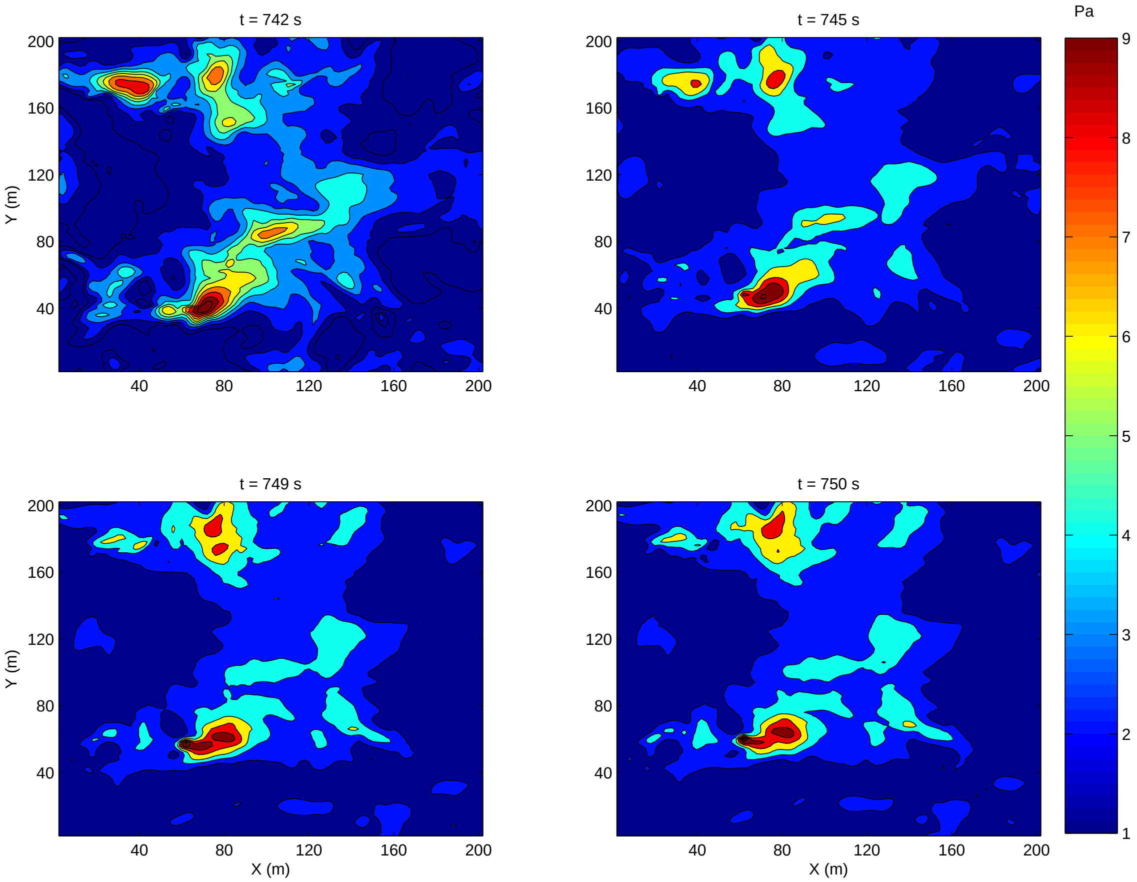

Figure 6.22. BSD: Zooming out for Fig. 6.21.

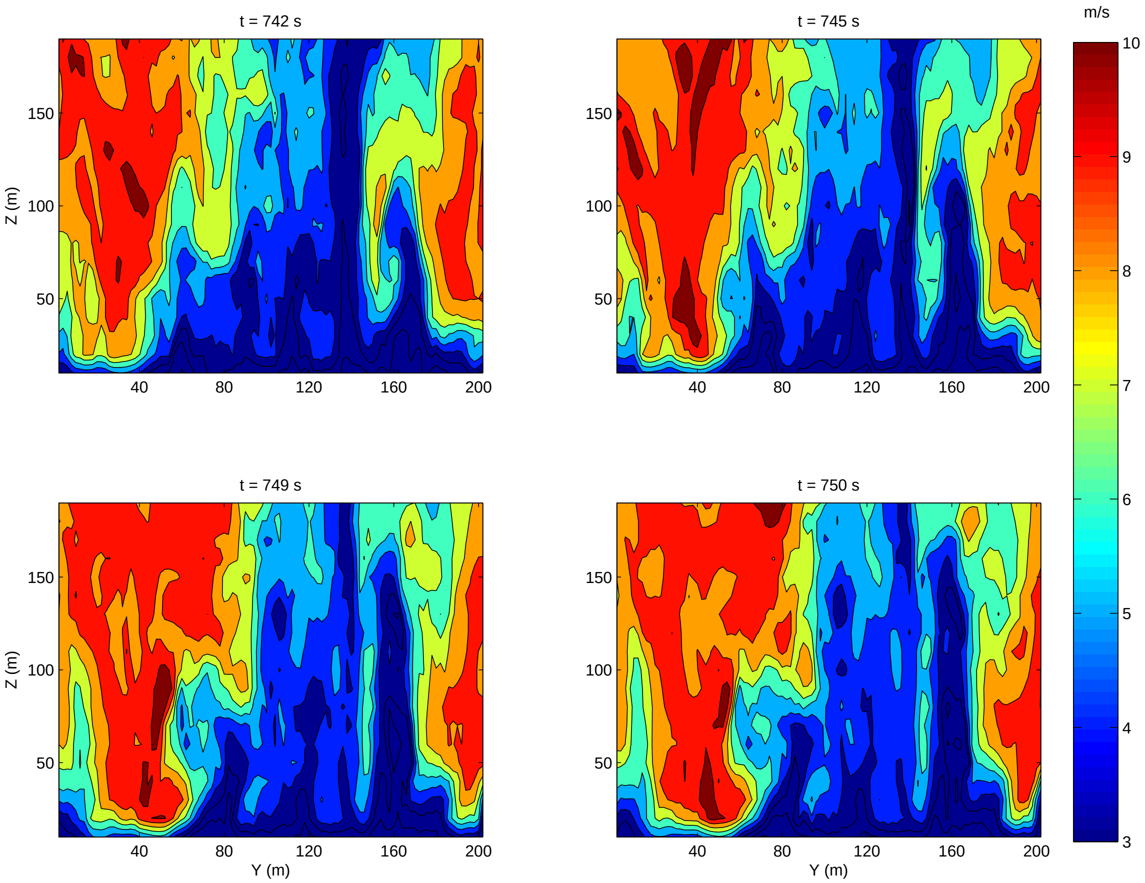

Figure 6.23. BSD: Velocity vs. altitude of candidate BSD as it moves through x = 1080 m.

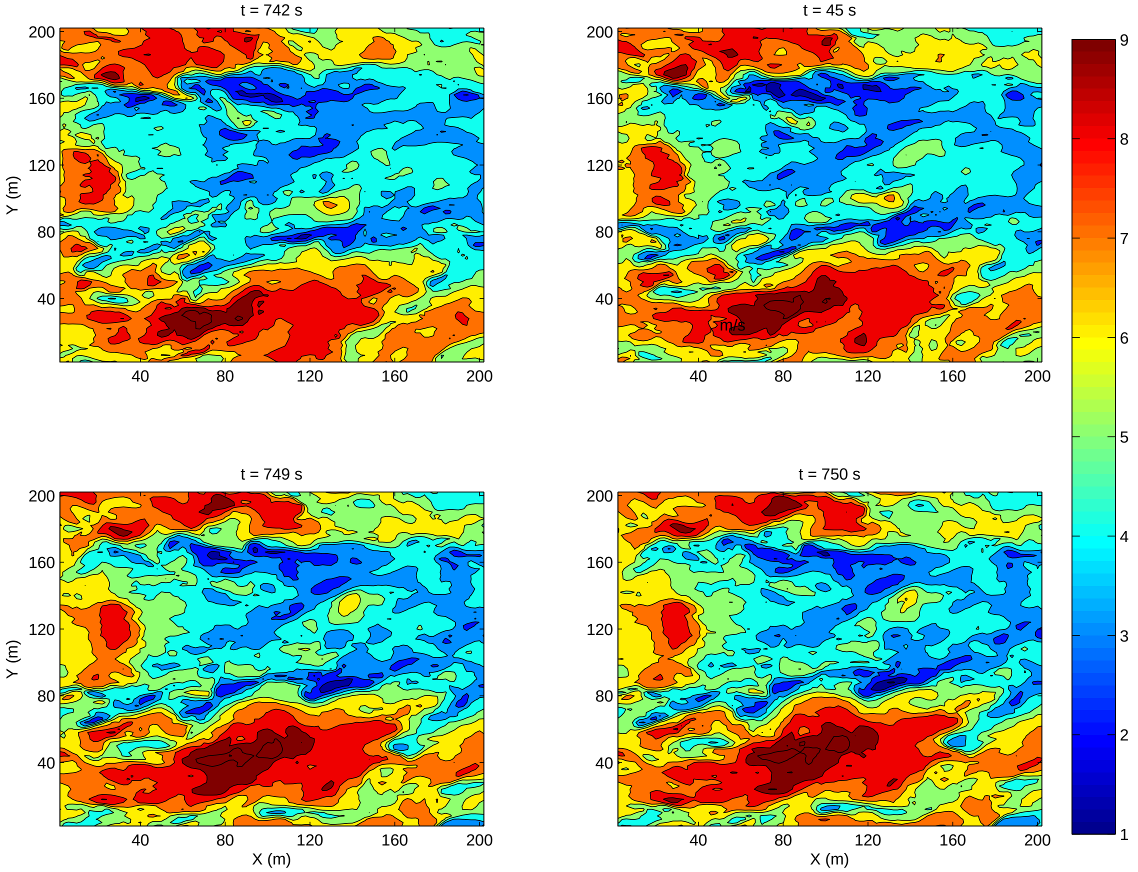

Figure 6.24. BSD: Horizontal slice of the velocities at z = 40 m.

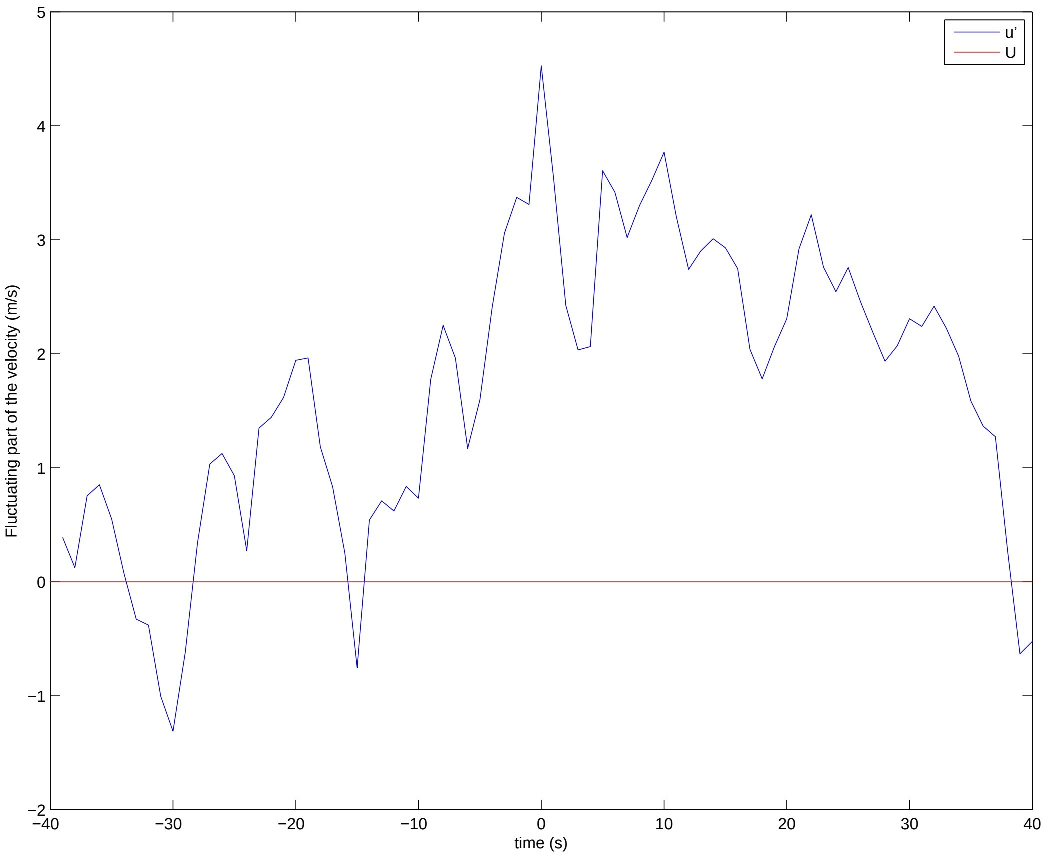

Figure 6.25. Gust BSD: The fluctuating part of the velocity is shown at each time step for the location where the maximum occurs at z = 40 m during candidate BSD.

6.6 Blind Search E

Array II was placed between $(x, y) = (530m : 550m, 640m : 660m)$ at the surface level within the simulated atmosphere from SRII. It monitored 1000 s of data and reported back a gust event shown in Fig. 6.26. Fig. 6.27 is a contour plot of the event with the area extended so that the entire two dimensional structure can be viewed. The maximum pressure peak in this cluster is 27.5 Pa. Altitudes above this maximum were scanned for a maximum velocity which was 13.2 m/s at z = 80 m in the velocity cluster shown in Fig. 6.28. This cluster of velocities is moving at approximately the same group velocity as the pressure event below and in a similar direction. The pressure peak in the cluster event on the ground is moving at 6.68 m/s.

Fig. 6.29 shows a time series for the point where the maximum velocity occurs at z = 80 m. The maximum peak at t = 0 differs from the minimum at t = -5 by 4.3 m/s. The event has a duration of 10 s. BSE fits the criteria for gust classification discussed in Chapter 1. It has a gust factor of 1.9.

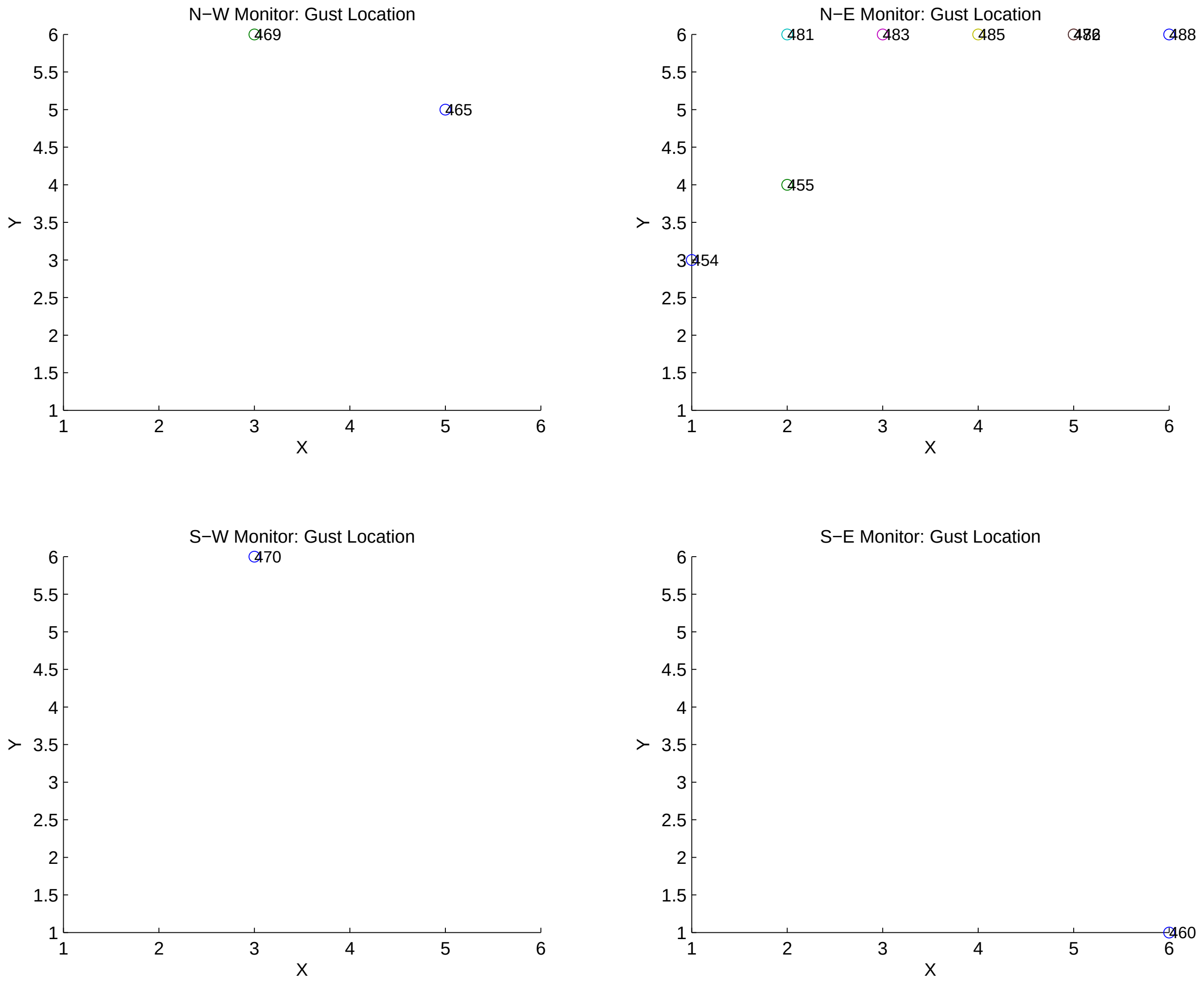

Figure 6.26. BSE: GEGT detected a new gust candidate labeled BSE.

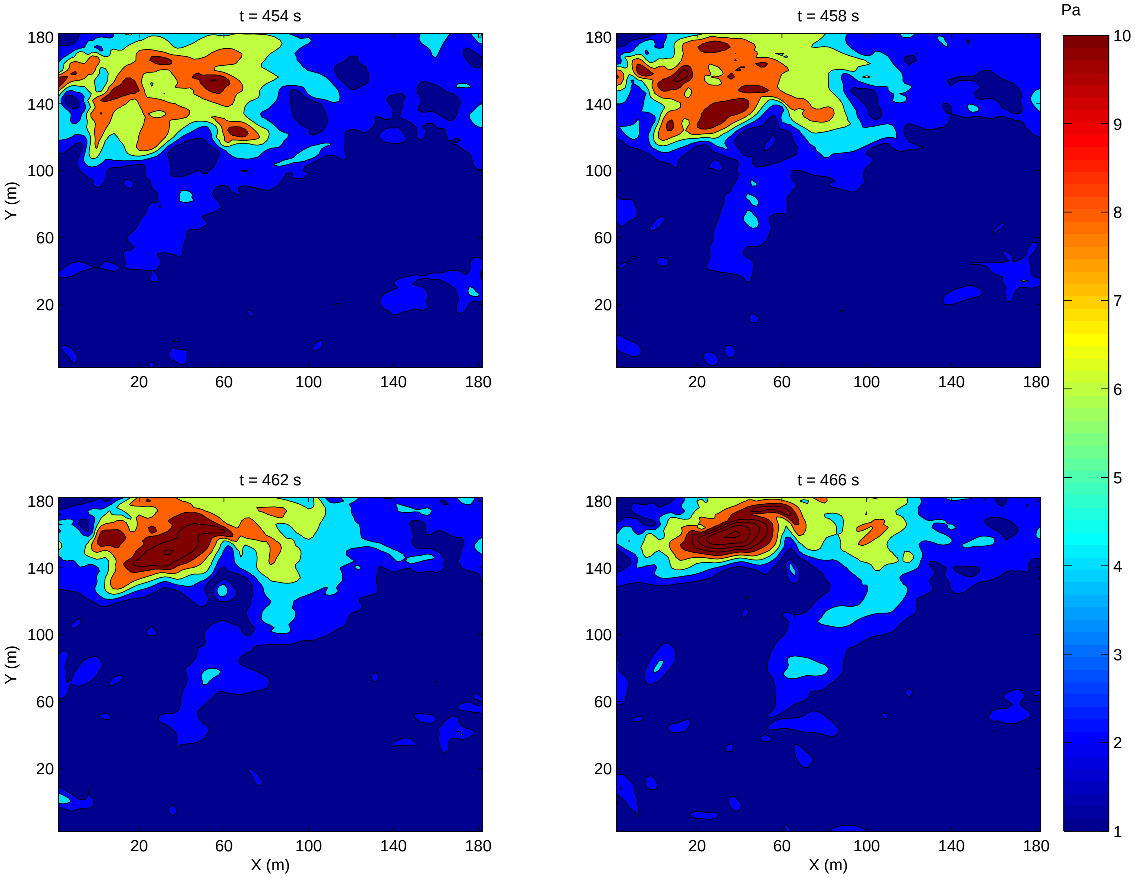

Figure 6.27. BSE: Horizontal slice of the pressure magnitudes for Fig. 6.26 zoomed out.

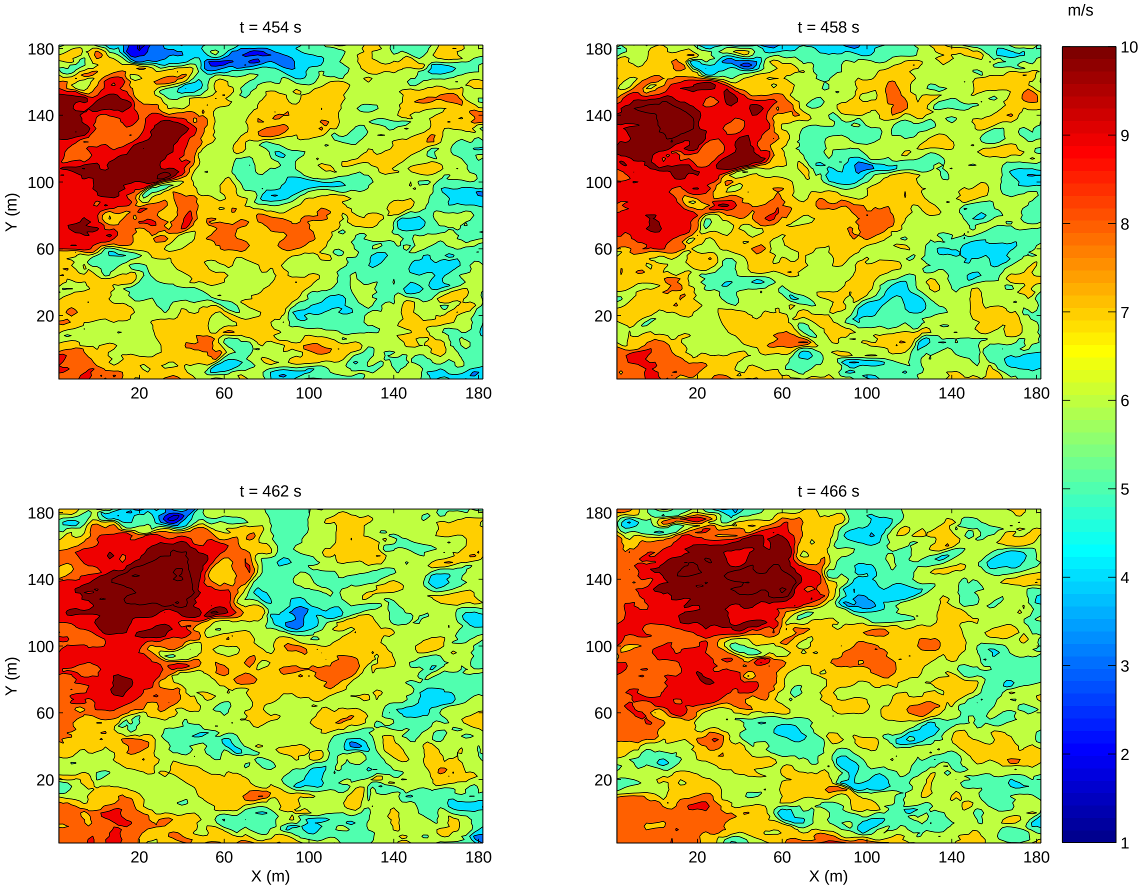

Figure 6.28. BSE: Horizontal slice of the velocity at z = 80 m.

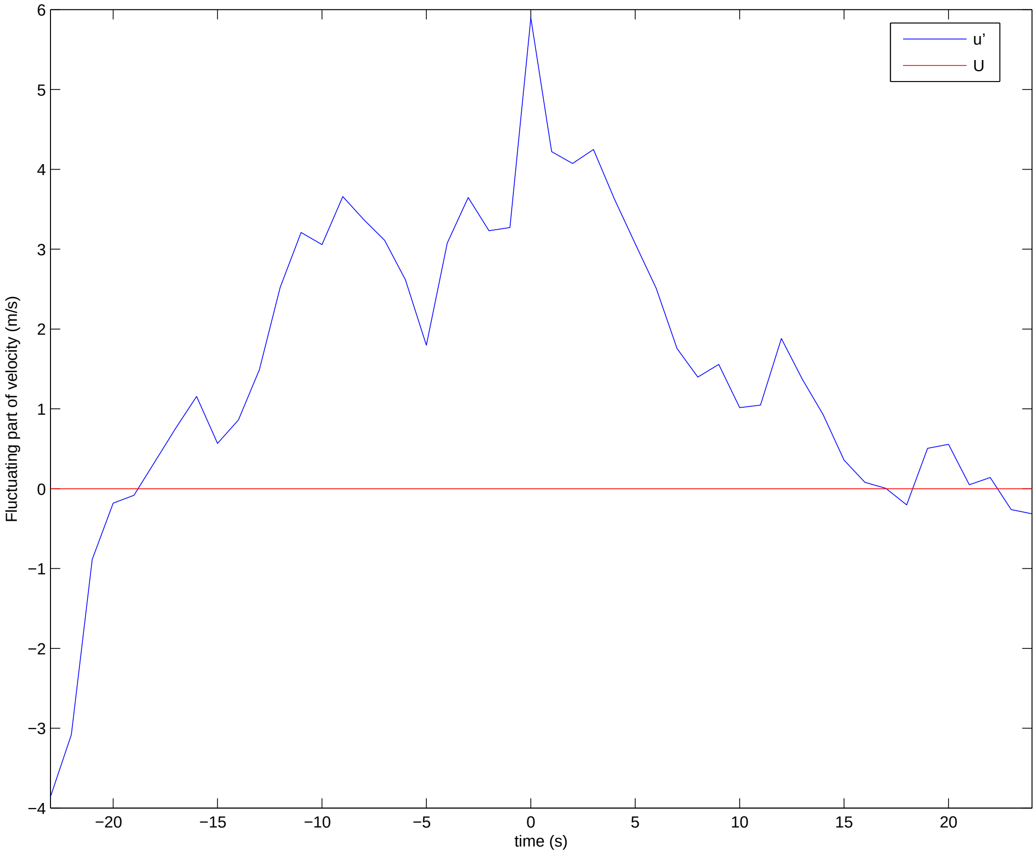

Figure 6.29. Gust BSE: The fluctuating part of the velocity is shown at each time step for the location where the maximum occurs at z = 80 m during candidate BSE.

6.7 Summary of Ground-based Elevated Gust Tracker Tests

Array II selected from Chapter 5 was placed beneath the simulated atmosphere generated by two different LES's at various locations. The data sets from the LES's were called SRI and SRII. GEGT processed the data recorded by the array and reported five pressure events that propagated through the array at rates that exceeded the wind velocity on the ground. Each of these five events were at five different locations on the ground within the LES data. Locations in which there were no identifications were checked for false negatives by searching for maxima in the pressure in that specific location. No false negatives were identified.

Plots of horizontal slices of the pressure at the ground were generated for each of the five events to visually observe the two dimensional structure, path through the horizontal plane, and the general spatial and temporal locations. The maximum of the velocities above this event was determined and a horizontal slice of the velocity at the altitude containing the maximum was generated. It was observed that the two dimensional structure of the velocity cluster moved along the same horizontal path as the pressure structure. Additionally, the signals had identical spatial and temporal locations.

The two dimensional time series of the velocity that contained the maximum velocity that corresponded to the pressure event below was separated into mean and fluctuating parts. The fluctuating part was plotted against time so that gust classification criteria outlined in Chapter 1 could be used to determine whether or not these signals were gusts. Most of the signals fell within the gust classification criteria and the one that did not, BSC, was so close that it is considered a gust event for the sake of this project.

Table 6.1 summarizes data collected from the blind searches as well as candidates A, B, and C. With GEGT, the PTV_{avg} was more accurately calculated for A,B, and C and updated in this table. The highest gust factor occurred at an altitude of z = 20 m and the lowest at z = 90 m. Though there were not enough gust events to do any statistics on the variations of gust factors with altitude, the values overall seem to trend down with increasing height which would be in agreement with previous research discussed in Chapter 1.

GEGT successfully detected pressure fluctuations on the ground and identified them as possible gusts. It also had reasonable success in determining the direction of the events. When the gusts above the ground break up the pressure events break into several clusters. The direction calculation tends to fail under these conditions because there are several pressure clusters moving through the array and as the amplitude of each cluster changes the maximum appears to jump to different clusters. What is really happening is that the amplitude in one of the clusters has decreased just enough so that the amplitude in another cluster becomes the new maximum. This can be easily overcome because when this does happen the pressure maxima that are reported as gusts are still consecutive in time.

Table 6.1. Summary of data from cross-correlation candidates and blind searches in order by increasing altitude z of the maximum gust.

$Candidate$	$z(m)$	$PTV_{avg}\ (m/s)$	$Peak\ Gust\ Velocity\ (m/s)$	G
BSA	20	2.7	15.0	2.0
A	20	3	12.0	2.2
BSD	40	3.5	12.4	1.8
B	80	4.8	11.3	1.6
BSE	80	6.68	13.4	1.9
BSC	90	3.33	12.1	1.6
C	90	6.4	12.3	1.6
BSB	120	3.6	13.6	1.7

CHAPTER 7: CONCLUSIONS

The primary goals of this research are to investigate relationships between gusts aloft in the atmospheric boundary layer and pressure fluctuations on the ground beneath them and to use the results of these investigations to develop a pressure sensing ground based array and processing method to detect and identify fast moving ground pressures that correspond to elevated gusts. The data were generated using a LES to simulate a convective boundary layer which provided a time series for full field velocities and pressures.

The first part of these goals was reached through visual identification of elevated gusts and their corresponding pressure responses on the ground followed by a cross-correlation analysis between the CWTs of velocities at points in the gust and the pressures of points on the ground. The CWT cross-correlations are a measure of how similar the time evolution of each signal's frequency content is. The CWT cross-correlation studies yielded high correlation coefficients suggesting that the signals from the elevated gust events are associated with the signals from the pressures measured on the ground beneath them. Parameters for ground based detection, such as the speed of the pressure fluctuations on the ground and the sizes of the pressure clusters on the ground, provided a starting point for designing a ground based array.

The second part of the project goals was to design a ground based array and processing routines to track fast moving pressures that could correspond to elevated wind gusts. Various array geometries were explored with practical applications such as wind turbine damage prevention in mind. A design was selected based on it's resolution and it's ability to house a structure such as a wind turbine. A processing routine called GEGT was written for the array that successfully identifies fast moving pressure features on the ground and identifies them as being associated with elevated gusts if they exceed the velocities measured at the ground.

Several new gust candidates were found using GEGT with the array design. Each signal that was discovered was compared to the standard definition of a wind gust and most of them met the criteria while some were so close that they were considered a gust for this project. Results from the GEGT blind searches showed the highest gust factor at the lowest altitude and the lowest gust factor at the highest altitude in agreement with the outdoor research done in White Sands discussed in Chapter 1. The events identified with GEGT did not have gust factors that would be out of place in the distribution of turbulent intensities generated by the virtual tower from Fig.3.2 or from the White Sands experiments.

The average peak pressure transfer velocities (PTV_{avg}) for each event were calculated using the change in peak location divided by the change in time over the duration of the event. These values are plotted against the altitude in which the maximum elevated gust velocities corresponding to the pressures on the ground occurred as shown in Fig. 7.1. As expected, the peak PTV_{avg} increased with increasing altitude. The two outliers are from BSC and BSB. BSB is the extreme outlier and is most likely due to the difficulties in determining the PTV_{avg} because the event broke up into several distinct clusters over the array. Since the mean wind speed changes overtime, it is likely that BSC represents a fluctuation that is propagating in a lull in the mean wind. Overall these results suggest that with many more detections using numerical simulations, a rough trend could be developed to estimate the altitude of the maximum elevated gust velocity from the transport velocities of corresponding pressure fluctuations on the ground. However, even with the limited number of events identified in this project the trend shows that the faster the moving pressure fluctuations on the ground propagate, the higher up the corresponding gust sources will be. In the literature review in Chapter 1, Priestly obtained the result that long wavelength disturbances in the pressure were correlated with high altitude events. Priestly developed a mathematical relationship that suggested that as the wavelength of the pressure disturbance increases the altitude of the source increases. Wind profiles show that the mean wind speed increases logarithmically with altitude and so the expectation is that the faster the velocity of the wavelength disturbance in the pressure is the higher in altitude its velocity source will be. Overall the results from this project do show that with an increase in the rate at which the pressure moves across the surface there is an increase in the altitude of its gust source.

False positives and negatives were searched for in this project. A false positive means that there is a pressure response on the ground that behaves like an elevated gust induced ground pressure without any significant elevated velocity event above to trigger it. False positives were searched for visually and using GEGT without any identifications. A false negative means that an elevated gust event occurs up high and induces a pressure response on the ground but GEGT misses it. This type of false negative was not seen during the blind searches. To make sure, the pressure was monitored visually during GEGT runs. Another situation of interest is an elevated gust event occurring without any noticeable pressure response on the ground. However, several elevated velocity events were isolated at several altitudes during this project and there was always a significant response in the pressure on the ground below.

In the future, the methods developed in this project could be applied to nighttime boundary layers. At night there is less noise compared to day time boundary layers and so it is expected that data analysis will be less challenging. The array and processing script developed as part of this research is ready to be used in outdoor experimentation. It could also be used to probe features in the atmospheric boundary layer such as wake turbulence generated at wind turbine farms or features related to Kelvin-Helmholtz instabilities. Ultimately, the methods developed in this research could be used as an early warning detection system for wind turbine damage control and for aircraft safety.

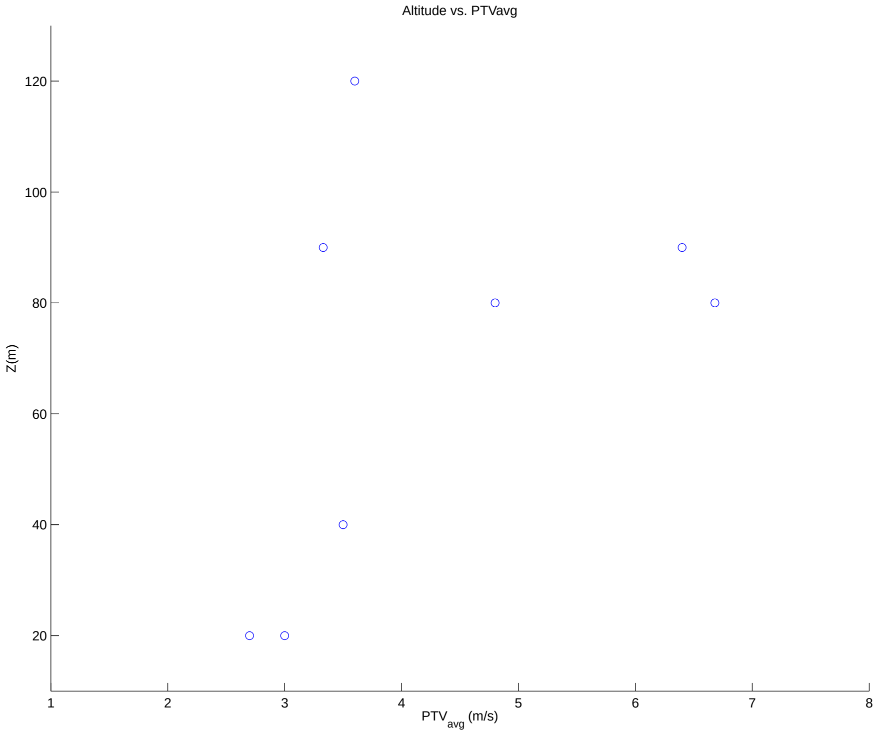

Figure 7.1. Location of maximum elevated gust velocities versus the corresponding average pressure transfer velocities on the ground.

BIBLIOGRAPHY

[1] Hans Panofsky and John Dutton. *Atmospheric Turbulence.* Wiley Interscience, first edition, 1984.

[2] R.B. Stull. *An Introduction to Boundary Layer Meteorology.* Kluwer Academic Publishers, first edition, 1988.

[3] George Stokes. On the effect of the internal friction of fluids on the motion of pendulums. *Transactions of the Cambridge Philosophical Society*, 9:106–114, 1851.

[4] Osborne Reynolds. An experimental investigation of the circumstances which determine whether the motion of water shall be direct or sinuous, and of the law of resistance in parallel channels. *Philosophical Transactions of the Royal Society*, 174:935–982, 1883.

[5] Osborne Reynolds. On the dynamical theory of turbulent incompressible viscous fluids and the determination of the criterion. *Philosophical Transactions of the Royal Society*, 186:123–161, 1894.

[6] J. Boussinesq. Essai sur la th eorie des eaux courantes. *M em. pr es. par div. savant ‘a lAcad. Sci.*, 23:1–680, 1877.

[7] L. Prandtl. ericht uber untersuchungen zur ausgebildeten turbulenz. *Zs. agnew. Math.Mech.*, 5:136–139, 1925.

[8] G.I. Taylor. Statistical theory of turbulence. *Proc. Roy. Soc. London A*, 151:421–478, 1935.

[9] A. N. Kolmogorov. The local structure of turbulence in incompressible viscous fluid for very large reynolds numbers. *Royal Society (London), Proceedings, Series A - Mathematical and Physical Sciences*, 431(1890):9–13, 1941.

[10] S. Corrsin. Turbulent flow. *Am. Scientist*, 49:300–325, 1961.

[11] J. Smagorinsky. General circulation experiments with primitive equations. *Mon. Weath. Rev.*, 91:99–164, 1963.

[12] J.W. Deardorff. A numerical study of three-dimensional turbulent channel flow at large reynolds numbers. *J. Fluid Mech.*, 41:453–480, 1970.

[13] J.W. Deardorff. The use of subgrid transport equations in a three dimensional model of atmospheric turbulence. *J. Fluids Eng.*, 95:429–438, 1973.

[14] C.H. Moeng. A large-eddy-simulation model for the study of planetary boundary layer turbulencea large-eddy-simulation model for the study of planetary boundary layer turbulence. *J. Atmos. Sci.*, 41:2052–2062, 1984.

[15] D.K. Lilly. The representation of small-scale turbulence in numerical simulation experiments. *Proceedings of the IBM Scientific Computing Symposium on Environmental Sciences*, IBM form no. 320-1951:195–210, 1967.

[16] J.W. Deardorff. Stratocumulus-capped mixed layers derived from a three-dimensional model. *Bound.-Layer Meteor.*, 18:495–527, 1980.

[17] Branko Kosovic. Subgrid-scale modelling for the large-eddy simulation of high reynolds number boundary layers. *J. of Fluid Mech.*, 336:151–182, 1997.

[18] Jianming He and C.S Song. Evaluation of pedestrian winds in urban area by numerical approach. *Journ. of Wind Eng. and Indust. Aerodynamics*, 81:295–309, 1999.

[19] Sinisa Kranjnovic. Large eddy simulation of flows around ground vehicles and other bluff bodies. *Phil. Trans. R. Soc. A*, 367:2917–2930, 2011.

[20] Christopher Knigge and Siegfried Raasch. Characterization of wind gusts using a large eddy simulation model. *Third Symposium Simulation of Wing and Nacelle Stall*, 2012.

[21] Joseph Priestly. *Correlation Studies of Pressure Fluctuations on the Ground Beneath a Turbulent Boundary Layer.* M.S. Thesis, Institute for Fluid Dynamics and Applied Mathematics, University of Marlyland, 1965.

[22] F.D. Shields. Low-frequency wind noise correlation in microphone arrays. *Acoustical Society of America*, 11:3489, 2005.

[23] Jiao Yu. *Calculation of Wind Noise Measured at the Surface Under Turbulent Wind Fields.* Ph.D. Dissertation, Dept. of Physics and Astronomy, The University of Mississippi, 2009.

[24] Hao Lu and Fernando Porte-Agel. Large-eddy simulation of a very large wind farm in stable atmospheric boundary layer. *Physics of Fluids*, 23, 2011.

[25] AMS: Meteorological glossary. `http://glossary.ametsoc.org/`.

[26] Tony Burton, Nick Jenkins, David Sharpe, and Ervin Bossanyi. *Wind Energy Handbook.* John Wiley and Sons, second edition, 2011.

[27] H.H. Monahan and M. Armedariz. Gust factor variations with height and atmopsheric stability. *Journal of Geophysical Research*, 76:5807–5818, 1971.

[28] John Wyngaard. *Turbulence in the Atmosphere.* Cambridge University Press, first edition, 2010.

[29] Martin J. Otte and John C. Wyngaard. Stably stratified interfacial-layer turbulence from large-eddy simulation. *Journal of the Atmospheric Sciences*, 58:3424–3442, 2001.

[30] James Dunyak, Xianoning Filliam, Richard Peterson, and Douglas Smith. Coherent gust detection by wavelet transform. *Wind Engineering and Industrial Aerodynamics*, pages 467–478, 1998.

[31] M. Farge. Wavelet transforms and their applications to turbulence. *Annual Review of Fluid Mechanics*, 24:395–457, 1992.

[32] Christopher Torrence and Gilbert P. Compo. A practical guid to wavelet analysis. *Bulletin of the American Meteorlogical Society*, 79(1):61–78, 1998.

[33] J.C.W. Denholm-Price and J.M. Rees. Detecting waves using an array of sensors. *American Meteorological Society*, 127:57–69, 1999.

Appendices

APPENDIX 1: GROUND-BASED ELEVATED GUST TRACKER MATLAB CODE

```
%%%%%%%%%%%%%%%%%%%%%%%%%%%%%%%%%%%%%%%%%%%%%%%%%%%%%%%%%%%%
%%%%%%%%% GROUND—BASED ELEVATED GUST TRACKER (GEGT) %%%%%%%%
%%%%%%%%%%%%%%%%%%%%%%%%%%%%%%%%%%%%%%%%%%%%%%%%%%%%%%%%%%%%

function tracker(tStart,tEnd,threshold,p_input,u_input,v_input)

%%%%%%%%%%%%%%%%%%%%%%%%%%%%%%%%%%%%%%%%%%%%%%%%%%%%%%%%%%%%
%%% GEGT identifies peaks in the pressure at each time %%%%%
%%% step, determines if they move along a coherent path,%%%%
%%% filters pressure peaks below a chosen threshold,   %%%%%
%%% calculates the x and y components of the pressure  %%%%%
%%% transfer velocity (PTV), and checks them against the %%%
%%% instantaneous velocities on the ground and reports %%%%%
%%% the time and array location of gust activity.      %%%%%
%%%%%%%%%%%%%%%%%%%%%%%%%%%%%%%%%%%%%%%%%%%%%%%%%%%%%%%%%%%%
%%%%%%%%%%%%%%%%%%%%%%%%%%%%%%%%%%%%%%%%%%%%%%%%%%%%%%%%%%%%
%%% inputs:  p_input, pressures time series measured by %%%%
%%%          the 2D array.                              %%%%
%%%          u_input, x—velocity time series measured by %%%
%%%          the 2D array.                             %%%%%
%%%          v_input, x—velocity time series measured by %%%
%%%          the 2D array.                             %%%%%
%%%%%%%%%%%%%%%%%%%%%%%%%%%%%%%%%%%%%%%%%%%%%%%%%%%%%%%%%%%%
%%% Example:  tracker(1,200,5,p,u,v)                  %%%%%%
%%%%%%%%%%%%%%%%%%%%%%%%%%%%%%%%%%%%%%%%%%%%%%%%%%%%%%%%%%%%
```

```

%  Opens a file to record gusts locations
%  and initializes arrays.

fileID = fopen('gustlog.txt','w');
ROW = zeros(tEnd);
COL = zeros(tEnd);
U_p = zeros(tEnd);
V_p = zeros(tEnd);

for i = tStart:tEnd;                 % simulates incoming data
p_mat = squeeze(p_input(:,:,i));     % squeezes to x-y foot print
u_mat = squeeze(u_input(:,:,i));
v_mat = squeeze(v_input(:,:,i));
max_value = max(max(p_mat));         % finds peak in the pressure
[row,col]=find(p_mat == max_value); % finds x-y coordinates of peak
ROW(i) = row;                        % stores x coordinates in array
COL(i) = col;                        % stores y coordinates in array
%if (row == 4) && (col == 4);        % simulates missing data at center,
    %continue                         % comment out if not using.
%elseif i > 1;                        % excludes first point.
if i > 1

% is the pressure magnitude greater than threshold?

  if(p_input(ROW(i),COL(i),i) > threshold)

% calculates pressure transfer rate (PTR) components.

  U_p(i) = 2*(row-ROW(i-1))./(i-(i-1));
  V_p(i) = 2*(col-COL(i-1))./(i-(i-1));

```

```
  % NE Monitor:  This monitors the NW direction.

% checks to see if pressure peak moved downstream in 1 second

  if(row > ROW(i−1) && col ≥ COL(i−1));

% checks to see if PTR exceeds the instantaneous velocity on the ground
% in the x or y direction.

  if(U_p(i) > u_mat(ROW(i),COL(i)) || V_p(i) > v_mat(ROW(i), COL(i)));

% does the event still exist 2 s later?

  if(row > ROW(i−2) && col ≥ COL(i−2));

% 3 s later? (comment out for 2 second sensitivity).

  if(row > ROW(i−3) && col ≥ COL(i−3));

%  Print to command line and save in a file gust detection coordinates
%  and direction estimate.

  fprintf(fileID,'Gust Highly Likely at t = %s s, x = %s, ...
  y=%s, NE; t = %s s, x = %s, y = %s\n',num2str(i),num2str(ROW(i)), ...
  num2str(COL(i)),num2str(i−3),num2str(ROW(i−3)),num2str(COL(i−3)));

  fprintf('Gust Highly Likely at t = %s s, x = %s, y=%s, ...
  NE; t = %s s, x = %s, y = %s\n',num2str(i),num2str(ROW(i)), ...
  num2str(COL(i)),num2str(i−3),num2str(ROW(i−3)),num2str(COL(i−3)));

%  Plots monitor on a subplot.

```

```
      figure(1);
      subplot(2,2,2);
      scatter(row,col);
      text(row,col,num2str(i),'FontSize',9);
      title(sprintf('N—E Monitor: Gust Location'));
      xlabel('x');
      ylabel('y');
      axis([1 length(p_input(:,:,1)) 1 length(p_input(:,:,1))]);
      pause(.5);
      hold on;
      end
      end % Comment out for 2 second sensitivity.
      end

  % NW Monitor

  elseif(row < ROW(i−1) && col ≥ COL(i−1));
  if(U_p(i) < u_mat(ROW(i),COL(i)) || V_p(i) > v_mat(ROW(i), COL(i)));
  if(row < ROW(i−2) && col ≥ COL(i−2));
  if(row < ROW(i−3) && col ≥ COL(i−3)); % Comment out for 2 second ...
     sensitivity.

%  Print to command line and save in a file gust detection coordinates
%  and direction estimate.

  fprintf(fileID,'Gust Highly Likely at t = %s s, x = %s, ...
  y=%s, NW; t = %s s, x = %s, y = %s\n',num2str(i),num2str(ROW(i)), ...
  num2str(COL(i)),num2str(i−3),num2str(ROW(i−3)),num2str(COL(i−3)));

  fprintf('Gust Highly Likely at t = %s s, x = %s, y=%s, ...
  NW; t = %s s, x = %s, y = %s\n',num2str(i),num2str(ROW(i)), ...
  num2str(COL(i)),num2str(i−3),num2str(ROW(i−3)),num2str(COL(i−3)));
```

```
      subplot(2,2,1);
      scatter(row,col);
      text(row,col,num2str(i),'FontSize',9)
      title(sprintf('N-W Monitor: Gust Location'));
      xlabel('x');
      ylabel('y');

      axis([1 length(p_input(:,:,1)) 1 length(p_input(:,:,1))]);
      pause(.5);
      hold on;
      end
      end %Comment out for 2 second Sensitivity.
      end

  % SE Monitor

  elseif(row > ROW(i-1) && col ≤ COL(i-1));
  if(U_p(i) > u_mat(ROW(i),COL(i)) || V_p(i) < v_mat(ROW(i), COL(i)));
  if(row > ROW(i-2) && col ≤ COL(i-2));
  if(row > ROW(i-3) && col ≤ COL(i-3));  % Comment out for 2 second ...
     sensitivity.

%  Print to command line and save in a file gust detection coordinates
%  and direction estimate.

  fprintf(fileID,'Gust Highly Likely at t = %s s, x = %s, ...
  y=%s, SE; t = %s s, x = %s, y = %s\n',num2str(i),num2str(ROW(i)), ...
  num2str(COL(i)),num2str(i-3),num2str(ROW(i-3)),num2str(COL(i-3)));

  fprintf('Gust Highly Likely at t = %s s, x = %s, y=%s, ...
  SE; t = %s s, x = %s, y = %s\n',num2str(i),num2str(ROW(i)), ...
```

```
 num2str(COL(i)),num2str(i-3),num2str(ROW(i-3)),num2str(COL(i-3)));



   subplot(2,2,4)
   scatter(row,col);
   text(row,col,num2str(i),'FontSize',9);
   title(sprintf('S-E Monitor: Gust Location'));
   xlabel('x');
   ylabel('y');
   axis([1 length(p_input(:,:,1)) 1 length(p_input(:,:,1))]);
   pause(.5);
   hold on;
   end
   end  % Comment out for 2 second sensitivity.
   end

 % SW Monitor

 else(row < ROW(i-1) && col ≤ COL(i-1));
 if(U_p(i) < u_mat(ROW(i),COL(i)) || V_p(i) < v_mat(ROW(i), COL(i)));
 if(row < ROW(i-2) && col ≤ COL(i-2));
 if(row < ROW(i-3) && col ≤ COL(i-3)); % Comment out for 2 second ...
   sensitivity.

%  Print to command line and save in a file gust detection coordinates
%  and direction estimate.

 fprintf(fileID,'Gust Highly Likely at t = %s s, x = %s, ...
 y=%s, NE; t = %s s, x = %s, y = %s\n',num2str(i),num2str(ROW(i)), ...
 num2str(COL(i)),num2str(i-3),num2str(ROW(i-3)),num2str(COL(i-3)));

 fprintf('Gust Highly Likely at t = %s s, x = %s, y=%s, ...
```

```
  NE; t = %s s, x = %s, y = %s\n',num2str(i),num2str(ROW(i)), ...
  num2str(COL(i)),num2str(i-3),num2str(ROW(i-3)),num2str(COL(i-3)));


      subplot(2,2,3)
      scatter(row,col);
      text(row,col,num2str(i),'FontSize',9);
      title(sprintf('S-W Monitor: Gust Location'));
      xlabel('x');
      ylabel('y');
      axis([1 length(p_input(:,:,1)) 1 length(p_input(:,:,1))]);
      pause(.5);
      hold on;
      end
      end  % Comment out for 2 second sensitivity.
      end
      end
  end
end
end
end
```

VITA

Jericho Cain was born in Oklahoma City, OK on December 13, 1979. He attended Brookwood High School in Atlanta, GA and graduated in 1998. Between 2003 and 2006 he studied physics at Georgia State University in Atlanta, GA. He received an M.A. in physics from the University of Mississippi in 2010.